

Title	振動型移動機構を用いた地形ナビゲーションのための適応型ソフトロボット
Author(s)	NGUYEN VIET LINH
Citation	
Issue Date	2025-03
Type	Thesis or Dissertation
Text version	ETD
URL	<a href="http://hdl.handle.net/10119/19932">http://hdl.handle.net/10119/19932</a>
Rights	
Description	Supervisor: HO, Anh Van, 先端科学技術研究科, 博士

Doctoral Dissertation

ADAPTIVE SOFT ROBOTS FOR TERRAIN NAVIGATION USING VIBRATORY  
LOCOMOTION

**Nguyen Viet Linh**

Supervisor **Ho Anh Van**

Graduate School of Advanced Science and Technology  
Japan Advanced Institute of Science and Technology  
Materials Science

March 2025





# Abstract

Robots with adaptive morphology can enhance body-environment interactions to enable adaptive functions without requiring complex control strategies, whereas traditional robots with fixed structures often rely on intensive computations, especially when encountering sudden environmental changes. In contrast, a robot with adaptive morphology can adjust to environmental changes with minimal effort. However, in-depth research has been limited to extending adaptive capabilities to small-scale robots to navigate constrained and variable environments where existing designs still struggle with certain tasks. To address these challenges, this study introduces two morphological designs: the first, named **Leafbot**, is designed for adapting to and traversing obstacles and uneven terrains in planar environments. The second is named **PufferFace Robot (PFR)**, inspired by the inflation and deflation mechanism of a pufferfish. PFR design features stretchable skin, allowing it to adapt to variable hollow-constrained structures, such as pipeline systems. Both target small-scale applications. Thus, vibration-driven sources are employed because of their compactness and robustness. The underlying physical phenomena are analyzed to construct an analytical model on Leafbot and a Finite Element Analysis (FEA)-based simulation model on PFR. The vibration-based locomotion and terradynamic properties of both designs were investigated to assess their performance under specific conditions. The results of the terradynamic studies of two designs highlight the significance of adaptive morphology with Leafbot overcoming obstacles up to five times its hip height and navigating rugose terrains ( $R_g = 0.28$ ), while PFR adapts to cavities with inner diameters ranging from 1 to 1.5 times its own diameter, which is significant compared to other robots with similar functions. This study expands the locomotion possibilities for vibration-driven robots beyond flat, even surfaces to diverse and challenging terrains in planar scenarios. For hollow-constrained environments such as pipeline networks, this research contributes a morphological design with high adaptability and the capability of implementing inspection tasks in dark conditions.

**Keywords:** Adaptive morphology soft robots, vibration-based locomotion, terradynamics, legged locomotion, pipeline inspection robot.



## Acknowledgment and Dedication

First and foremost, I would like to express my heartfelt gratitude to my supervisor, *Professor Ho Anh Van*, for his invaluable mentorship, patience, and encouragement that has guided me through three and a half years of challenges and desperation when dealing with difficulties of pursuing a Ph.D. degree. Countless and immense support from Prof. Van, as well as his insights and expertise, have been instrumental in shaping the direction and success of this work. Furthermore, the hardships I encountered during my Ph.D. duration extended beyond scientific challenges, encompassing personal problems that felt unsolvable at first glance. Even though I did not explicitly share these struggles, my supervisor recognized them and offered unwavering support and invaluable opportunities, which helped me navigate the most challenging phases of my Ph.D. journey. Therefore, all triumphs of this research are dedicated to my respectful supervisor, *Professor Ho Anh Van*.

I am deeply grateful to my second supervisor, *Professor Kazuaki Matsumura*, for his valuable insights on my research proposal and his support for this research topic. I also extend my sincere gratitude to *Professor Nguyen Le Minh* and *Professor Alambeigi Farshid* for their insightful advice, support, and guidance on my minor research project.

My appreciation also extends to my lab mates, especially *Assistant Professor Nguyen Huu Nhan*, *Dr. Nguyen Dang Duy*, *Dr. Luu Khanh Quan*, *Dr. Le Dinh Minh Nhat*, and *Mr. Nguyen Thanh Khoi*. Their invaluable support of expertise significantly contributes to the success of this work. To a further extent, this could have been a boring, stressful, and desperate journey without the company of all lab members.

I am heartfelt grateful to my father, *MD. Nguyen Van Hai*, my mother, *Mrs. Tran Thi Lan*, and my younger brother, *Mr. Nguyen Tung Lam*, whose unwavering support has been the foundation of my journey. Their encouragement and understanding have carried me through countless challenges, and their belief in me has been a constant source of strength and motivation. I owe much of my success to their love and sacrifices, which have inspired me to persevere and strive for excellence. Furthermore, I would like to extend my heartfelt gratitude to my father- and my mother-in-law, *Mr. Nguyen Thanh Hung* and *Mrs. Nguyen Thi Thu* for their love, support, and encouragement throughout this challenging journey.

Finally, I dedicate this work to my beloved wife, *Mrs. Nguyen Thi Thanh Tuyen*, whose patience, support, and love have been my greatest source of inspiration. Her understanding and encouragement through the ups and downs of this journey have been invaluable. I am deeply thankful for her presence by my side and her constant endurance for having been apart for almost eight years, making this achievement all the more meaningful.

# Contents

<b>Abstract</b>	<b>I</b>
<b>Acknowledgment and Dedication</b>	<b>III</b>
<b>Contents</b>	<b>V</b>
<b>List of Figures</b>	<b>IX</b>
<b>List of Tables</b>	<b>XIX</b>
<b>Chapter 1 Introduction</b>	<b>1</b>
1.1 Background . . . . .	1
1.1.1 Adaptive morphological designs of soft robots . . . . .	1
1.1.2 Locomotion of soft robots. . . . .	3
1.2 Motivations and research questions . . . . .	4
1.3 Originality and contributions . . . . .	5
1.4 Significance . . . . .	6
1.5 Proposing two morphological design concepts with vibration-based locomotion .	6
1.6 Dissertation structure . . . . .	8
<b>Chapter 2 Related Works</b>	<b>9</b>
2.1 Vibration-driven designs for planar working conditions . . . . .	9
2.2 Vibration-driven and other developed mechanisms for cavity working conditions	11
2.3 Terradynamics study of vibration-driven robots. . . . .	12
2.4 Vibration-based locomotion: one mechanism adaptable to both planar and cavity conditions. . . . .	15
<b>Chapter 3 Two Developed Morphological Designs of Soft Robot Driven by Vibration Mechanism</b>	<b>17</b>

3.1	Vibration-driven locomotion mechanism . . . . .	17
3.2	Two morphological designs of soft robot driven by vibration mechanism . . . . .	19
3.2.1	Vibration-based robot design for planar working conditions - <i>Leafbot</i> . . . . .	20
3.2.2	Vibration-based robot design for constrained cavity conditions - <i>Puffer-Face Robot (PFR)</i> . . . . .	25

## Chapter 4 Study and Analyze the Involving Physics Phenomena of Vibration-based Soft Robot Designs 33

4.1	The involving physics phenomena on <i>Leafbot</i> . . . . .	33
4.1.1	Vibration frequency . . . . .	33
4.1.2	Transverse waves along the soft backbone . . . . .	35
4.2	The involving physics phenomena on <i>PFR</i> . . . . .	36
4.2.1	Modes of locomotion . . . . .	37
4.2.2	Vibration frequency . . . . .	41
4.2.3	Characterization of the inflation radius . . . . .	44
4.2.4	Propulsion force examination . . . . .	45

## Chapter 5 Showcase of Vibration-driven Design in Planar Conditions: *Leafbot* 49

5.1	Constructing analytical model of <i>Leafbot</i> . . . . .	49
5.2	Experimental scheme for <i>Leafbot</i> 's locomotion evaluation . . . . .	55
5.2.1	Experimental design for locomotion verification . . . . .	55
5.2.2	Outcomes obtained from the experimental and analytical methods . . . . .	56
5.3	<i>Terradynamics</i> study of <i>Leafbot</i> . . . . .	63
5.3.1	Scenario 1: Slope locomotion . . . . .	65
5.3.2	Scenario 2: Semi-circular obstacles traversability . . . . .	67
5.3.3	Scenario 3: Rugose terrain traversability . . . . .	69
5.4	In-plane locomotion verification of <i>Leafbot</i> . . . . .	71
5.4.1	Modified design . . . . .	71
5.4.2	Experimental setup . . . . .	71
5.4.3	Outcomes . . . . .	72

## Chapter 6 Showcase of Vibration-driven Design in Constrained Cavity Conditions: *PufferFace Robot - PFR* 77

6.1	Experimental scheme for PFR locomotion verification in the horizontal condition	77
-----	---	----

6.2	Constructing the Finite Element Analysis (FEA) simulation model of PFR . . .	78
6.3	Experiment and FEA simulation outcomes in horizontal pipes . . . . .	81
6.3.1	Experimental results . . . . .	81
6.3.2	FEA simulation results in ABAQUS . . . . .	84
6.4	Investigate the influence of $Df_r^a$ and $P_{M3}^S$ to locomotion performance in horizontal and vertical conditions . . . . .	84
6.5	Estimate the maximum traveling distance in certain circumstances . . . . .	87
6.6	Terradynamics study of PFR through critical and hybrid conditions of a pipeline system by empirical and experimental approaches . . . . .	89
<b>Chapter 7</b>	<b>Discussion and Conclusion</b>	<b>93</b>
7.1	Leafbot design . . . . .	93
7.1.1	Design and fabrication . . . . .	93
7.1.2	Dynamics and <i>Terradynamics study</i> . . . . .	93
7.1.3	In-plane locomotion verification . . . . .	94
7.1.4	Conclusion . . . . .	94
7.1.5	Future works . . . . .	95
7.2	PufferFace Robot-PFR design . . . . .	95
7.2.1	Design and fabrication . . . . .	95
7.2.2	Locomotion performance . . . . .	96
7.2.3	FEA-based simulation model . . . . .	97
7.2.4	Evaluate the cavity traversal performance based on the <i>terradyamics</i> approach . . . . .	98
7.2.5	Conclusion . . . . .	98
7.2.6	Future work . . . . .	99
	<b>Achievements</b>	<b>101</b>
	<b>Appendices</b>	<b>103</b>
	<b>Appendix A Limb morphology of Leafbot</b>	<b>103</b>
	<b>Appendix B Experimental values of Leafbot</b>	<b>105</b>
	<b>References</b>	<b>107</b>





# List of Figures

1.1	Morphological bodies facilitate the interaction with the environments to reduce the computational burdens (the picture adopted from [1]). (A) the sprawl robot leverages the material properties of its legs to achieve rapid locomotion. The elasticity in its linear joint, derived from the compressed air, allows the robot to automatically adapt its movement over uneven terrain, minimizing the need for complex computation. (B) The leg morphology of the animal, derived from the elasticity of its muscle, features an adaptive function, resulting in reducing the computation. (C) A robot constructed from rigid materials requires a complex control algorithm to adapt to uneven terrain, leading to significantly slowing down its movement. . . . .	2
1.2	The remarkable adaptability and flexibility of soft robots advance the terrain's traversal with irregularities and complicated constraints that conventional rigid robots find challenging to be qualified for these tasks. (A) The soft robot with a moving mechanism is inspired by the growth of plants. It is well suited for variable-confined-hollow structures. (B) the multilegged miniature soft robot adapts to harsh environments where surface features are complicated. This soft adaptive design shows the potential for biomedical applications (the images adopted from [2,3]). . . . .	3
1.3	The proposed adaptive design concept for planar and variable-constrained cavity working conditions. The robot's hollow structure enables fluid and gas flow when operating in such conditions. . . . .	7

- 2.1 The developed vibration-based designs. (A) A miniature robot is driven by a piezoelectric stack. (B) One of the common designs of bristlebot is driven by an eccentric motor. (C) A rigid backbone is incorporated with inclined bristles and two vibration motors to generate forward motion. (D) A design takes advantage of the influence of the vibration phenomenon to create a vacuum state, causing the robot firmly suck to flat surfaces. However, the motion is manipulated by two DC motors. (E) A soft body with an asymmetric limb structure is integrated with a vibration source to induce forward motion (the images adopted from [4–8]). 10
- 2.2 Several developed designs aim for various tubular environments. (A) A pipeline inspection robot for small-scale applications is driven by DEAs. (B) A vibration-based robot with an inclined bristles pattern was developed for inspection tasks. (C) A miniature robot incorporated kirigami soft wheels is driven by a wheel-based mechanism. (D) A vibration-based soft robot, including two sub-modules, facilitates complex navigation tasks in pipelines. (E) A rigid wheel-driven design robot adapts to various sizes of cylindrical channels (the images adopted from [9–13]). . . . . 12
- 2.3 The *terradynamics* studies investigated how body morphology affects the traversability of robots with certain terrains. (A) B. Chong *et al.*, evaluated the relation between the redundancy of the number of robot’s limbs with the traversal to step-field terrains. (B) The *terradynamics* term was initially proposed by C. Li *et al.*, to assess the locomotion of their legged robot design with the granular media. (C), (D) S.W. Gart *et al.*, published studies that verified the traversability of their legged robots with large gaps and bumps (the images adopted from [14–17]). 13
- 2.4 (A) The most common design in the vibration-based robot class is a bristlebot design. (B) Drawing inspiration from the bristlebot, we developed a vibration-driven robot with a flexible soft body to enhance its ability to navigate rough terrains. The design incorporates inclined elastic limbs, serving a similar purpose to the elastic bristles in brushbot designs, which is compulsory for generating forward motion. . . . . 14

2.5	(A) A rigid design of the pipe inspection robot, equipped with an active size-adjustment mechanism, allows it to adapt to various pipe sizes (the image adopted from [18]). (B) A vibration-driven soft robot concept featuring a flexible soft skin allows it to adapt to different pipe sizes, with expansion achieved through an external compressed air supply. This concept aims for small-scale pipeline applications. . . . .	15
3.1	The vibration-based locomotion mechanism on a bristlebot. The bristlebot is represented by a rigid body with inclined elastic bristles. The non-symmetric friction feature is attributed to the inclination of the bristles. Under the excitation of the vibration source, a forward motion can be achieved thanks to the asymmetric friction mechanism. . . . .	18
3.2	The stick-slip mechanism caused by anisotropic friction forces results in net displacements, $N_{D1}$ and $N_{D2}$ , over one cycle of centripetal force [5]. . . . .	19
3.3	The general design of the robot: (a) The robot design components. (b) The design parameters. . . . .	20
3.4	The morphology of the limb design: (a) The incline-beam shape. (b) The desired shape of limb design. (c) The simplified models of limb shapes are in contact with slopes. . . . .	21
3.5	The experiment scheme to evaluate the propelled force when the limb is compressed. (A) Utilizing a 3-axis force sensor to collect yielded force data. (B) The acquired force graph. . . . .	21
3.6	The ABAQUS simulation is conducted on two designs of limb, an inclined straight and a curved limb, to evaluate the contact features in terms of the number and area of contact with the sloped obstacles. (A) The curved limb interacts with the slope. (B) The results of the curvy limb. (C) The inclined straight limb interacts with the slope. (D) The results of the inclined straight limb. The red background implies the failure, while the green background implies the robot's success. . . . .	22
3.7	The obtained average velocity of three radius designs of the limb. . . . .	24
3.8	Three limb patterns were fabricated to study the terradynamics. <b>(A)</b> Leafbot3 pattern; <b>(B)</b> Leafbot5 pattern; <b>(C)</b> Leafbot9 pattern. . . . .	24
3.9	The fabrication process of the monolithic soft body. . . . .	25

3.10	(A) Examples of cavity conditions in industrial applications. (B) The concept of a vibration-propelled robot with an inflatable structure that is capable of adapting to various cavities' working conditions. (C) The model design drew inspiration from a pufferfish. (D) PFR is in the inflation state. (E) PFR is in the normal state. PFR is equipped with an LED and a tiny NanEye camera to serve inspection tasks in dark conditions. . . . .	27
3.11	The 3D design model of PFR: (A) the component's view of PFR. (B) The front view and side view of PFR are shown with the dimensions, including the frame inner diameter $ID_F = 12$ mm, the frame outer diameter $OD_F = 15$ mm, the 1mm-thickness soft skin outer diameter $OD_S = 27$ mm, the length of the PFR body $L_B = 30$ mm, and the overall length of the PFR $L_O = 33$ mm, when it is in the normal state. . . . .	28
3.12	The dimensions of PFR's parts. (A) the front view of PFR; $OD_S = 27$ mm, $ID_{SB} = OD_F = 15$ mm, $OD_{SB} = 17$ mm; (B) the side view of PFR; $L_B = 30$ mm. (C) The cross-section of the 3D printing mold presents the dimensions of the soft spike. . . . .	30
3.13	The fabrication process of PFR. . . . .	32
4.1	Marker-based model for robot motion investigation. Markers' coordinates are then determined with respect to time. A time step (dt) is equal to 1/960 (designed frame per second - fps of HSC). (a) Green markers on the robot backbone; (b) The experimental set-up; (c) Example of the first marker's trajectory. . . . .	34
4.2	Employing piezoelectric disc to determine the vibration frequencies corresponding to the applied voltage on driven motors. The vibrator mounting to a 3D-printing housing is attached to the piezoelectric disc by a double-sided tape [19]. . . . .	36
4.3	The obtained trajectory of the first marker of Leafbot5 by processing the captured image from HSC. (A) The displacement of the 1st marker in the Z direction, $\hat{z}_1$ , at 3V. (B) The collected dominant freq. in freq. domain by FFT from experimental data of vector $\hat{z}_1$ at 3V. . . . .	36
4.4	Clarifying the frequency decline phenomenon of the vibrator when it was incorporated into different objects. . . . .	37
4.5	The determination of the time difference between two nearby peaks (marker 2 and marker 3) of a transverse wave, $\tau$ , in the case of Leaf5 at 3V (132Hz). . . . .	38

4.6	Operation principle and locomotion modes of PFR. (A) the PFR is in the tubular condition whose inner diameter exceeds the PFR's outer diameter. The PFR is in a normal state. A vector of centripetal force, $F_C$ , is generated by the DC vibrator and relies on its rotation angle, $\varphi$ . (B) The PFR is transformed from the normal state into the inflation state via the supplying air channel and adapts to a bigger-diameter condition of the cavity environment. (C) Modes of locomotion explanation. Mode 3 is a combination of the vibration and inflation/deflation process. In the subset figure of Mode 3, the dash-dot line and the solid line, which are out of phase by $\pi/2$ , stand for the centripetal force vector components in the plane containing $\hat{Y}_{fr}$ axis and $\hat{Z}_{fr}$ axis. . . . .	39
4.7	The experiment to determine the relation between the applied voltage (V) and the vibration frequency (Hz) and its obtained results. . . . .	42
4.8	The obtained average velocity of PFR with respect to vibration frequency in Mode 1 of locomotion. . . . .	43
4.9	The relation between the applied pressures and the obtained expansion radii of soft skin. (A) Employing a hyperelastic simulation module of ABAQUS to identify the radius behavior corresponding to the applied pressure. The simulation can be utilized to determine arbitrary radii corresponding to desired tubular working conditions. (B) Identifying the expansion radius by capturing the inflation state. (C) The outcomes of the empirical and simulated methods were obtained. . . . .	44
4.10	The experimental scheme to measure the propulsion force generated from the soft spike pattern. . . . .	45
4.11	Obtained propulsion forces conducted in the $ID_P^1=30$ mm, $ID_P^2=36$ mm, and $ID_P^3=41$ mm pipes in the aforementioned pre-setting conditions. (A, D, G), (B, E, H), and (C, F, I) demonstrate the results in the cases of applying pressures 20 kPa, 23 kPa, and 26 kPa, respectively. . . . .	47

4.12	The shapes of the soft skin when subjected to three pressure air values in three tube dimensions. (A, B, C), (D, E, F), and (G, H, I) are cases in which PFR is tested in 30-mm, 36-mm, and 41-mm tubes, respectively. The inset figure in (C) illustrates the traces of the contacting soft limbs with the wall. The white infill squares stand for the contacting spikes, whereas the sole-solid-line squares represent the non-contacting spikes. Each row of soft spikes in the radial direction is numbered from one to five from right to left. Each white square stands for 14 radially distributed soft spikes. . . . .	48
5.1	The proposed dynamics scheme for the robot design. (a) The simplified model of the vibrator. All limbs in the red dashed line region are merged into a single node, attaching to an equivalent spring and damper. (b) The soft and monolithic structure of the robot body is transformed into the line-segment model and characterized by the viscoelastic model. These models characterize Leafbot's analytical model. (c) The transverse forces are induced by the transverse wave generated by the vibration source. . . . .	50
5.2	(A), (B), (C) The trajectory of the 1st marker in the $Z$ direction determined by experimental method and analytical model under the three pre-determined excitation freqs.: 132 Hz, 142 Hz, and 186 Hz, respectively. . . . .	56
5.3	(A), (B), (C) The collected dominant freq. in freq. domain by FFT from experimental data of vector $\hat{z}_1$ at pre-determined excitation freq. 132Hz, 142Hz, and 186Hz, correspondingly. . . . .	57
5.4	(A), (B), (C) The trajectories of the 2nd to the 4th node in the $Z$ direction are determined by experimental method and analytical model under the three pre-determined excitation freqs.: 132 Hz, 142 Hz, and 186 Hz, respectively. For ease of observation, $z_2$ and $z_3$ lines are offset 4 mm, apart. $z_3$ and $z_4$ lines are 6 mm. . . . .	58
5.5	The position of the marker on Leafbot5 tracked by the OptiTrack system over time is presented between analytical and experimental data. The area enclosed by the red-dash line is presented in Figure 5.7. . . . .	59
5.6	Attained velocity, $\dot{x}_1$ , from the analytical model, and average velocity from the experimental results of the marker, tracked by OptiTrack system along the $X$ direction. . . . .	60

5.7	The $x_1$ , $\dot{x}_1$ , $z_1$ , and $\dot{z}_1$ results of Leafbot5 from the analytical model are illustrated in a very short time domain. . . . .	61
5.8	The position of the marker on Leafbot3 tracked by the OptiTrack system over time is presented between analytical and experimental data. . . . .	62
5.9	The position of the marker on Leafbot9 tracked by the OptiTrack system over time is presented between analytical and experimental data. . . . .	62
5.10	Obtained ave. velocity at three limb pattern variants on the ascending slope angle. <b>(A)</b> Leafbot3; <b>(B)</b> Leafbot5; <b>(C)</b> Leafbot9. . . . .	63
5.11	The traversability experiment scheme. Scenario 1: The robot traversed through slope obstacles characterized by slope $\beta$ and height $h$ . Scenario 2: The robot traversed through semi-circular-like obstacles characterized by $R$ . Scenario 3: The robot traversed through a designed terrain characterized by the rugosity $R_g$ factor. . . . .	64
5.12	The traversal success rate, $S_r$ , of Leafbot's patterns in Scenario 1. <b>(A)</b> Leafbot3; <b>(B)</b> Leafbot5; <b>(C)</b> Leafbot9. . . . .	66
5.13	The traversal success rate, $S_r$ , of Leafbot's patterns in Scenario 2: <b>(A)</b> Leafbot3, <b>(B)</b> Leafbot5, and <b>(C)</b> Leafbot9. . . . .	68
5.14	The step-field terrain was constructed based on the rugosity. <b>(A)</b> $R_g = 0.18$ , <b>(B)</b> $R_g = 0.28$ . . . . .	69
5.15	The empirical traverse duration of patterns in two rugose terrains, $R_g = 0.18$ and $R_g = 0.28$ . <b>(A)</b> the traverse duration of Leafbot5. <b>(B)</b> the traverse duration of Leafbot9. The duration of Leafbot3 does not appear in this figure since Leafbot3 fails to overcome both designed terrains, which means the duration becomes infinite. . . . .	70
5.16	The vibrator configurations. <b>(A)</b> Two side vibrators are placed at the rear of the body; <b>(B)</b> Two vibrators are placed in the middle of the body; <b>(C)</b> Two side vibrators are installed at the front. Two vibrators are placed $D_v = 30\text{ mm}$ apart. . . . .	71
5.17	The experiment setup to explore the trajectories of Leafbot-X5 in 2D space. The center trajectory, the white line, is determined from the trajectories at both sides of Leafbot. . . . .	72



5.18	The navigation performance of Leafbot-X5's configurations when equipped with two side vibrators at different vibration frequencies. The duration of the applying vibration to the driven vibrator was two seconds in every experiment. . . . .	74
5.19	The performance of Leafbot-X5 in delivering the straight-line locomotion by simultaneously activating two side vibrators at 3V in three seconds (the correspondingly induced frequency is 95Hz). (A), (B), (C) The trace of Front, Middle, and Rear configuration, respectively. . . . .	75
6.1	The experimental scheme to measure the displacement of PFR over time in the horizontal condition. . . . .	78
6.2	FEM simulation procedure with ABAQUS. (A) The removal of unnecessary parts for the simulation. (B) The simplified model of the cavity and the soft skin of PFR. How physical factors, including sinusoidal centripetal force $F_C$ and pressurized air, come into play in the model. (C) The characterization of the inflation and deflation phases. . . . .	79
6.3	Prepared samples to measure the stiffness behaviors of three patterns of soft spikes. (A) A $7 \times 5$ pattern sample ( $i_1$ to $i_7$ ; $j_1$ to $j_5$ ). (B) $5 \times 5$ pattern sample ( $i_1$ to $i_5$ ; $j_1$ to $j_5$ ). (C) $3 \times 5$ pattern sample ( $i_1$ to $i_3$ ; $j_1$ to $j_5$ ). . . . .	81
6.4	The stiffness behaviors of three patterns, <i>i.e.</i> , $3 \times 5$ , $5 \times 5$ , and $7 \times 5$ soft spike patterns. . . . .	82
6.5	The PFR's position data in X direction was collected when testing in $ID_P^1 = 30$ mm, $ID_P^2 = 36$ mm and $ID_P^3 = 41$ mm pipes in the aforementioned pre-setting conditions. <b>(A, D, G)</b> , <b>(B, E, H)</b> , <b>(C, F, I)</b> illustrate the results in the cases of applying pressures 20 kPa, 23 kPa, and 26 kPa, respectively. . . . .	83
6.6	The displacement behaviors vary according to different average deflation rates, $Df_r^a$ , and the lowest threshold pressure, $P_{M3}^S$ . (A, B, C) the displacement behavior varies according to the average deflation rate, $Df_r^a$ , in the 30-mm, 36-mm, and 41-mm cases, respectively. (D, E, F) the displacement behavior varies according to the lowest threshold pressure, $P_{M3}^S$ , in the 30-mm, 36-mm, and 41-mm cases, respectively. (G, H, I) The variations of displacement in the 30-mm, 36-mm, and 41-mm vertical pipes correspond to the thresholds of $P_{M3}^S$ , <i>i.e.</i> , 9 kPa, 12 kPa, 13 kPa, respectively. . . . .	85

6.7	The average locomotion speed of PFR in different inclined angles of pipe configurations . . . . .	87
6.8	The experimental set-up to indirectly evaluate the maximum traveling distances. (A), (B), (C) PFR carries extra mass and the equivalent length of tethers in the 30-mm, 36-mm, and 41-mm pipes, respectively. . . . .	88
6.9	The evaluation of PFR performance when coping with critical zones in pipeline systems by the empirical and simulation approaches. (A, B, I, J) PFR overcomes elbow turning sections in real conditions and in the simulation environment in (C, K). (D, E, F, H) PFR surpasses transition areas in real conditions, whose diameters vary from small to big ones, especially in (D, H), gravity against the forward motion of PFR. (G) PFR traverses a small-to-big transition area in the simulation environment. (L) PFR performs the steering ability by changing the rotation direction of the vibration. (M, N) PFR proceeds with inspection missions in dark conditions. The high-lumen LED is activated to support the record from the NanEye camera. In (D, H, I), the red dash circles demonstrate positions where PFR hangs its body to prepare for the upward motion against gravity. Note that the diameter dimensions in this figure stand for the inner diameters of the pipe. . . . .	90



# List of Tables

3.1	The detailed value of design parameters (Figure 3.3(b)). . . . .	21
3.2	The design parameter values of three patterns and their locomotion performance	31
4.1	The experimental values of oscillation frequency were determined from the piezoelectric disc and the mocap data processed by FFT at the applied voltage 3V, 4V, and 5V. . . . .	37
5.1	The average curvatures, $K_s$ ( $mm^{-1}$ ), derived from the obtained data set of the tracking position in $X$ and $Y$ direction. . . . .	73
6.1	The vibration frequencies and the corresponding amplitudes of the sinusoidal signals of the centripetal force. . . . .	81
6.2	The parameters applied to PFR to examine the average locomotion speed at different pipe inclination angles. . . . .	87
B.1	The experimental values for the analytical model. . . . .	105
B.2	The nodes' mass on Leafbot designs . . . . .	105



# Chapter 1

## Introduction

### 1.1 Background

Through the efforts to develop material technology in the last three decades, a new branch known as soft robotics has arisen from the robotics area. The adaptability and compliance inherent in soft robotics have unlocked a spectrum of possibilities for developing novelty designs. This advancement likewise allows for improvements in complex structures by integrating new features from state-of-the-art materials. For example, soft materials have been used to create bio-inspired robots [20–22]. The softness of rubber materials has advanced tactile sensors [23,24]. The adaptable and compliant nature of soft materials enables them to interact with the versatile morphology of handling objects [25]. Apart from developing novel applications for soft robotics, many researchers have been putting efforts into exploiting benefits from the intrinsic properties of soft robots to deal with difficulties that conventional robots or equipment, such as the lack of softness and compliance, might encounter. For example, this includes applying soft robots to human inspection [26,27] or studying various locomotion postures that rigid robots might find challenging to implement [28–30].

#### 1.1.1 Adaptive morphological designs of soft robots

This research aims to introduce the remarkable adaptability of soft robots, which makes them well-suited for tasks that require the robot to deal with complicated terrain conditions or variable working environments where traditional robots might need to be incorporated with complex physical structure (morphology) and computational algorithms to handle these missions. In the robotics area, the term *morphology* refers to the physical structures, form, and design of a robot, including the arrangement and configuration of its body and components. This term encompasses how a robot’s shape and features influence its functionality, movement, and interaction with the environment. The morphology of a robot is crucial for determining its

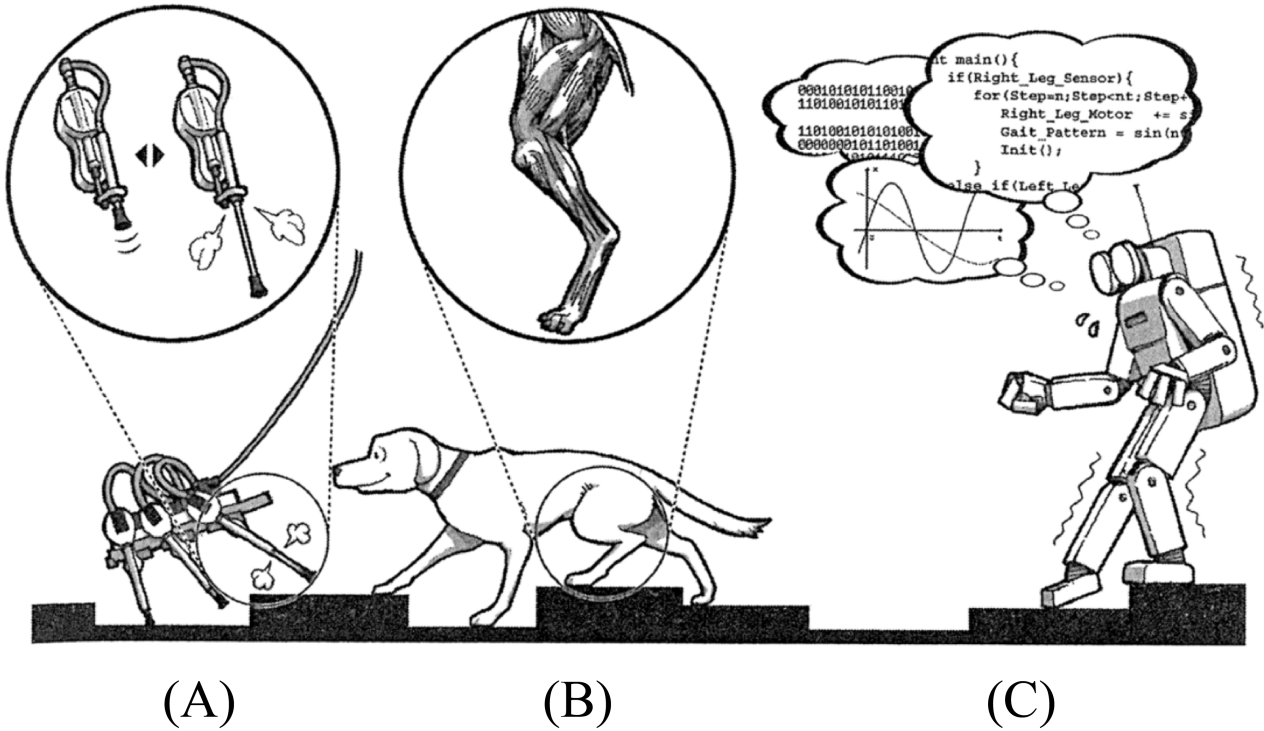


Figure 1.1: Morphological bodies facilitate the interaction with the environments to reduce the computational burdens (the picture adopted from [1]). (A) the sprawl robot leverages the material properties of its legs to achieve rapid locomotion. The elasticity in its linear joint, derived from the compressed air, allows the robot to automatically adapt its movement over uneven terrain, minimizing the need for complex computation. (B) The leg morphology of the animal, derived from the elasticity of its muscle, features an adaptive function, resulting in reducing the computation. (C) A robot constructed from rigid materials requires a complex control algorithm to adapt to uneven terrain, leading to significantly slowing down its movement.

capabilities, such as stability, adaptability, and efficiency in performing specific tasks [31, 32].

Robots with adaptive morphology can improve interactions with their environment, allowing adaptive functions without complicated control strategies. Adaptive morphology can be regarded as an aspect of intelligence. Traditional robots with fixed morphologies, such as industrial robots, require centralized controllers to perform complex computations for tasks like position control or force control, especially when encountering sudden environmental changes (see Figure 1.1). In contrast, a robot with adaptive morphology can adjust to environmental variations with minimal computational effort, as its adaptive structure inherently accommodates these changes locally. Consequently, adaptive morphology allows the robot to reduce computational demands for specific tasks, suggesting that intelligence is integrated into the physical body itself, known as embodied intelligence (see Figure 1.2).

Hawkes, E.W. et al., (2017)

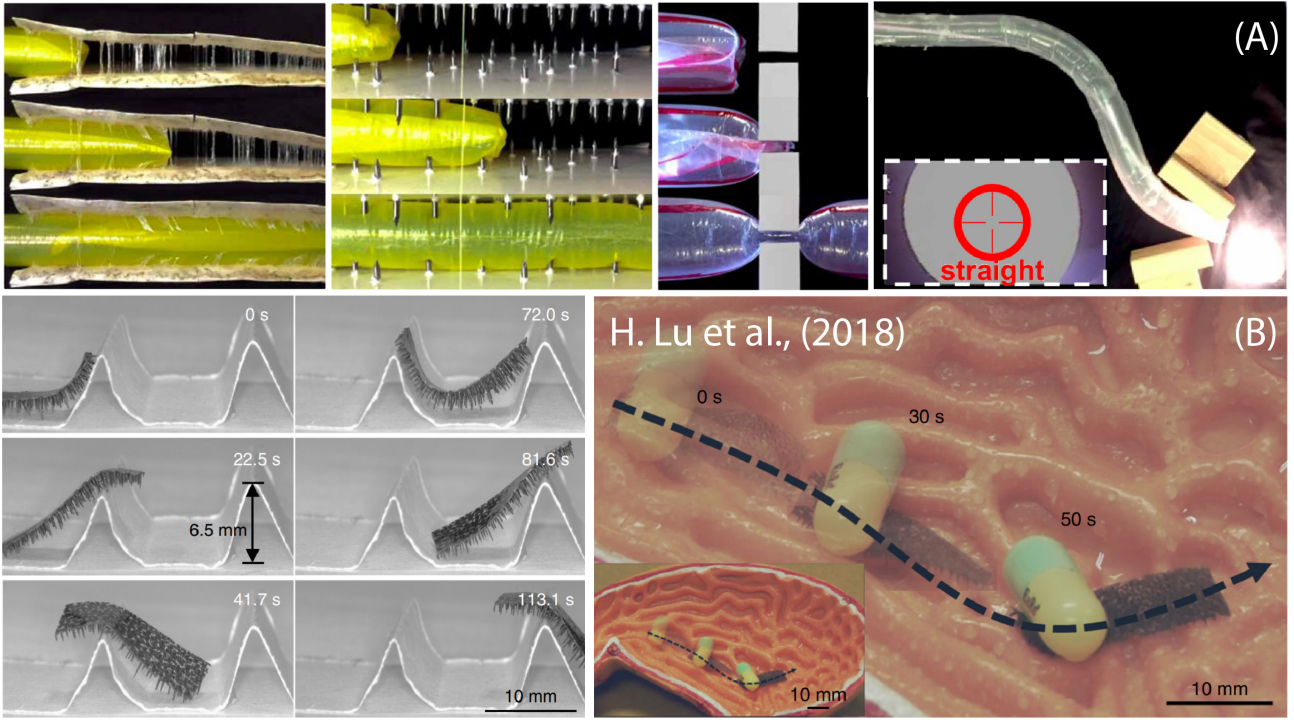


Figure 1.2: The remarkable adaptability and flexibility of soft robots advance the terrain's traversal with irregularities and complicated constraints that conventional rigid robots find challenging to be qualified for these tasks. (A) The soft robot with a moving mechanism is inspired by the growth of plants. It is well suited for variable-confined-hollow structures. (B) the multilegged miniature soft robot adapts to harsh environments where surface features are complicated. This soft adaptive design shows the potential for biomedical applications (the images adopted from [2,3]).

Therefore, soft robots have been drawing attention from researchers due to their potential for advancing adaptive functions to robot designs to target variable working environments. Additionally, soft robots have been demonstrating the potential for miniature robotic applications, whereas conventional robots with rigid mechanisms have been encountering challenges of scaling down. Thanks to the development of cutting-edge manufacturing technologies, researchers have been presenting many remarkable designs and materials that are suitable for the application of small-scale-driven mechanisms.

### 1.1.2 Locomotion of soft robots.

Locomotion in soft robots represents a significant advancement in robotics. Thanks to the integration of flexible, compliant structures, soft robots that mimic the movement and adaptability of natural organisms are allowed. Unlike traditional rigid robots, soft robots are capable of bending, stretching, and conforming to complex surfaces, allowing them to traverse



a variety of terrains with greater agility and safety. This unique mode of locomotion relies on innovative designs and materials that enable the robots to navigate tight spaces, climb uneven surfaces, or interact delicately with their surroundings. The study and development of soft robotic locomotion open new possibilities in areas such as search and rescue missions, medical procedures, and exploration of constrained and confined environments, showcasing their potential to revolutionize how robots move and interact with the world around them [33].

Numerous methods have been proposed for generating locomotion in soft robots, which can be grouped into six main gaits: crawling, legged, jumping, flying, swimming, and an alternative locomotion mode. While animal movements largely inspire most locomotion strategies of soft robots, there is a small group with locomotion principles that cannot match any biological creatures' motion postures thus far, for instance, vibration-based locomotion [33]. With terrestrial locomotion, *i.e.*, crawling, legged, and jumping strategies, the most common actuation mechanisms employed were Shape Memory Alloys, pneumatic, Dielectric Elastomer Actuators, and Motor, while with aquatic locomotion, Fluidic Elastomer Actuators and Shape Memory Alloys were the most preferences. The flying gaits, especially in flapping-wing flight type, integrated-driven mechanisms are various. A dominant mechanism has not been observed [34]. However, the scope of this study only focuses on terrestrial locomotion strategies. With the purpose of developing adaptive morphological designs of soft robots for small-scale works, the primary-driven source to generate locomotion should be taken into consideration to obtain miniature, compact, and lightweight structures.

## 1.2 Motivations and research questions

Despite the notable advantages of soft robots as well as substantial improvements in driven mechanisms for small-scale applications, there is not much in-depth research that features adaptive functions to deal with varying and constrained environments at small scales, such as rough and uneven terrains or variable cavity conditions, where current robotic designs are still facing difficulties in handling these certain tasks. Considering the robot's morphology, the working environments, and the way interaction occurs are the keys to developing smarter robot bodies with high adaptability and low computational burden. The ultimate goals of this study are **to develop two adaptive morphological designs of soft robots that can navigate varying terrains in two scenarios, including planar conditions and hollow-confined structures, such as pipeline systems, at small scales.** Adopting the *terradynamics*

study method to evaluate the traversability of the design concepts with variable terrains and constraints from environments. The term *terradynamics* will be explained in the following sections. However, to cope with small-scale applications for both terrains, there are concerns that need to be addressed; thus, the first research question would be:

**RQ1: What are the primary locomotion mechanisms that efficiently facilitate the adaptability of two designs and generate locomotion simultaneously?**

Because the selection of the driven mechanism directly influences the body structure, it leads to the second question:

**RQ2: How to accommodate the desired locomotion strategy for enhancing adaptive locomotion of soft robots?**

The study method to investigate and evaluate the capabilities of navigating the two aforementioned conditions is essential. Hence, the third research question is:

**RQ3: What methodologies can be employed to assess the locomotion performance of the proposed design?**

### 1.3 Originality and contributions

In the following sections, this thesis introduces the proposed methodologies to address the concerns above. These works demonstrate the advancements in the adaptive morphology field of soft robots. The originality and contributions of this dissertation are summarized as below:

- Two adaptive designs of soft robots were developed, named **Leafbot** and **PufferFace Robot-PFR**, to advance the capability of dealing with variable and complicated environments in two working scenarios, including the variable terrains in 2D spaces and the variable constraints in hollow-confined cavities, such as pipeline systems. The fabrication processes are fully addressed.
- The underlying physical phenomena caused by vibration mechanism are analyzed to construct the analytical model and Finite Element Analysis (FEA)-based simulation model.
- Taking the *terradynamics* features into account by adopting the geometry-based method to characterize terrains in the planar context to evaluate the traversability of **Leafbot**.
- Conducting the *terradynamics* study on **PFR** by assessing its traversability through variable and critical pipeline sections. PFR successfully adapts and navigates through

tubular sizes, ranging from 1 to 1.5 times the outer diameter of PFR in both horizontal and vertical configurations.

- The proposed analytical and simulation models can be generalized to other soft robots.
- Expand the possibilities of vibration-based robot class to work with irregular terrains rather than flat and even surfaces as previously developed designs.

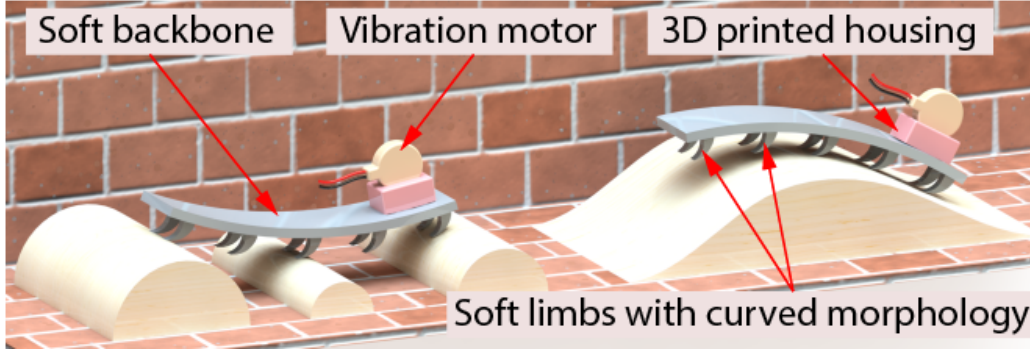
## 1.4 Significance

Adaptive morphology in soft robotics has been shown to be significant for handling variable and constrained environments without relying heavily on complex control algorithms. The robustness and resilience attributed to the hyperelastic properties of the silicone rubber material allow soft robots to withstand physical impacts or pressures that would damage more rigid systems. This makes them ideal for tasks requiring close interaction with objects or even humans. However, research in this field remains inconclusive. Thus, this thesis aims to conduct more in-depth investigations to extend the possibilities of soft robots with adaptive morphology by harnessing the intrinsic properties of soft materials and studying the *terradynamics* features of those proposed morphological concepts. This research lays a foundation for assessing the traversability of soft robots in complex and changing environments. This study also presents two soft designs with adaptability and flexibility that address the existing challenges in terms of dealing with variable terrains in planar and cavity spaces, which might potentially expand the robot’s capabilities to specific areas to deliver specific missions, such as human inspections and maintaining and inspecting small-scale pipeline systems, where current robot designs have not shown promising results

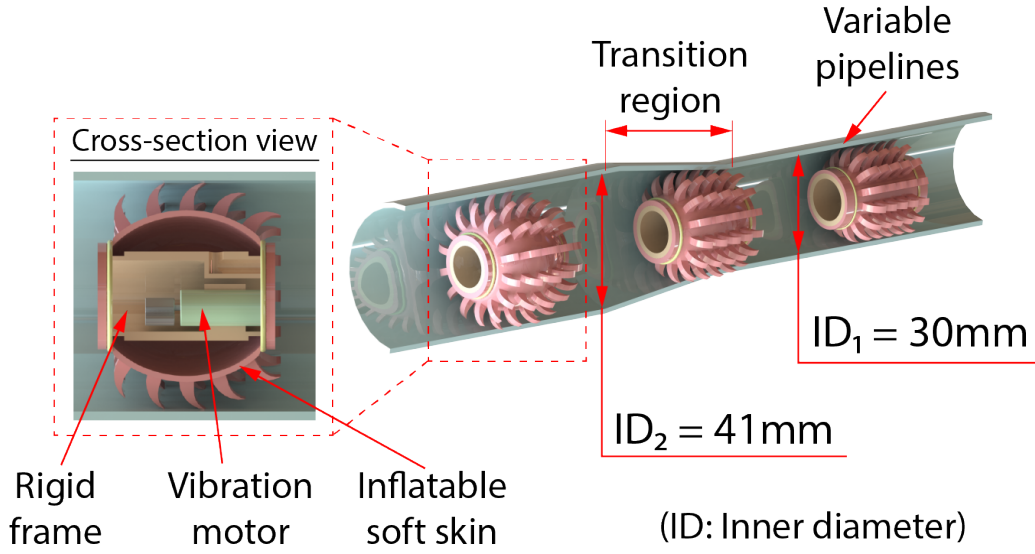
## 1.5 Proposing two morphological design concepts with vibration-based locomotion

Through a comprehensive review of the existing literature on soft robotics area, this research aims to introduce two adaptive morphology bodies incorporating vibration-based mechanisms. This approach is intended to tackle the challenges of achieving locomotion in diverse and complex environments at small scales.

The original motivation for employing vibration-driven mechanisms in these proposed concepts is derived from prior vibration-based studies of miniature robots [5, 6, 35–37]. In this



(a) The soft robot morphology adapts to obstacles and uneven terrain.



(b) The soft robot with inflatable morphology adapt to varying conditions in a pipeline system.

Figure 1.3: The proposed adaptive design concept for planar and variable-constrained cavity working conditions. The robot's hollow structure enables fluid and gas flow when operating in such conditions.

research, authors proposed rigid-body robot designs and obtained promising results in terms of velocity, modeling, robustness, and compactness. However, these models were typically found to focus on examining the dynamics characteristics of the robots with flat surface conditions rather than considering locomotion dynamics in rough terrain or complex environments, which is generally called *terradynamics* [16, 38]. Moreover, the analogous studies as *terradynamics* applied to hollow-confined structures, such as pipeline systems, have so far yielded limited outcomes. This study was inspired by both the effectiveness and the unresolved challenges of vibration-based locomotion. Figure 1.3 illustrates the vibration-based design concepts adapted for both planar environments and constrained-cavity conditions. The design model that addresses obstacles and rough terrains consists of two key components: a soft monolithic structure with a patterned limb morphology and a vibration-driven source. Similarly, the

design intended for variable and confined tubular environments features two main elements: a highly inflatable soft skin with a limb pattern and a vibration-driven source. In the next chapter, this work provides an overview of the developed design models for planar and tubular environments, offering readers deeper insight into the challenges and potential of soft-adaptive designs incorporating vibration-driven sources.

## 1.6 Dissertation structure

This chapter highlights the role of adaptive morphology in improving robots' ability to navigate diverse and complex environments, as well as the challenges that remain. It presents three key questions to tackle these issues, along with the research's contributions and significance. Additionally, it showcases two design concepts aimed at planar and tubular conditions. The following chapters of this dissertation are structured as follows:

- Chapter 2 summarizes developed vibration-based designs in planar and tubular contexts and the existing challenges. The *terradynamics* approach is presented in this chapter.
- Chapter 3 explains the fundamentals of vibration-driven locomotion and presents two adaptive designs for two working conditions and their fabrication techniques.
- Chapter 4 shows the analysis of physical phenomena attributed to vibration. The necessary parameters for the analytical and simulation models are thoroughly presented here.
- Chapter 5 showcases the vibration-based locomotion of Leafbot designs in uni-direction and 2D spaces. The justification of the analytical model and experiment and the terradynamics study to evaluate the traversability of Leafbot patterns with obstacles and rough terrains are all presented here.
- Chapter 6 showcases the locomotion vibration-driven locomotion of PFR design in pipelines. The experimental outcomes in various scenarios are demonstrated. The simulation outcomes are shown along with experimental outcomes in certain cases. The terradynamics approach is taken into account. This aims to assess the PFR's capability of coping with variable pipe sizes and critical sections of a pipeline.
- Chapter 7 summarizes challenges remaining in this study and future works.

# Chapter 2

## Related Works

### 2.1 Vibration-driven designs for planar working conditions

Regarding the vibration-based models working in 2D spaces, the most ubiquitous design model found is the bristlebot or brushbot [5, 6, 36, 37, 39]. A bristlebot design includes a miniature vibration motor mounted on a bristle head, which has elastic fibers referred to as bristles or brushes. During the operation, the eccentric mass from the vibration source generates a centripetal force. The asymmetric friction force phenomenon induced during a full cycle of centripetal force yields a net displacement [5, 39, 40], consequently resulting in locomotion if the rotation of the eccentric mass is provided continuously. The popularity of the brushbot is largely due to its brush structure, consisting of numerous small, inclined fibers with low-modulus elasticity. This design allows the brushes to deform easily under external forces, creating anisotropic friction. This is the basis of vibrational locomotion across various approaches. Consequently, vibration-driven locomotion can be applied to any asymmetrical structure, not just brushes. The typical source of vibration comes from a rotational eccentric mass attached to a DC motor or a piezoelectric stack actuator, which can produce vibrations at desired frequencies. Most vibration-based designs favor the eccentric mechanism due to its compact structure and low voltage requirements, whereas piezoelectric vibrators often need a high applied voltage, typically over 50 V [41]. Thus, these properties have the potential for integration into small-scale robots. Figure 2.1 illustrates vibration-driven designs for flat and even surfaces. These designs share a common feature: the asymmetrical structure of the robots' limbs, which is the foundation for generating forward motion in the vibration robot class, other than Figure 2.1D. This design uses a vibration source to create a vacuum effect, allowing the robot to securely adhere to flat surfaces while its movement is driven by two DC motors.

Furthermore, the dynamics of vibration-class robots and the contact mechanics between their limbs and the environment are complicated for mathematical models. Ioi *et al.* [36] presented a small vibration-driven design for planar locomotion by employing two tiny vibration

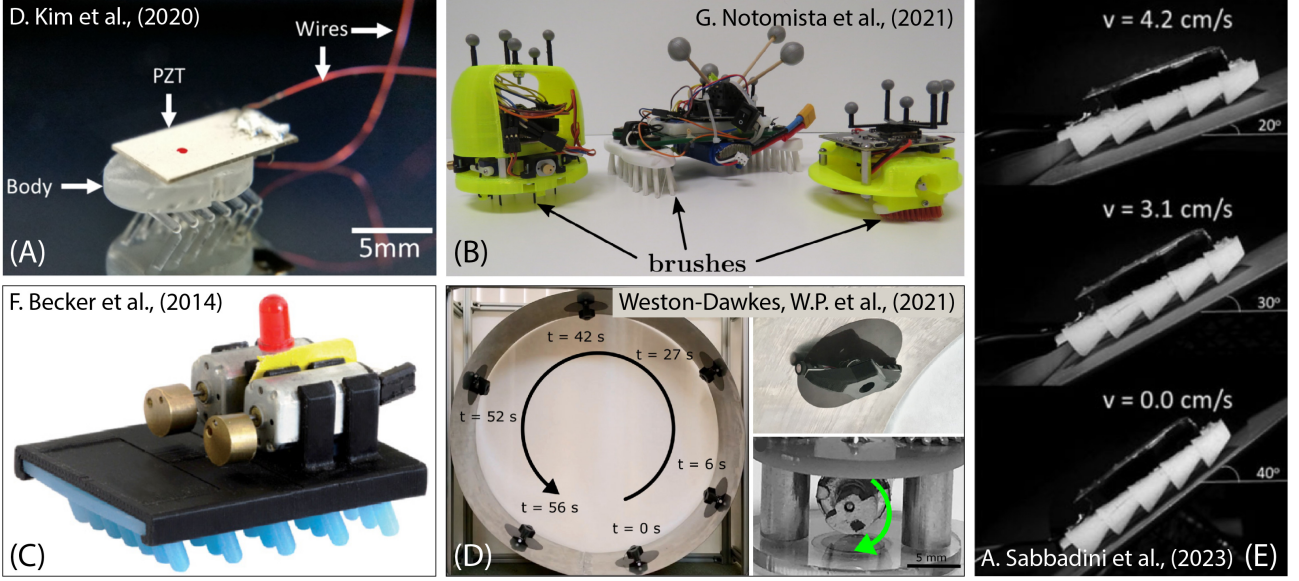


Figure 2.1: The developed vibration-based designs. (A) A miniature robot is driven by a piezoelectric stack. (B) One of the common designs of bristlebot is driven by an eccentric motor. (C) A rigid backbone is incorporated with inclined bristles and two vibration motors to generate forward motion. (D) A design takes advantage of the influence of the vibration phenomenon to create a vacuum state, causing the robot firmly suck to flat surfaces. However, the motion is manipulated by two DC motors. (E) A soft body with an asymmetric limb structure is integrated with a vibration source to induce forward motion (the images adopted from [4–8]).

motors mounted on a bristle piece. The author modeled the locomotion feature based on the elastic properties of the bristle cilia. Giomi *et al.* [35] also constructed their analytical model for their vibration-based swarm robot by considering the elastic features of the cilia. DeSimone and Tatone [40] utilized a simplified design of a vibration-based robot to investigate the frictional contact between robot limbs and substrate. Becker *et al.* [6,37], Notomista *et al.* [5], and Kim *et al.* [4] also adopted a similar method, taking the elastic properties and the asymmetric friction force into account, for the numerical calculation. In the most recent study of A. Sabbadini *et al.* [8], authors published a soft design integrated with a vibration source to generate forward locomotion. The basic principle of the motion was non-symmetric friction. They presented the dynamics study of their vibration-based model in planar conditions. The design featured a very good locomotion speed when encountering slope terrains. Thus far, most studies in the field of vibration-based robots have focused on delivering locomotion and clarifying the underlying physics of the locomotion posture on a flat and smooth surface. There is no extensive in-depth research focused on studying the behavior of vibration-driven robots when performing locomotion in complex environments, such as the traverse capability of a vibration-based robot

through obstacles or complicated terrains in 2D spaces.

## **2.2 Vibration-driven and other developed mechanisms for cavity working conditions**

Cavities with size-changing conditions, such as pipelines at the centimeter scale, are the target objects of this research. Pipeline systems are considered the most effective way of transporting gas and fluids in industrial factories, oil refineries, automobiles, machinery, spaces and aviation, etc. This type of transportation is regularly used for safe and cost-effective reasons [42, 43]. However, the pipeline networks are usually placed in enclosed and confined spaces, such as hydraulic oil or fuel systems in aircraft, cargo vessels, or gas systems in households, etc., which limits the approach of humans for proceeding with periodic maintenance. Therefore, the demand for having a tool or a method to inspect the conditions of pipeline systems draws attention from engineers and researchers. However, apart from the assembly condition, this type of transportation system is composed of not only a single-size pipe but a wide range of sizes, ranging from a few millimeters to several centimeters, and can have various shapes, from straight sections to sharp curves. They also cover significant distances, extending from a few centimeters to hundreds of meters. Regular inspections of both the exterior and interior of these pipelines are essential to ensure their reliable operation. To be deployed and used in such environments, various robots with different propulsion mechanisms have been developed [9], including wheel-driven [44–50], walking-based [51–53], crawler-based robots [13, 18, 54–59], vibration-based [60–62], and other locomotion mechanisms [63, 64].

However, adapting robots with these types of navigation mechanisms for use in smaller (centimeter-scale) pipelines has posed difficulties. Various studies have been exploring different strategies to address the challenges of miniaturizing conventional mechanical structures [9]. Bioinspired soft robots that utilize smart materials such as piezoelectric actuators [65–68], dielectric elastomer actuators (DEAs) [69–72], fluidic elastomer actuators [73–76], hydrogels [77–79], shape memory alloys (SMAs) [80–82], and magnetic actuators [83–85], for actuation have also been explored in prior research. These methods, which occupy less space, exhibit higher power and energy density, and are more adaptable to small-scale dimensions, offer distinct advantages for pipeline locomotion. Soft robots made from low-modulus materials, which mimic the elasticity of biological tissues, can passively adapt to varying dimensions and



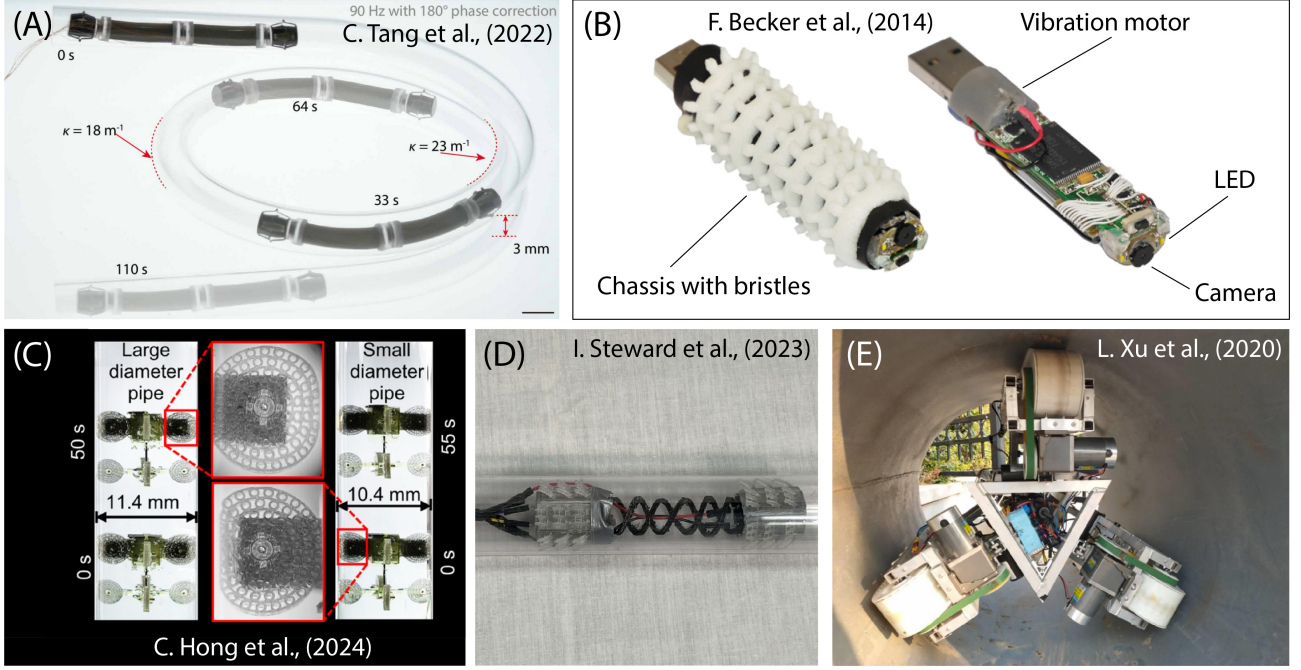


Figure 2.2: Several developed designs aim for various tubular environments. (A) A pipeline inspection robot for small-scale applications is driven by DEAs. (B) A vibration-based robot with an inclined bristles pattern was developed for inspection tasks. (C) A miniature robot incorporated kirigami soft wheels is driven by a wheel-based mechanism. (D) A vibration-based soft robot, including two sub-modules, facilitates complex navigation tasks in pipelines. (E) A rigid wheel-driven design robot adapts to various sizes of cylindrical channels (the images adopted from [9–13]).

shapes of pipes due to their flexibility and high adaptability. In pipeline inspection, the tubular environment can present challenges depending on factors such as curvature, the presence of substances within the pipeline, or transitions between different diameters. As a result, achieving agile navigation, effective inspection, particularly in small-scale pipes, and adaptability across different pipe sizes during inspection missions remains a significant challenge [9]. Figure 2.2 demonstrates several developed designs for pipeline networks. Figure 2.2A, B, C, D present studies that exploit the advantages of soft and smart materials to advance centimeter-scale locomotion. Nevertheless, these approaches still yielded poor adaptability performance in the variation of cavity environments. In contrast, Figure 2.2E represents a rigid traditional design exhibiting good adaptability but showing difficulties in miniaturizing.

### 2.3 Terradynamics study of vibration-driven robots.

Dealing with a 3D complex terrain during locomotion is always a matter of concern to robot researchers. To date, most robots have been designed to use their sensory systems to avoid

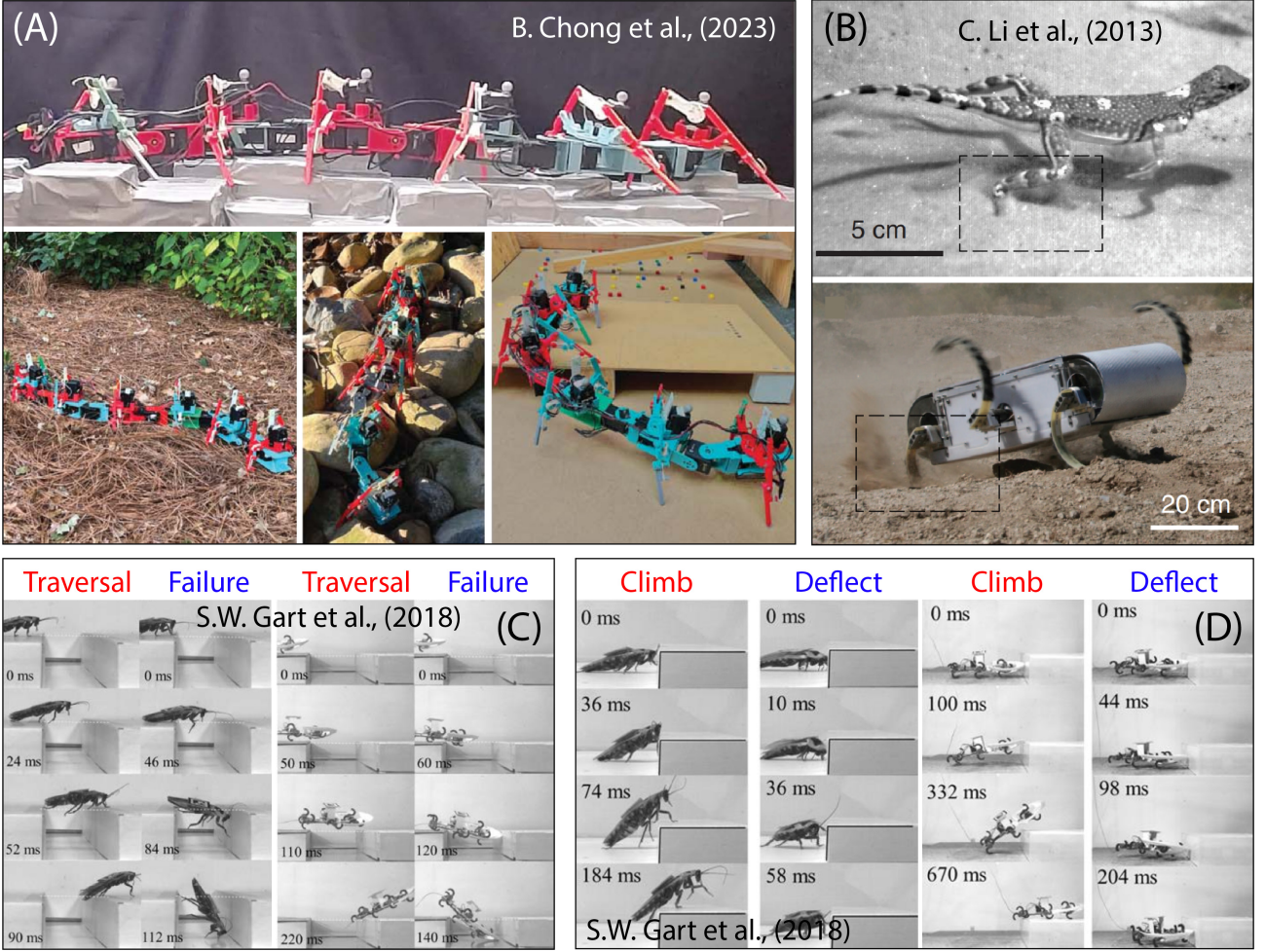


Figure 2.3: The *terradyamics* studies investigated how body morphology affects the traversability of robots with certain terrains. (A) B. Chong *et al.*, evaluated the relation between the redundancy of the number of robot’s limbs with the traversal to step-field terrains. (B) The *terradyamics* term was initially proposed by C. Li *et al.*, to assess the locomotion of their legged robot design with the granular media. (C), (D) S.W. Gart *et al.*, published studies that verified the traversability of their legged robots with large gaps and bumps (the images adopted from [14–17]).

obstacles or complex terrains, such as large gaps, bump-like obstacles, or high-slope terrains, instead of dealing with such environments [17]. However, in some specific scenarios, obstacle avoidance is not feasible, or overcoming such obstacles and complex terrains can enhance mission efficiency [86]. Therefore, many researchers put effort into studying the locomotion behavior of terrestrial animals when they cope with complex environments. These studies can form the basis for developing robot locomotion strategies to tackle sophisticated terrain [15, 16].

We found the *terradyamics* term for the first time in the study of C. Li *et al.*, (2013) [15]. In this article, the authors introduced a robot design that imitated the lizard locomotion for their robot to overcome the granular terrains at which wheel-mobile robots might encounter

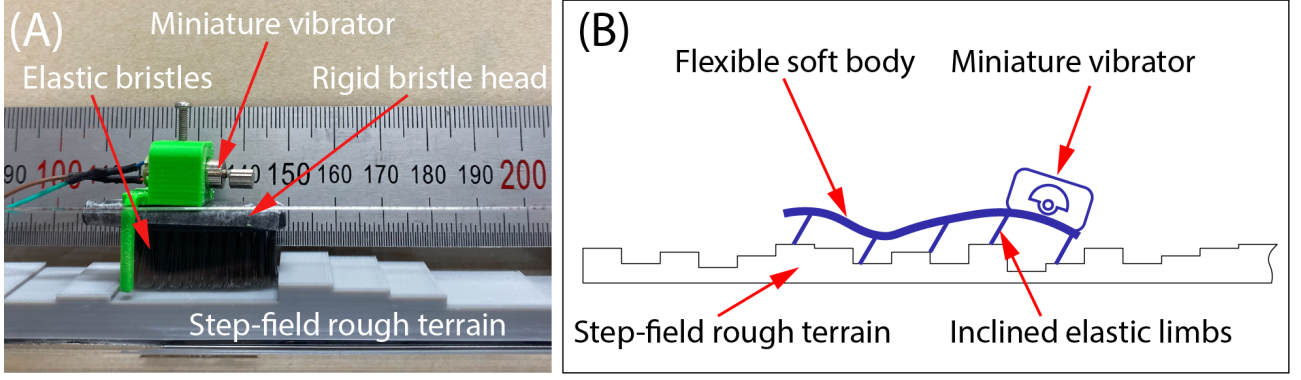


Figure 2.4: (A) The most common design in the vibration-based robot class is a bristlebot design. (B) Drawing inspiration from the bristlebot, we developed a vibration-driven robot with a flexible soft body to enhance its ability to navigate rough terrains. The design incorporates inclined elastic limbs, serving a similar purpose to the elastic bristles in brushbot designs, which is compulsory for generating forward motion.

difficulties (see Figure 2.3B). Five years later, in 2018, Chen Li and his team published additional research in the field of terradynamics. They revealed a template of the dynamic traverse of insects and legged robots when confronting large bumps and gaps during rapid locomotion [16,17] (see Figure 2.3C, D). Recently, another study demonstrated a methodology for resolving and evaluating the locomotion performance of their legged robot when traversing a step-field terrain [14] (see Figure 2.3A), which was constructed based on performance metrics that were utilized to assess the mobility of robots in simulated rough terrains [87]. However, in those earlier stated studies, authors employed a rigid-structure prototype to examine the terradynamics feature [15–17] or in the case of B. Chong *et al.* [14], the author utilized a multi-joint rigid body, which was snake-like design, to investigate the terradynamics in the step-field terrains. However, terradynamics study by soft robots has not been addressed.

From the above literature work, note that within this thesis, the scope of *terradynamics* is not only limited to 2D spaces but also extended to hollow-variable-confined structures. Such critical and challenging conditions are attributed to the variation in working constraints, which can be similarly considered as irregularities of terrains in planar contexts. Thus, in-depth research studying locomotion behavior in such “varying terrains” is essential. This research advances *terradynamics* investigations of both designs in two contexts, including flat working conditions and hollow-confined spaces.



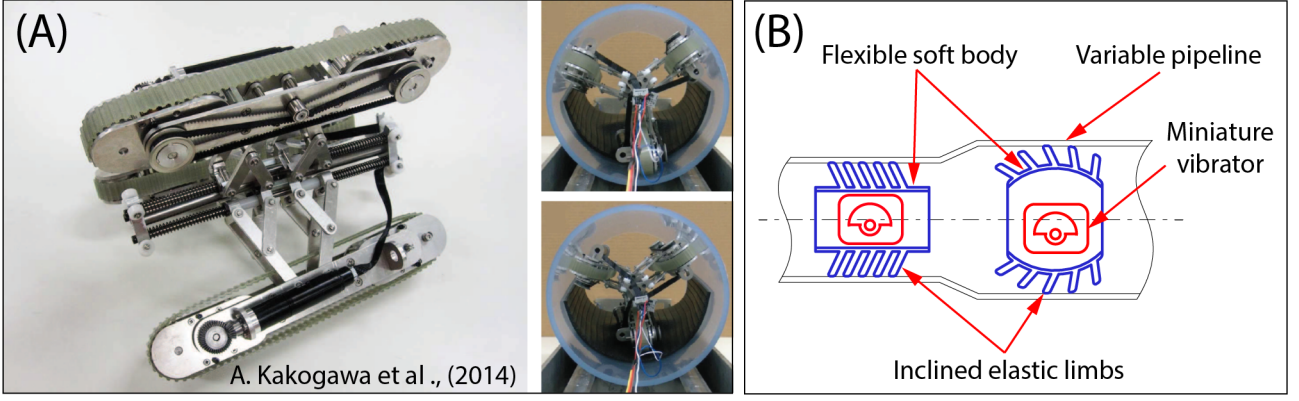


Figure 2.5: (A) A rigid design of the pipe inspection robot, equipped with an active size-adjustment mechanism, allows it to adapt to various pipe sizes (the image adopted from [18]). (B) A vibration-driven soft robot concept featuring a flexible soft skin allows it to adapt to different pipe sizes, with expansion achieved through an external compressed air supply. This concept aims for small-scale pipeline applications.

## 2.4 Vibration-based locomotion: one mechanism adaptable to both planar and cavity conditions.

As presented above, the most ubiquitous vibration-driven design is the bristlebot or brushbot. Figure 2.4A shows a conventional design of a bristlebot, which includes two primary components: elastic bristles attached to a rigid bristle head and a vibration source. The bristlebot offers several advantages, such as a high locomotion speed, a miniature and compact design, and a low voltage requirement. These benefits drew our attention to this type of mechanism. Nevertheless, this locomotion faces a significant challenge: its rigid body restricts its ability to navigate uneven and variable terrains. As illustrated in Figure 2.4A, this type of bristlebot is unable to navigate step-field terrains. To address this limitation, we modified the traditional rigid vibration-driven bristlebot by integrating the vibration source into a flexible soft body, which is expected to enhance its ability to navigate rough terrains. Our initial soft robot design concept, intended for 2D variable working conditions, was inspired by a regular bristlebot, as shown in Figure 2.4B. Further studies of this soft concept driven by a vibration mechanism with adaptability will be presented in detail in the next section.

The successful case of the initial vibration-driven soft model in the 2D space motivated us to apply this mechanism to variable cavity environments, such as pipeline systems. Various designs have been developed to meet the demand for pipeline inspection and maintenance. However, with advancements in manufacturing, pipeline networks have shrunk to centimeter-

and millimeter-scale dimensions, posing challenges for scaling down conventional designs. At larger scales, robots can incorporate rigid mechanisms (see Figure 2.5A) to adapt to changes in tubular environments. In contrast, integrating adaptive mechanisms at smaller scales is far more challenging. Nevertheless, the vibration-based approach is very compact and has the potential for application to small-scale pipeline networks. Thus, to address the existing challenges of miniature pipeline robots, we harnessed the softness once again to help the robot adapt to the size-changing tubular environments while combining with a miniature vibratory source. This integration was expected to resolve the existing barriers in two ways: vibration-based locomotion is feasible for small structure design, while the soft skin can facilitate the adaptability to diverse tubular shapes. A detailed exploration of this vibration-driven soft concept and its adaptability will be provided in the next section.

## Chapter 3

# Two Developed Morphological Designs of Soft Robot Driven by Vibration Mechanism

### 3.1 Vibration-driven locomotion mechanism

As presented in Chapter 2 and Section 3.1, the fundamental operation of vibration-based robots relies on the anisotropic friction mechanism and the influence of the centripetal forces induced by the vibration source. This locomotion mechanism has been applied to almost vibration-based designs. A simple forward motion of a bristlebot can be achieved using the concept illustrated in Figure 3.1. The bristlebot is equipped with a vibration motor, which includes rotational eccentric mass, to generate centripetal forces. When a rotation occurs, the motor's stator is subjected to a centripetal force. The centripetal force components in the  $X$  and  $Z$  directions are determined by the following relation, respectively (see Figure 3.1) [88]:

$$f_{cx}(\omega_v) = m_e e \omega_v^2 \sin \omega_v t, \quad (3.1)$$

$$f_{cz}(\omega_v) = -m_e g - m_e e \omega_v^2 \cos \omega_v t, \quad (3.2)$$

where  $m_e$  is the eccentric mass,  $e$  is the radius from the eccentric mass to the center of rotation (see Figure 3.1 and 3.3(a)), and  $\omega_v$  is the angular frequency of the vibrator. Figure 3.2 presents the principle of how vibration-based locomotion can be obtained. This mechanism is explained through two configurations, *i.e.*, vertical and horizontal configurations. The vertical one is also known as the stick-slip mechanism. In Figure 3.2A, the inclined limb is subjected to centripetal force in the  $Z$  direction,  $f_{cz}$ , causing deformation,  $D_z$ , then retrieval (stick-slip mechanism) on the limbs sequentially, resulting in a net displacement over one cycle of centripetal force. When the limb is compressed, a propelled force in the  $X$ -axis,  $F_x^{pot}$ , is generated simultaneously due to the resistance of friction force ( $F_{fr+}$ ) and the accumulated potential energy inside the limb.

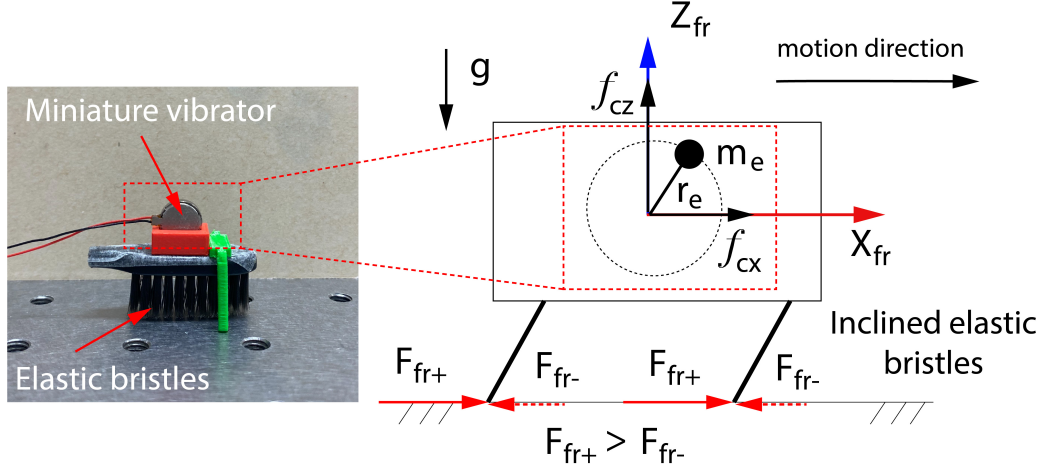


Figure 3.1: The vibration-based locomotion mechanism on a bristlebot. The bristlebot is represented by a rigid body with inclined elastic bristles. The non-symmetric friction feature is attributed to the inclination of the bristles. Under the excitation of the vibration source, a forward motion can be achieved thanks to the asymmetric friction mechanism.

Furthermore, when it is rapidly released,  $F_x^{pot}$  can induce a net displacement  $N_{D1}$  because the potential energy is transformed into kinetic energy. Owing to the non-symmetric feature of the limbs, the counter-friction ( $F_{fr-}$ ) yields less when the robot moves forward. Consequently, under prompt excitation, compression, and then release, the inclined limbs can generate a forward motion thanks to asymmetric friction. The forward motion in vertical configuration is activated if the centripetal force is maintained continuously. In addition, the robot might also be subjected to the centripetal force in the  $X$  direction,  $f_{cx}$ , if the rotational plane of the eccentric mass is parallel to the  $X$ -axis. Figure 3.2B exhibits the influence of  $f_{cx}$  in the  $X$  direction. The non-symmetric friction property also plays a vital role in facilitating the forward motion in the horizontal mode. Under the simultaneous effects of  $f_{cx}$  and the friction asymmetry, a net displacement  $N_{D2}$  is attained. The forward motion in the horizontal configuration is likewise initiated if the centripetal force is kept constant. For the vibration-driven robot class, the limb must be designed to have an angle of inclination instead of a vertically straight limb because this cannot feature asymmetric friction, which is necessary for vibration-based robots to move forward. This characteristic was proved in the prior study of L. Giomi *et al.* [35].

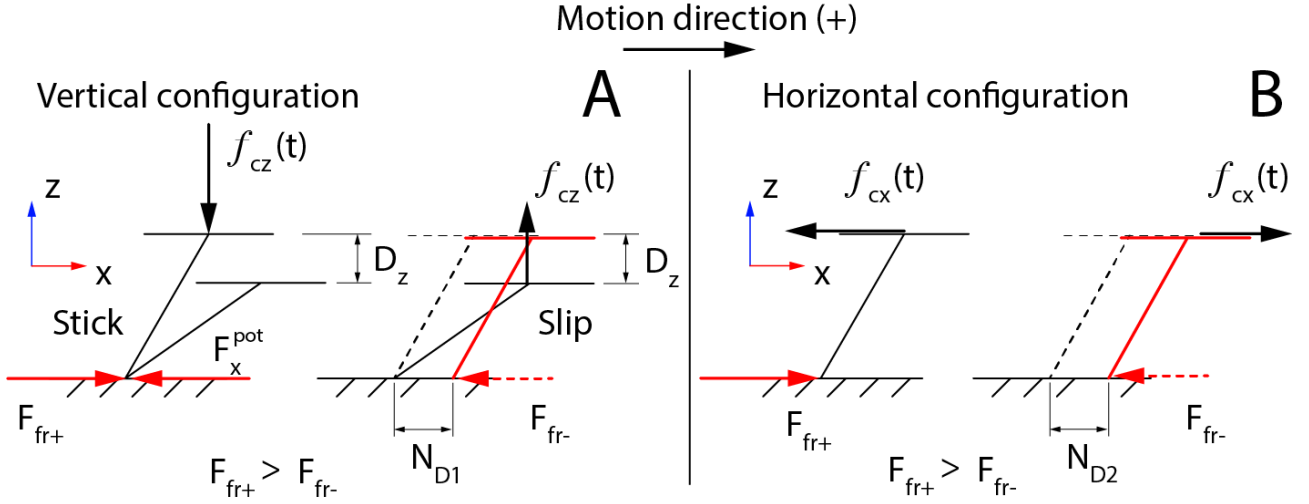
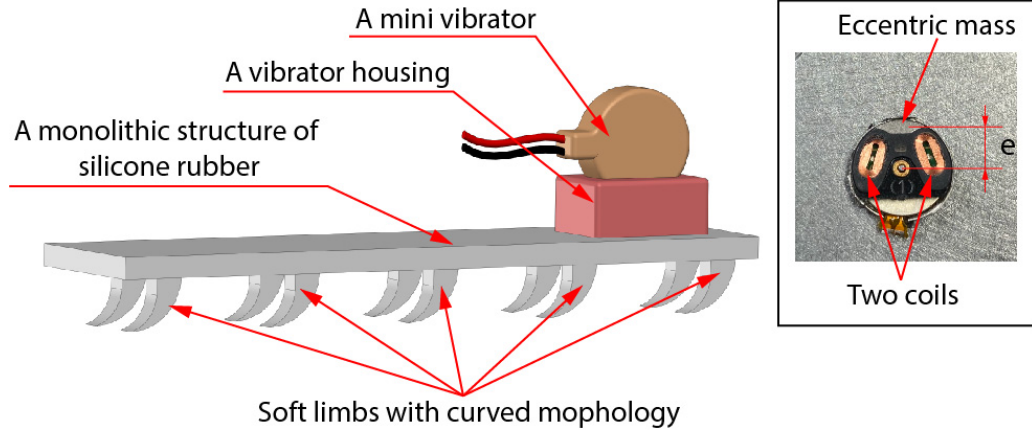


Figure 3.2: The stick-slip mechanism caused by anisotropic friction forces results in net displacements,  $N_{D1}$  and  $N_{D2}$ , over one cycle of centripetal force [5].

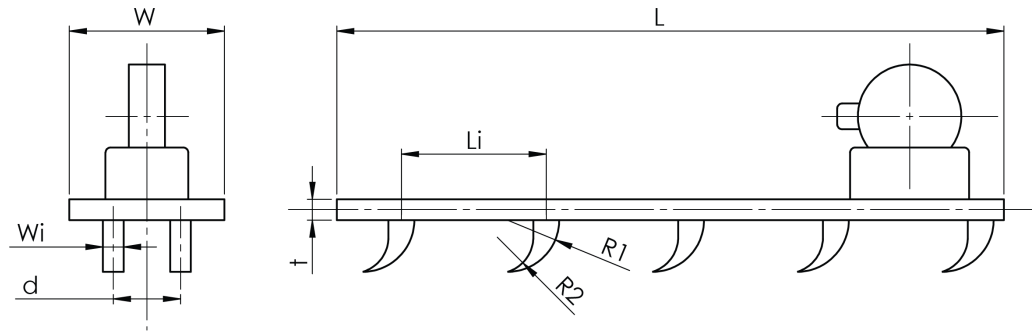
### 3.2 Two morphological designs of soft robot driven by vibration mechanism

We took advantage of the vibration mechanism to develop two design concepts for the robot with vibration-based locomotion. The first model specializes in working in planar conditions, whereas the second is only viable for constrained cavity environments. The asymmetric friction phenomenon between the robot's limbs and substrates primarily contributes to the induced locomotion of the robot. This non-symmetry feature can only be obtained thanks to the morphology of the limb. We developed a morphological design for the robot limbs that not only facilitates vibration-driven locomotion but also enhances the capability of dealing with specific terrain conditions. The general design of the first and second models is presented in the following sections. The limb morphology was initially developed and examined on the first robot operating in planar conditions; then, the design parameters were applied to the limbs of the second robot.





(a) The robot design comprises a monolithic structure of silicone, a mini vibrator, and a vibrator housing. The inset figure shows the inner components of a mini vibrator. The radius from the eccentric mass to the center of the rotation is  $e$ .



(b) The design parameters of the robot can be referred to Table

Figure 3.3: The general design of the robot: (a) The robot design components. (b) The design parameters.

### 3.2.1 Vibration-based robot design for planar working conditions - *Leafbot*

#### 3.2.1.1 Design

This section presents the design concept of a vibration-driven robot to work in planar conditions; we named it **Leafbot**. The design comprises a monolithic soft body with a morphological design of limbs. The motion of Leafbot is driven by a miniature vibration motor (see Figure 3.3). The backbone was constructed from soft material to leverage its flexibility and adaptability. The curved morphology of soft limbs was considered to assist the obstacle traversal of the robot, which was one of the objectives of studying the *terradynamics* of the vibration-based robot in planar conditions. A Finite Element (FE) analysis-based simulation engine, ABAQUS, was employed to aid the morphological study.

Table 3.1: The detailed value of design parameters (Figure 3.3(b)).

Design Parameters	$L$	$L_i$	$W$	$W_i$	$d$	$t$	$R_1$	$R_2$
Leafbot3 (mm)	64	28	15	2	6.5	2	5	3.5
Leafbot5 (mm)	64	14	15	2	6.5	2	5	3.5
Leafbot9 (mm)	64	7	15	2	6.5	2	5	3.5

### 3.2.1.2 Curved morphology of limbs

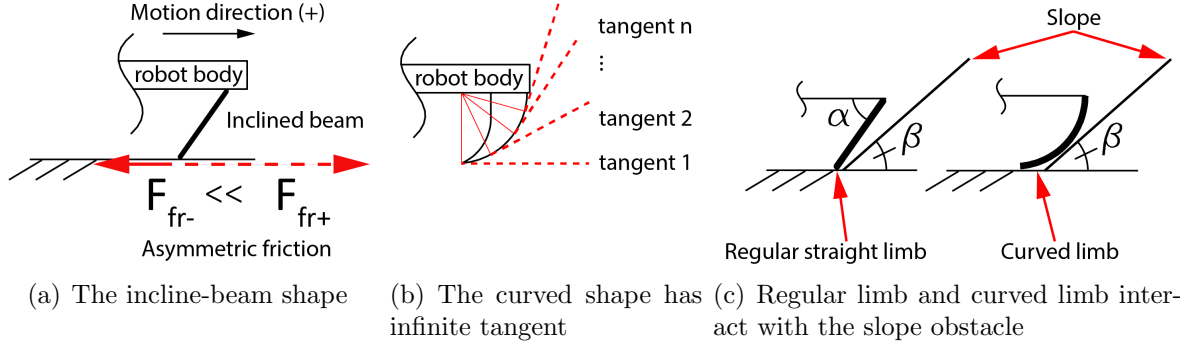


Figure 3.4: The morphology of the limb design: (a) The incline-beam shape. (b) The desired shape of limb design. (c) The simplified models of limb shapes are in contact with slopes.

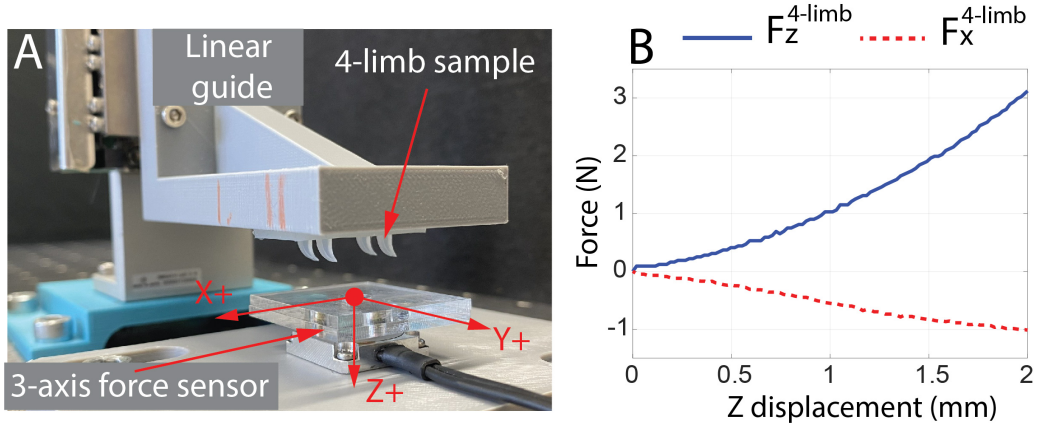


Figure 3.5: The experiment scheme to evaluate the propelled force when the limb is compressed. (A) Utilizing a 3-axis force sensor to collect yielded force data. (B) The acquired force graph.

The morphological design was inspired by the C-shape prosthetic legs; such a design was proven to transform the potential energy stored in the deformed legs into kinetic energy, thereby aiding forward movement [89,90]. The fundamental operation of the vibration-based robot is the induced asymmetric friction force between the Leafbot's limbs and the substrate. To achieve such a phenomenon, firstly, we considered the limb morphology as an elastic beam with a specific inclination angle (see Figure 3.4(a)). The inclined characteristic is required to provide the forward motion for the vibration-driven robot [4, 5, 40]. We justified this functionality via

an experimental set-up shown in Figure 3.5. The 3-axis force sensor employed is Tec Gihan USL06-H5. This examination presents two points:

- When the limb is compressed, a propelled force in the  $X$ -axis,  $F_x^{4-limb}$ , is generated simultaneously due to the resistance of friction force ( $F_{fr+}$ ) and the accumulated potential energy inside the limb. Furthermore, when it is rapidly released,  $F_x^{4-limb}$  can induce a forward motion because the potential energy is transformed into kinetic energy. Owing to the non-symmetric feature of the limbs, the counter-friction ( $F_{fr-}$ ) yields less when Leafbot moves forward. Consequently, under prompt excitation, compression, and then release, the morphological design of the limb can generate a forward motion thanks to asymmetric friction.
- The lumped stiffness of the morphological limb in the  $Z$  direction,  $k_z$ , which will be the input parameter for the analytical model, is determined. It is important to note that  $k_z$  will be treated as exhibiting linear behavior in the analytical model. In subsequent experiments analyzing the locomotion of the Leafbot, we observed that the displacement in the  $Z$  direction never exceeded 2 mm.

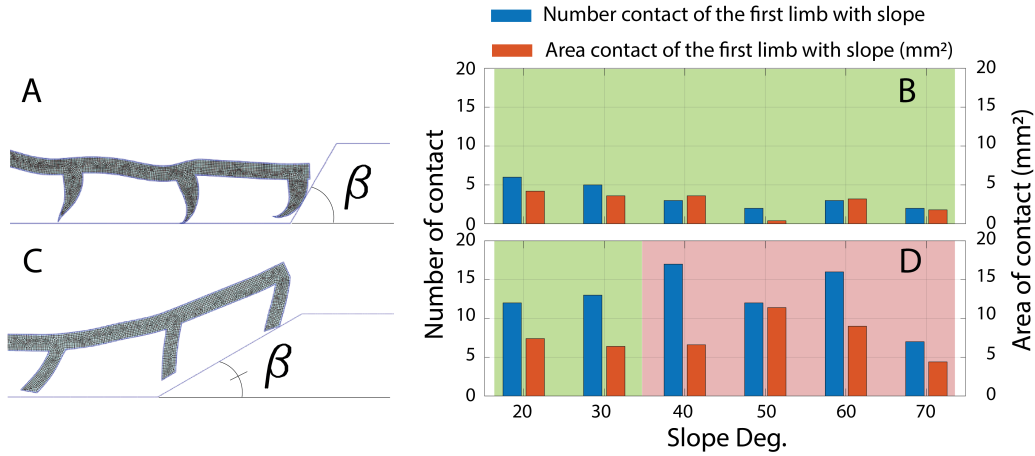


Figure 3.6: The ABAQUS simulation is conducted on two designs of limb, an inclined straight and a curved limb, to evaluate the contact features in terms of the number and area of contact with the sloped obstacles. (A) The curved limb interacts with the slope. (B) The results of the curvy limb. (C) The inclined straight limb interacts with the slope. (D) The results of the inclined straight limb. The red background implies the failure, while the green background implies the robot's success.

Secondly, to enhance traversal locomotion in complex terrain, a limb design should improve obstacle-overcoming capabilities. We initially planned to test Leafbot with sloped terrains. Most prior models of vibration-driven robots use the straight inclined design, which might not facilitate slope traversal because the limb's softness can cause the inclined limb to lean to the

slope and yield a line of contact with the slope, resulting in more friction and contact areas. More contact areas can also lower the propelled force of the limbs; consequently, it might not assist obstacle-overcoming capabilities. In contrast, a curved-shaped limb is considered to have an infinite number of tangents (see Figure 3.4(a) and Figure 3.4(c)); thus, whenever a curve interacts with an arbitrary slope, we can always find a point of contact between the curve and the tangent. This adaptive feature may allow robots to overcome various slopes more easily. We used a FEA-based simulation platform, ABAQUS, to justify this hypothesis. We assessed the performance of straight inclined and curved limbs by measuring the number and area of contacts with the slope until successful traversal. Figure 3.6A, C show the simulation of two limb designs with slope angles,  $\beta$ , ranging from 20 deg to 90 deg. The utilized simulation module was Dynamic Explicit, which effectively handles the non-linear models and large deformations of soft material due to their hyperelastic properties [91]. The Yeoh model was accommodated to simulate these hyperelastic characteristics properly [92]. The material constants applied to the Yeoh model and other setting parameters of the simulation model are presented in the Appendix A section. The results are depicted in Figure 3.6B, D. The curved design performs better, overcoming a maximum 70-deg slope (light green region), while the straight limb is halted at a 40-deg slope (light red region). Additionally, the curvy design also has fewer contact points and areas. These results suggest that our design takes less effort to surpass the slope obstacles. Consequently, we selected the curved shape for the limb morphology design (see Figure 3.4(a)).

Next, we took the front radius of the arc shape into account. We examined three radii ( $R_1 = 3\text{ mm}$ ,  $5\text{ mm}$ , and  $8\text{ mm}$ ) to determine the best locomotion speed. As shown in Figure 3.7, the  $5\text{ mm}$  radius performed best at  $3\text{ V}$  and  $4\text{ V}$ . Hence, we selected the curved limb with the front radius,  $R_1 = 5\text{ mm}$ . The final parameters for the Leafbot design were chosen based on these early evaluations and presented in 3.1. For details, refer to Figure 3.3(b), which shows the grid of  $5 \times 2$  limbs, representing five rows of two limbs each.

### 3.2.1.3 Design Patterns

In this research, we fabricate three limb-pattern models, including  $3 \times 2$ ,  $5 \times 2$ , and  $9 \times 2$  patterns to serve the *terradyamics* examination. To briefly distinguish between patterns, we name them **Leafbot3**, **Leafbot5**, and **Leafbot9**, respectively (see Figure 3.8). Table 3.1 presents each design parameter's value of three patterns. The front head of the robot is equipped with the

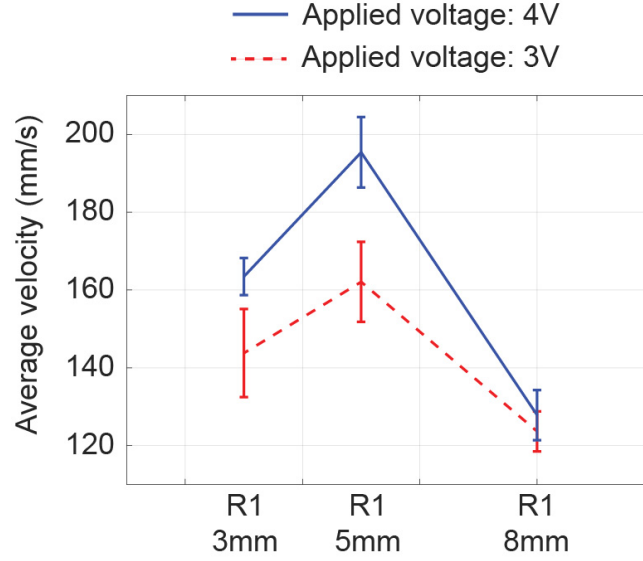


Figure 3.7: The obtained average velocity of three radius designs of the limb.

mini-vibration DC motor, which is mounted on the 3D printing housing. The entire robot body is a monolithic structure made of silicone rubber (Dragon Skin 30 material) that is fabricated via a special casting process.

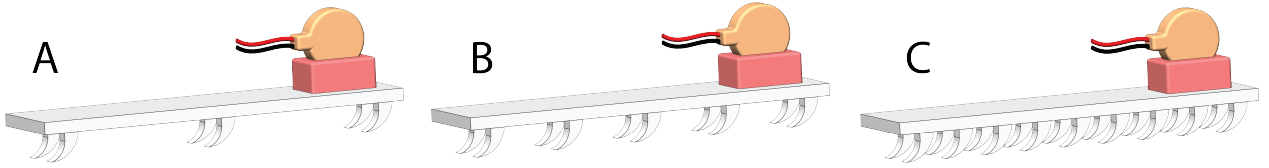


Figure 3.8: Three limb patterns were fabricated to study the terradynamics. (A) Leafbot3 pattern; (B) Leafbot5 pattern; (C) Leafbot9 pattern.

#### 3.2.1.4 Fabrication process

To fabricate this design as a monolithic silicone structure, we used silicone casting. This required first creating a mold for the robot body. Due to the complexity of the limb geometry, 3D printing was challenging for support removal. Instead, we applied another technique common in the metal casting process. The mold for the soft robot body was created from a specialized silicone rubber, Mold Star 16 FAST, of Smooth-On. The core that forms the hollow space for the robot body is made from an acrylic sheet shaped by a laser-cutting machine, with the sheet's thickness determining the limbs' thickness ( $W_i$ ). After laser cutting, the cores are assembled into a 1:1 scale model of the design. This acrylic body is then embedded in the Mold Star 16 FAST compound, which hardens in 45 to 60 minutes. Once cured, the core is gently removed

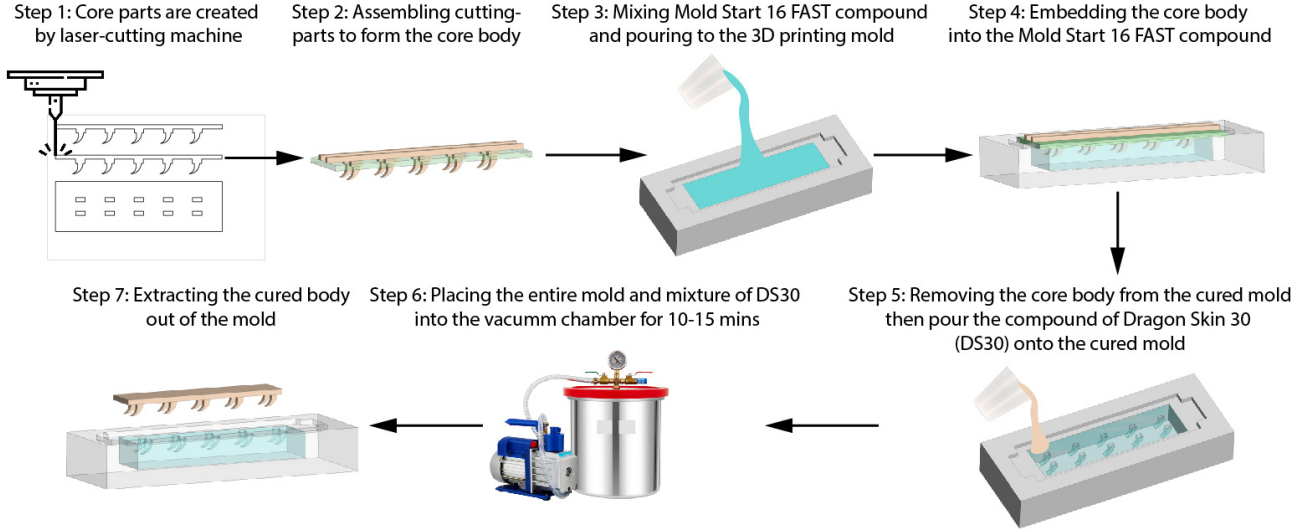


Figure 3.9: The fabrication process of the monolithic soft body.

from the silicone mold. Finally, Dragon Skin 30 silicone is poured into the cured mold. Due to the small limb spaces, the mold is placed in a vacuum chamber for 10 to 15 minutes to ensure the silicone fully fills the hollow spaces. The fabrication steps for the monolithic soft body are shown in Figure 3.9. The soft body can be extracted from the mold after 10 to 12 hours. After obtaining the soft body, a DC vibrator is securely attached to the 3D-printed housing and bonded to the soft body using Smooth-On’s Sil-Poxy adhesive.

### 3.2.2 Vibration-based robot design for constrained cavity conditions - *PufferFace Robot (PFR)*

#### 3.2.2.1 Design

In this study, we introduce a novel concept of soft robots with adaptive morphology designed to enhance interaction between the robot’s body and the surrounding environment through simple vibrations, enabling traversal through cavities. Figure 3.10 demonstrates our model concept. The robot design concept was inspired by a pufferfish (see Figure 3.10C), leading us to name it PufferFace Robot (PFR). In addition to the inflation/deflation mechanism that motivated the development of an adaptive design for varying cavity environments, the robot’s front view resembles a pufferfish’s face. For this reason, we included “Face” in the robot’s name to easily associate our nature-inspired design concept with a natural creature, the pufferfish. The robot concept features a soft, inflatable skin covered with an array of flexible limbs. While the pufferfish’s morphology enhances its ability to evade predation and increases its survival chances

in the wild, our robot’s similar morphology improves adaptability to surrounding cavities and facilitates vibration-induced locomotion. Three major contributions have been emphasized in this study:

- The adaptability to the varying cavity environments.
- The hollow structure facilitates the flow of gases and fluids during the inspection operation.
- The adaptive morphology enables PFR to traverse complicated constrained tubular conditions with a simple control strategy.

The proposed PFR needs to be capable of propelling itself in confined and/or constrained environments of various sizes. Considering the characteristics of the environments in which it will be applied, the proposed robot should be miniaturizable, capable of a wide range of size adjustments, self-propelled, and easy to fabricate to ensure fulfillment of the above-mentioned requirements. Figure 3.10A shows the constrained working conditions, *i.e.* pipeline networks, in industrial manufacture. These pipeline systems are normally constructed from various sizes and geometries. As a consequence, the robots aiming to apply to this field need to be equipped with the adaptive morphology property to flexibly adapt to variable cavity environments (see Figure 3.10B). The proposed concept can actively enlarge or contract its soft body to fit with specific cavity conditions. The size of soft skin of PFR can vary from 1 to 1.5 times the outer diameter of PFR at the normal state (see Figure 3.10D, E).

The 3D design model of PFR is demonstrated in Figure 3.11. As shown in Figure 3.11A, PFR includes three main components: a vibration source selected from a DC eccentric motor, a hollow-shape rigid frame, and an inflatable torus-shaped soft balloon incorporated with a soft “spikes” pattern, which is similar to the skin surface of a pufferfish. The barbs on the skin of pufferfish brought us the idea of employing a vibration mechanism to generate locomotion, which is compact to integrate into PFR’s body structure. Nevertheless, the soft spike design is required to ensure the asymmetric friction distribution at the tips of the spikes. **Thus, the soft spike morphology was inherited from the morphological design of Leafbot’s limb. Note that because the soft spikes play a vital role in contributing to the motion of PFR, we might use three words, *i.e.*, “limb”, “spike”, and “barb” interchangeably hereafter within this thesis.** An air pressure hose connected to the rigid frame enables the inflation and deflation of the balloon, allowing the conformable body of PFR to adapt easily to various tubular diameters (illustrated in Figure 3.10 B, D). Additionally, a DC vibration



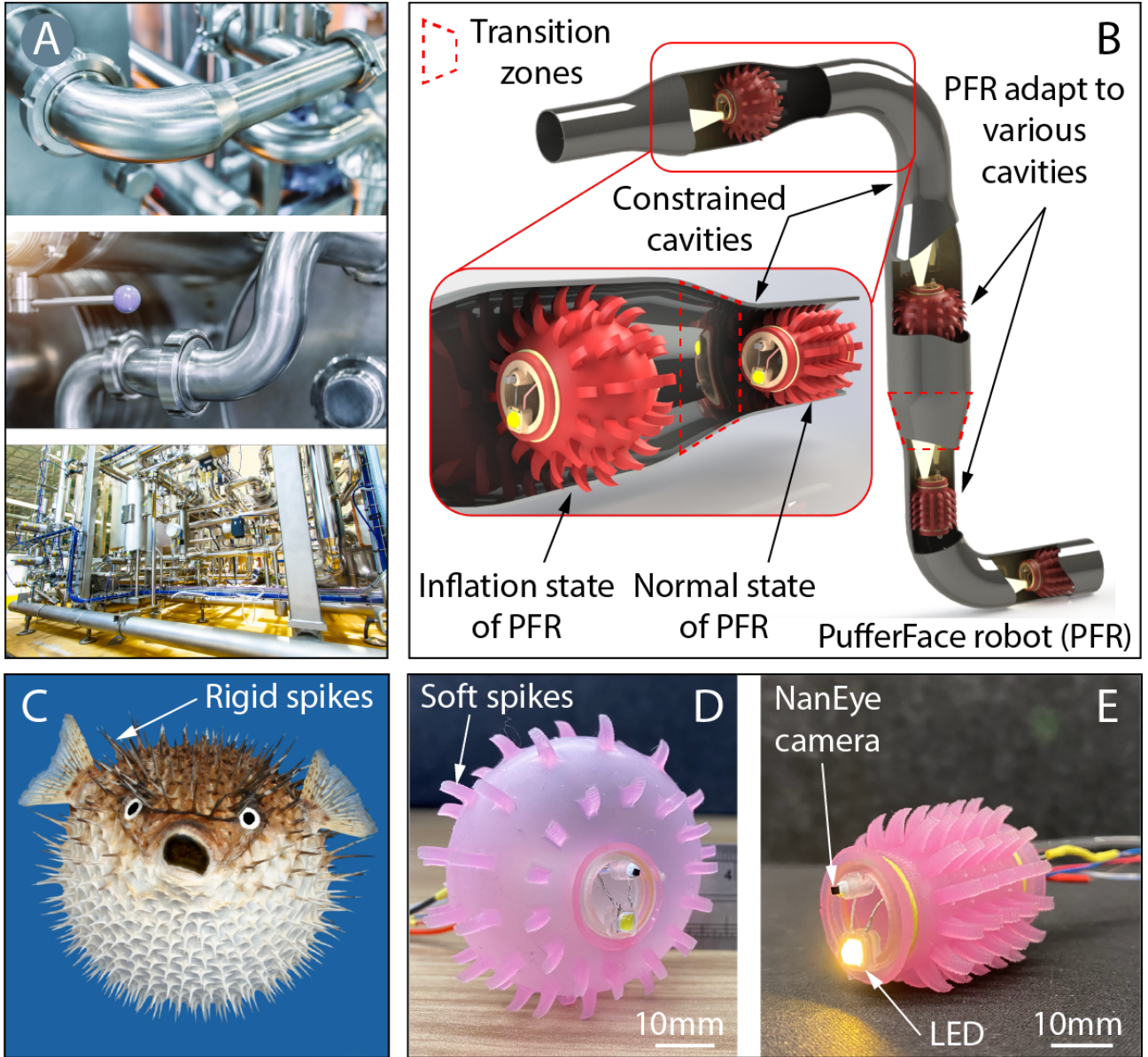


Figure 3.10: (A) Examples of cavity conditions in industrial applications. (B) The concept of a vibration-propelled robot with an inflatable structure that is capable of adapting to various cavities' working conditions. (C) The model design drew inspiration from a pufferfish. (D) PFR is in the inflation state. (E) PFR is in the normal state. PFR is equipped with an LED and a tiny NanEye camera to serve inspection tasks in dark conditions.

motor, a miniature camera (NanEyeM model manufactured by AMS OSRAM), and an LED are installed within the rigid frame, supporting both the self-propulsion and inspection capabilities of the proposed robot in constrained environments. Note that the hollow-shaped frame and torus-shaped balloon mechanism is designed to adapt to inspection environments with liquid or gas flows.

The proposed design for the PFR presents advantages capable of concurrently fulfilling all the aforementioned design requirements:



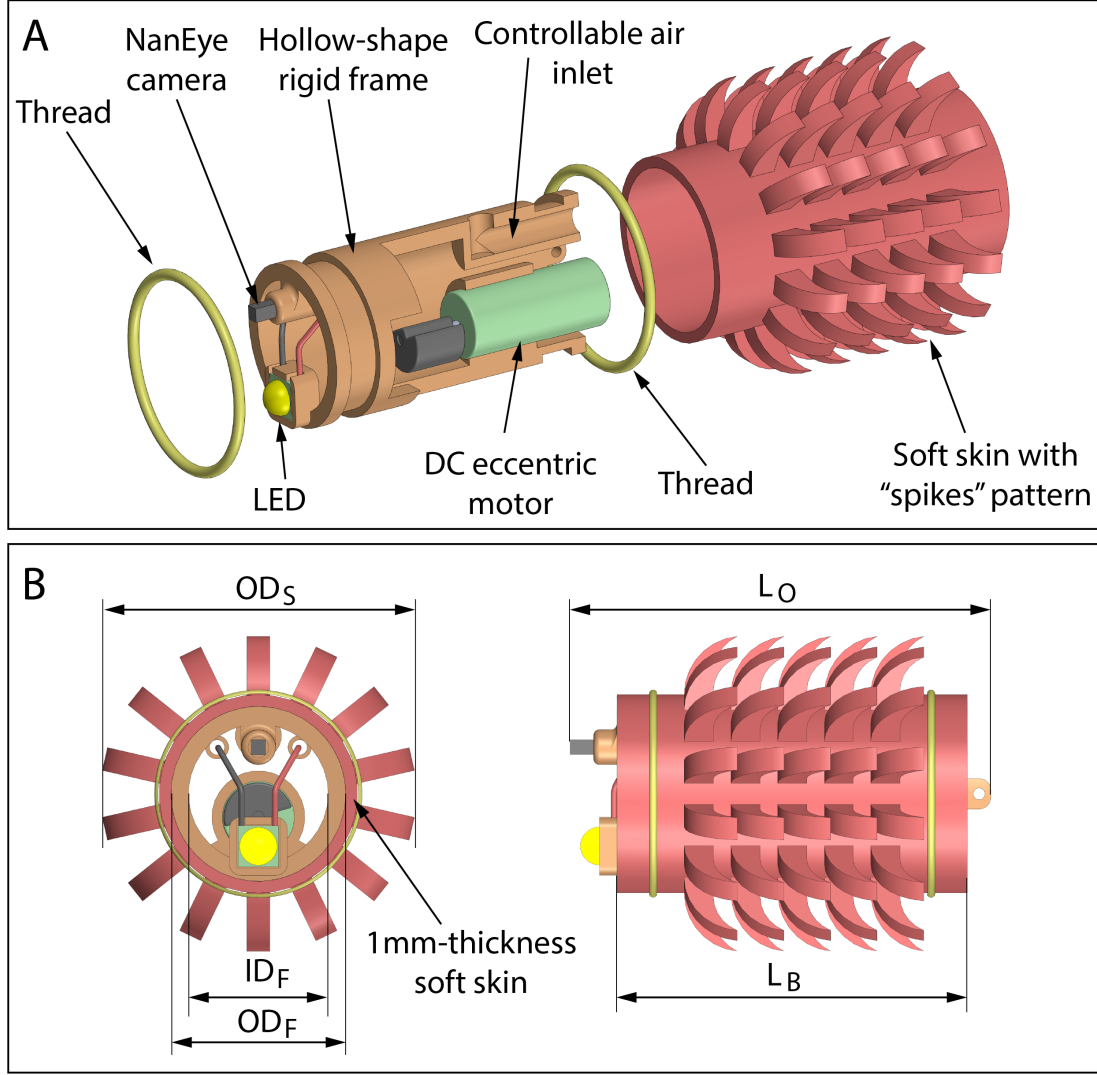


Figure 3.11: The 3D design model of PFR: (A) the component's view of PFR. (B) The front view and side view of PFR are shown with the dimensions, including the frame inner diameter  $ID_F = 12$  mm, the frame outer diameter  $OD_F = 15$  mm, the 1mm-thickness soft skin outer diameter  $OD_S = 27$  mm, the length of the PFR body  $L_B = 30$  mm, and the overall length of the PFR  $L_O = 33$  mm, when it is in the normal state.

- As shown in Figure 3.11B, the overall size of the robot is miniaturized and compact before the soft skin inflates, making it suitable for applications in tight and confined spaces. The thin thickness and high elasticity of the soft skin allow for significant diameter changes with small variations in air pressure and effectively conform to asymmetric internal geometries of pipes when PFR experiences the inflation state (Figure 3.10D).
- Considering the viable flow of fluids or gases in the environment where the proposed PFR is utilized, the overall structure of the robot, responsible for rigidity, is designed in a hollow-shaped. Figure 3.11A illustrates the completed mechanical configuration of the proposed PFR. This robot comprises two primary components, as shown below.

- By combining the vibration generated by the miniature vibrator and the inflation/deflation activated by the pressurized air, PFR can perform adaptive locomotion to overcome critical constrained conditions that are regularly found in pipeline networks without involving complex control algorithms. This adaptability is attributed to the hyperelastic feature of the soft skin and spikes.

Regarding *the hollow-shaped rigid frame*, in order to minimize the overall size of the robot, the frame incorporates multiple essential components: The camera and LED for inspection are attached to the front section of the rigid frame, while the eccentric DC motor for self-propulsion is installed inside the rigid frame to ensure operational stability. The rigid frame incorporates two peripheral notches to securely fix the soft skin in place and prevent any air leakage. The soft skin is fixed on the rigid frame through a knot of thread. The dimensions of the rigid frame are established according to the inner diameter of the inspection environment. In other words, the diameter of the robot, including the soft skin before inflation, should be smaller than the minimum inner diameter of the inspection environment. Given these design specifications and to ensure broad applicability without loss of generality, the following dimensions and specific components were chosen for this study: inner diameter  $ID_F = 12$  mm, an outer diameter  $OD_F = 15$  mm, and a total length  $L_B = 30$  mm. Based on these dimensions, a polyurethane tube (TU0212C-20, SMC) was employed as the inflation line for the soft skin.

### 3.2.2.2 Morphology of PFR

This section introduces the development process of obtaining design parameters of PFR's body morphology. Our purpose was to create a robot that can traverse and adapt to variable cross-section sizes of pipeline systems at a centimeter scale. Therefore, the general geometry property of the design is vital because pipeline networks might be constructed with critical sections, *i.e.*, the elbow turning and T-connector sections, which restrain the robot motion. To overcome these constraints, the study of H.R. Choi et al. (2001) [44] suggested that the total length and diameter of the robot should be determined according to the smallest radius of the pipeline curvature, or the motion robot will be impeded at the elbow turning sections. Consequently, we determined that the ratio between the length and diameter should be approximately one in our context. Based on the dimensions of the selected DC vibration motor and the ratio requirements for the robot in a constrained pipeline network, we initially determined the preliminary values of the total length,  $L_B = 30$  mm, and the outer diameter,  $OD \approx 26$  mm – 32 mm, for the robot

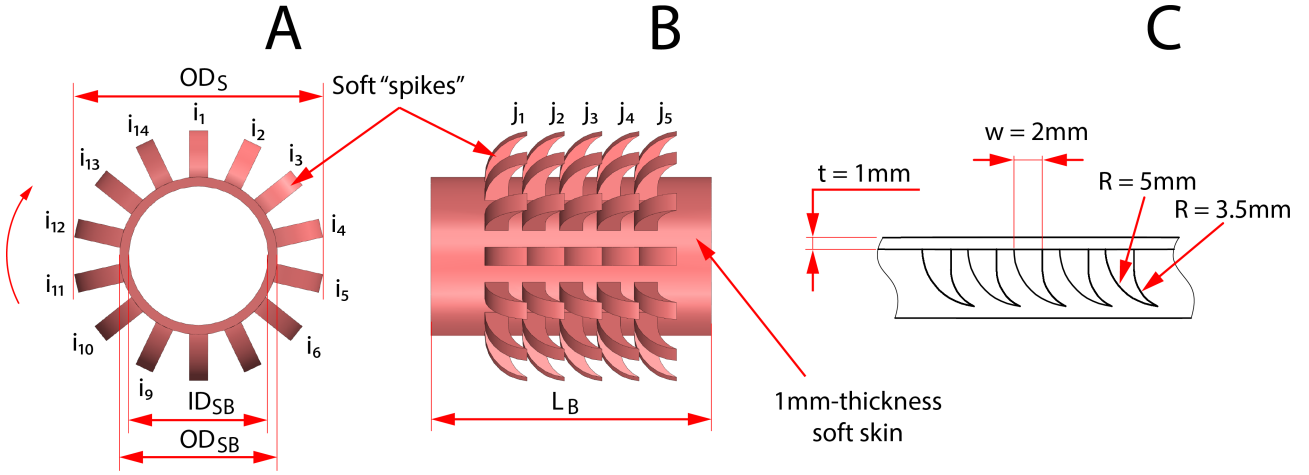


Figure 3.12: The dimensions of PFR's parts. (A) the front view of PFR;  $OD_S = 27$  mm,  $ID_{SB} = OD_F = 15$  mm,  $OD_{SB} = 17$  mm; (B) the side view of PFR;  $L_B = 30$  mm. (C) The cross-section of the 3D printing mold presents the dimensions of the soft spike.

configuration. Subsequently, it is essential to analyze and select the shape of the robot limb so that the robot can obtain locomotion when it is subjected to the oscillation frequencies from the vibration source. Nonetheless, as presented above, the soft limb design parameters of PFR were inherited from Leafbot, which was proven to generate vibration-driven locomotion efficiently.

Next, we developed three prototypes to evaluate the locomotion performance between different patterns. Figure 3.12 exhibits the dimensions of PFR's design. Figure 3.12A and Figure 3.12B demonstrate the pattern of PFR, which is characterized by the number of  $i$  and  $j$ . Table 3.2 shows the design parameters of three patterns and their locomotion performance. The first model cannot advance, while the third exhibited extremely low locomotion speed. Only the second model achieved the best locomotion speed and adapted to a cavity 1.5 times larger than its outer diameter. In the first model, the limited number of spikes failed to generate sufficient thrust, causing it to remain stationary. In contrast, the third design added more spikes, which increased its size and mass, leading to a considerably slower movement speed. As a result, we chose the second design (see Figure 3.12), as it met our initial objective of being capable of navigating through a pipeline system with varying cavity conditions.

The 1-mm thickness of soft skin with a spike pattern (see Figure 3.11F and Figure 3.11G) plays an important role in generating propulsion force and adapting to the variety of working cavities. During locomotion, the behavior of spikes can be compared to spring-damper systems. They are compressed and then rapidly and consistently released under high-frequency excitations from the eccentric DC motor, propelling the PFR forward. These spikes are integrated into a monolithic structure with the soft skin, which is required to inflate and

Table 3.2: The design parameter values of three patterns and their locomotion performance

Prototype	$L_B$ (mm)	$OD_S$ (mm)	$OD_{SB}$ (mm)	$ID_{SB}$ (mm)	$i$	$j$	Locomotion performance
First design	30	27	17	15	$i_1$ to $i_{10}$	$j_1$ to $j_3$	Unable to move forward
Second design	30	27	17	15	$i_1$ to $i_{14}$	$j_1$ to $j_5$	Able to move forward
Third design	30	31	21	19	$i_1$ to $i_{18}$	$j_1$ to $j_5$	Able to move forward with very slow velocity

deflate in a proper sequence, allowing the robot’s skin to match the inner diameter of the tubular environment without impeding its forward movement. The selection of the skin’s material is paramount due to the characteristics of the locomotion strategy of the PFR. The spikes might produce insufficient propulsion force if their stiffness is low; however, applying a material with high shore hardness could hinder the inflation process of the skin. Therefore, the mechanical properties of the soft skin material should be thoroughly considered. After working on several prototypes ranging from 00-10 to 30A Shore Hardness, we concluded that the most suitable stiffness for our application is 10A Shore Hardness. The silicone rubber utilized for the 1-mm soft skin is the Dragon Skin 10 MEDIUM (DS-10M), a product from Smooth-On. As presented above, although the geometrical parameters of the morphological spike design (also called morphological limbs in the Leafbot model) remain unchanged, the mechanical properties of the spikes still rely on the soft skin material because they are fabricated as a monolithic structure.

### 3.2.2.3 Fabrication process

The fabrication process of the soft skin with a spike pattern is shown in Figure 3.13. In Step 1, we initially utilized an FDM 3D printer (Raise 3D Pro2 Series, RAISE3D Inc.) to create a mold, which includes spike shapes. In Steps 2 and 3, the silicone (DS-10M) was poured into the mold and thoroughly degassed. To get the air bubbles removed from the compound of Dragon Skin 10A and 10B efficiently, we recommend putting the pre-mixed part A and part B of Dragon Skin 10 into the fridge for one hour before mixing them and keeping the mixture in the vacuum chamber for at least 10 minutes. By this method, we achieved soft-skin samples

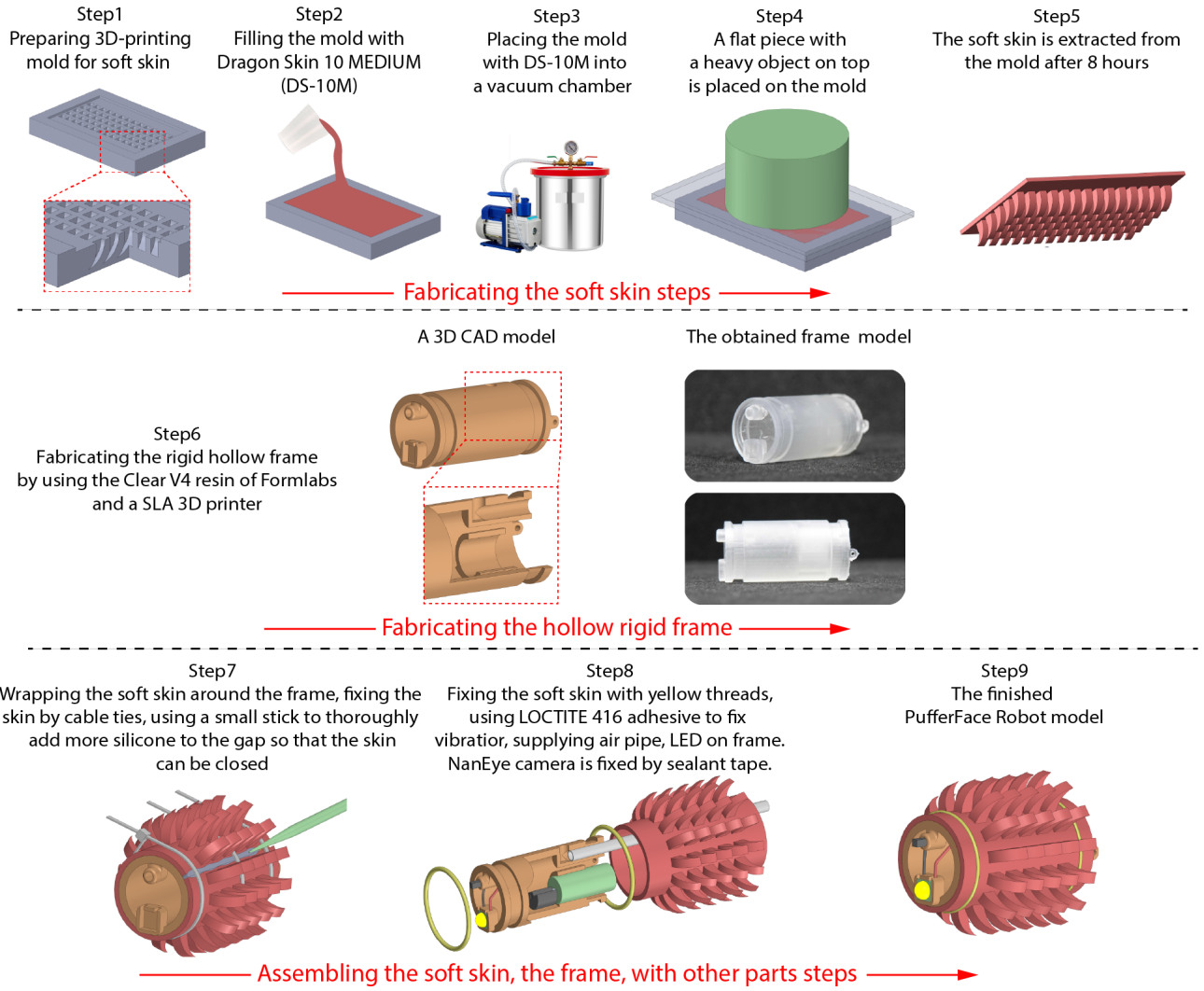


Figure 3.13: The fabrication process of PFR.

without any air bubbles inside the skin. This step is paramount because the existing air bubbles might cause the leakage of the compressed air, affecting the inflation and deflation phase of PFR. After allowing it to cure sufficiently at room temperature for 8 hours, the soft skin was extracted from the mold (Steps 4 and 5). We used an SLA 3D printer (Form3, Formlabs Inc) and clear resin to make a hollow-shaped rigid frame (Step 6). After wrapping the extracted soft skin around the printed hollow-shaped rigid frame and fixing it in place with cable ties, we use a stick to thoroughly add more silicone to the gap so that the skin can be closed (Step 7). The DC vibration motor, air pressure hose, and LED are attached to the rigid frame via adhesive (LOCTITE 416, Henkel Adhesives), while the camera is fixed with sealant tape (Step 8). In Step 9, the soft skin was attached to the peripheral notches of the hollow-shaped frame using threads.

## Chapter 4

# Study and Analyze the Involving Physics Phenomena of Vibration-based Soft Robot Designs

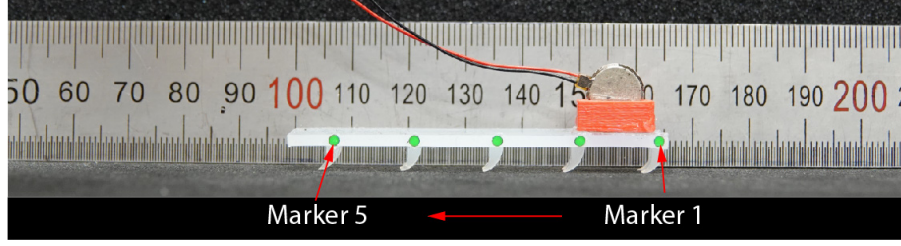
### 4.1 The involving physics phenomena on *Leafbot*

This section clarifies the underlying physics phenomena of Leafbot locomotion driven by a vibration source. To track the Leafbot’s high-frequency motion, we conducted preliminary observations to determine the necessary parameters for constructing the analytical model.

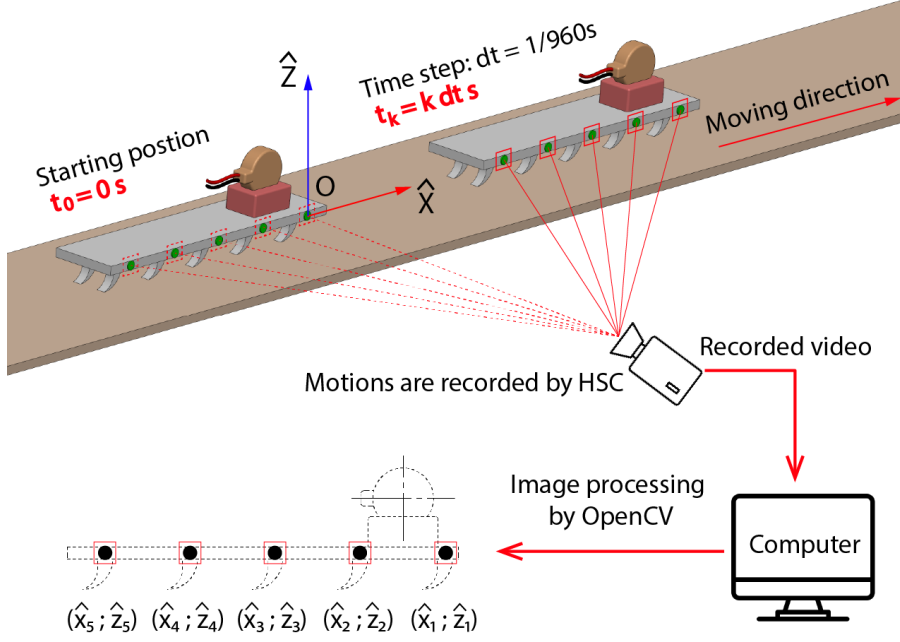
#### 4.1.1 Vibration frequency

We adopted a marker-based motion capture (or mocap) system with a high-speed camera (HSC) and reflective markers for motion analysis to address Leafbot’s high-frequency locomotion gaits. This technique is widely used to investigate locomotion behaviors, even in high-frequency conditions [93, 94]. Additionally, firms have developed advanced markers, such as infrared markers, for specialized optical tracking systems.

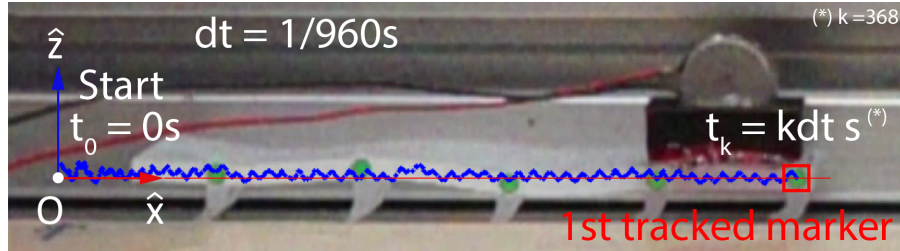
In our case, we presented a simple and low-cost method to conduct mocap experiments while still ensuring the necessary precision and accuracy. Our tracking model comprised an HSC and reflective markers adhered to specific points on the robot body to detect the motion over time (see Figure 4.1(a)). Based on the thickness,  $t$ , of the robot backbone, 2 mm-diameter circular markers were selected. Moreover, to keep the markers compact and lightweight, we cut them from green reflective tape using a laser-cutting machine. Our marker-based mocap experiment is illustrated in Figure 4.1(b). Selecting the HSC’s frame rate, fps (frame per second), is crucial and must be at least twice the highest frequency of the vibrating Leafbot to accurately capture its frequency bandwidth [95]. Leafbot’s locomotion is controlled by adjusting the vibrating frequency by varying the motor voltage, with a maximum supply voltage of 5 V to avoid damaging the motors. We measured the oscillation frequency at 5 V utilizing a piezoelectric disc (CUI Devices CEB-35D26) connected to a KEYSIGHT



(a) Green markers are attached to the robot body. The order of markers starts from the vibrator side to the tail side. Marker 1 starts at the first limb on the vibrator side, and marker 5 is the last marker placed at the last limb.



(b) The motion capture experiment set-up.  $\hat{x}_1$  and  $\hat{z}_1$  represent the experimental values of marker 1. The analogous definition is applied to other markers.



(c) The trajectory of the first marker from  $t_0$  to  $t_k$ .

Figure 4.1: Marker-based model for robot motion investigation. Markers' coordinates are then determined with respect to time. A time step ( $dt$ ) is equal to  $1/960$  (designed frame per second - fps of HSC). (a) Green markers on the robot backbone; (b) The experimental set-up; (c) Example of the first maker's trajectory.

InfiniiVision DSOX2002A oscilloscope [19]. This oscilloscope, with a sensitivity of  $10 \text{ mV/div}$  and a frequency bandwidth of up to  $10 \text{ MHz}$ , showed smooth sinusoidal curves of the voltage output from the piezoelectric disc (see Figure 4.2). The vibration frequency of the tested motors ranged from  $230 \text{ Hz}$  to  $260 \text{ Hz}$  at  $5 \text{ V}$ , with a recorded voltage amplitude of about  $8 \text{ V}$ . From

these preliminary evaluations, we chose the SONY DSCRX10M4 HSC, which featured 960 fps and satisfied the required sampling rate. Note that the oscillation frequency varied among different motors at the same voltage, making it crucial to determine the voltage-frequency characteristics.

Using mocap video from the HSC, we tracked the markers' trajectories (see Figure 4.1(c)). These reveal Leafbot's locomotion mechanism. The robot's front head jumps forward at certain frequencies, causing passive bounces along its backbone. We analyzed these trajectories using the Fast Fourier Transform (FFT) to identify dominant frequencies. We observed Leafbot3, Leafbot5, and Leafbot9 at 3V, 4V, and 5V and focused on the jumping frequency of the first marker. Figure 4.3 shows one of the obtained trajectories via the mocap method and the dominant frequency analysis by FFT at 3V. Table 4.1 presents oscillation frequencies from the piezoelectric disc and Fourier transform. We observed a drop in centripetal force frequency when the vibrator was integrated into Leafbot despite a consistent voltage supply. This phenomenon was clarified as it impacts the analytical model. We utilized an open-design eccentric mass vibrator to track its rotation speed on a piezo disc and the soft body. Figure 4.4 depicts our experimental set-up for clarification. There are two conclusions drawn from this inspection:

- We observed that, under the same applied voltage, the rotation speed of the eccentric mass decreases when the vibrator is transferred from the piezo disc to Leafbot's soft body. This speed is affected by the mass of the object on which the vibrator is placed. Here, elaborating on such a phenomenon is out of the scope of this paper.
- When the vibrator is integrated with the soft body, the vibration frequency (Hz) extracted from the marker on the soft body is equal to the angular frequency (rad/s) of the motor over  $2\pi$ .

From these early observations, we conclude that the angular frequency (rad/s) of the eccentric mass in the enclosed design of the vibrator can be inferred from the dominant freq. shown in Table 4.1. These results are the parameter input for the analytical model.

#### 4.1.2 Transverse waves along the soft backbone

Aside from oscillation at the vibrator location, another key phenomenon in Leafbot's locomotion is the transverse wave on its soft backbone, caused by the front head bouncing and creating motion along the backbone. We justified this observation by investigating the frequencies



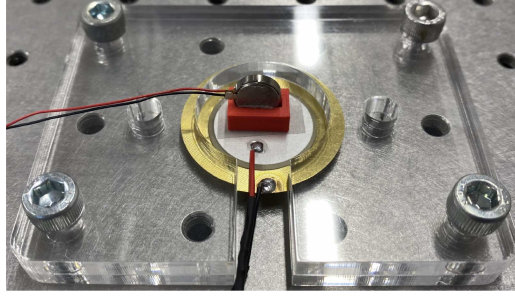


Figure 4.2: Employing piezoelectric disc to determine the vibration frequencies corresponding to the applied voltage on driven motors. The vibrator mounting to a 3D-printing housing is attached to the piezoelectric disc by a double-sided tape [19].

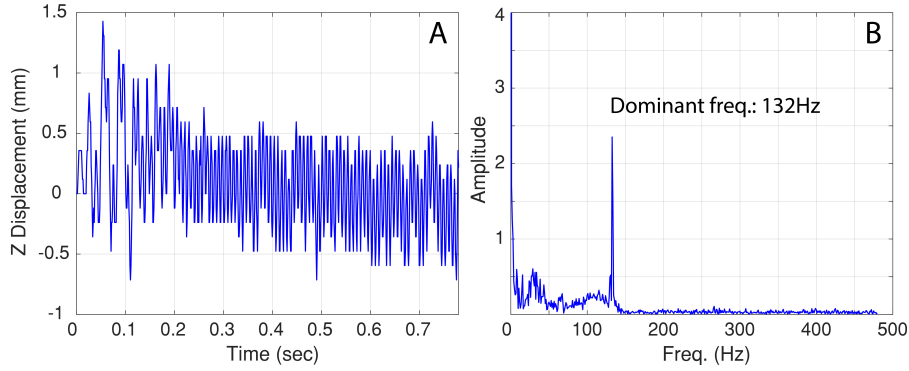


Figure 4.3: The obtained trajectory of the first marker of Leafbot5 by processing the captured image from HSC. (A) The displacement of the 1st marker in the  $Z$  direction,  $\hat{z}_1$ , at 3V. (B) The collected dominant freq. in freq. domain by FFT from experimental data of vector  $\hat{z}_1$  at 3V.

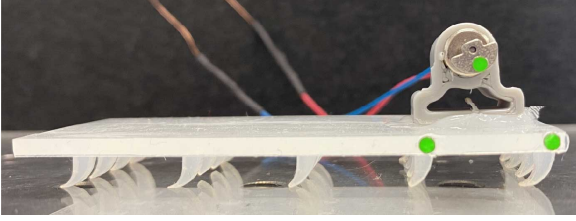
of other markers and the time difference,  $\tau$  (second), between nearby markers at maximum heights. Mocap data revealed consistent frequencies across Leafbot's body, except for Leaf3 at 4V (186Hz), where markers 2 and 3 stalled in the  $Z$  direction, accompanied by a rapid decrease in  $X$  direction velocity. The values of  $\tau$  can be calculated from the peaks of two adjacent markers in the  $Z$  direction (see Figure 4.5) and are used to specify the transverse forces in the analytical model.

## 4.2 The involving physics phenomena on *PFR*

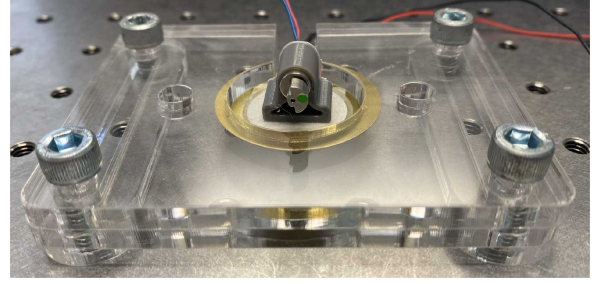
Unlike the Leafbot design, the PFR design is equipped with two actuation components, including the eccentric DC motor and the pressurized air inlet (see Figure 3.11). The combination of these two actuators is able to deliver three locomotion modes with three distinguishable postures. The first and second modes are activated by the vibration motor and the air inlet, respectively. The third one is generated via simultaneous activation of the vibration excitation and the air input. The physical features of the three modes are explained in the following

Table 4.1: The experimental values of oscillation frequency were determined from the piezoelectric disc and the mocap data processed by FFT at the applied voltage 3V, 4V, and 5V.

	Applied Voltage	3V	4V	5V
	Measured freq. by piezoelectric disc on the predetermined motor (Hz)	210	240	260
Leafbot3	Dominant freq. analyzed by FFT on $\hat{z}_1$ data (Hz)	132	186	191
Leafbot5		132	142	186
Leafbot9		120	166	170



(a) The open design of the vibrator was mounted on a soft body. The markers were adhered to the eccentric mass and the soft body to determine the rotational speed and the oscillation frequency of the soft body.



(b) The open design of the vibrator was attached to the piezoelectric disc by double-sided tape.

Figure 4.4: Clarifying the frequency decline phenomenon of the vibrator when it was incorporated into different objects.

sections.

## 4.2.1 Modes of locomotion

### 4.2.1.1 Mode 1: vibration only Mode

Vibration-based locomotion models have been developed to target applications for pipeline systems. Such proposed locomotion postures completely rely on the excitation frequencies of vibration sources, which are derived from a rotation of an eccentric mass [10, 12, 60] or stimulation of a piezoelectric actuator supplied with high voltages [9, 65–68]. Within this paper, we consider this locomotion strategy as Mode 1. The operational fundamental involves the stick and slip phenomenon, alternatively known as the asymmetric friction force. When the eccentric mass rotates, it generates a centripetal force vector periodically in the plane perpendicular to the motion direction. Thus, the entire robot body is subjected to a sinusoidal centripetal force. As a consequence, the elastic limbs run into the compression and the release period cyclically. The stick phase corresponds to compression, while the slip phase corresponds to release. The

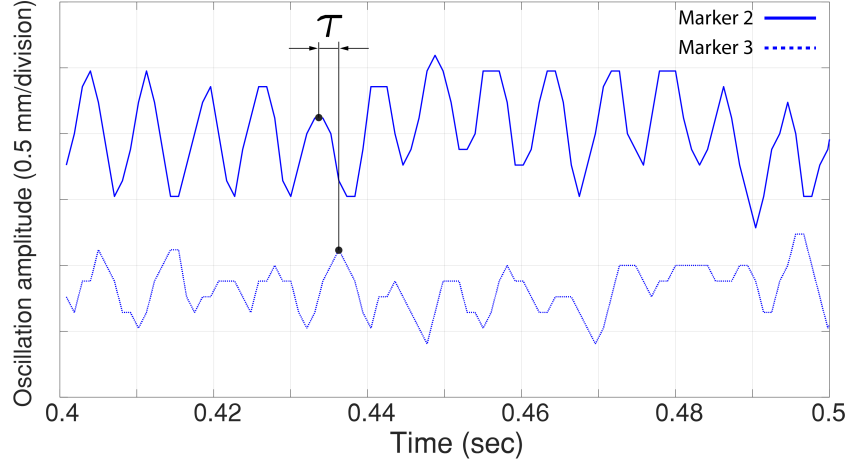


Figure 4.5: The determination of the time difference between two nearby peaks (marker 2 and marker 3) of a transverse wave,  $\tau$ , in the case of Leaf5 at 3V (132Hz).

working principle of Mode 1 of the locomotion is presented in Figure 4.6C. The limitation of Mode 1 is that it cannot provide locomotion against gravity in tubular conditions where the inner diameter exceeds the outer diameter ( $OD_S$ ) of the PFR, see Figure 4.6A.

#### 4.2.1.2 Mode 2: variation of pressurization only mode

In this mode, the propulsion motion of PFR solely happens due to the sequential inflation and deflation of the robot. In contrast to Mode 1 and Mode 3, the delivered velocity of this mode is very slow due to the activation method (sequentially inflating and deflating the soft skin), which is able to yield only a small amount of net displacement,  $D_2$ , after a complete cycle of inflation to deflation process (see Figure 4.6C, Mode 2). During the inflation, the soft skin and the spikes are compressed (the stick phase occurs). When PFR rapidly deflates, the slip mechanism happens, generating a net displacement in one cycle of applying pressure. We characterized the deflation rate by an average pressure decline in one second and represented it by the  $Df_r^a$  parameter. In Mode 2, to obtain a net displacement, we reported that  $Df_r^a$  should vary from 10 to 15 kPa/s. The average velocity in this mode is approximately 0.5 mm/s. However, the most significant advantage of Mode 2 is the ability to create substantial propelled forces (see Figure 4.11) that outperform the rest of the locomotion modes. The maximum generated propulsion forces are even 20 to 35 times higher than the total weight of PFR (see the Propulsion force examination for more information). This propelled force is produced as a result of the soaring up of the inlet pressure in the inflation process. The pressurized air compresses the soft skin and spike pattern against the pipe wall, increasing the normal force on

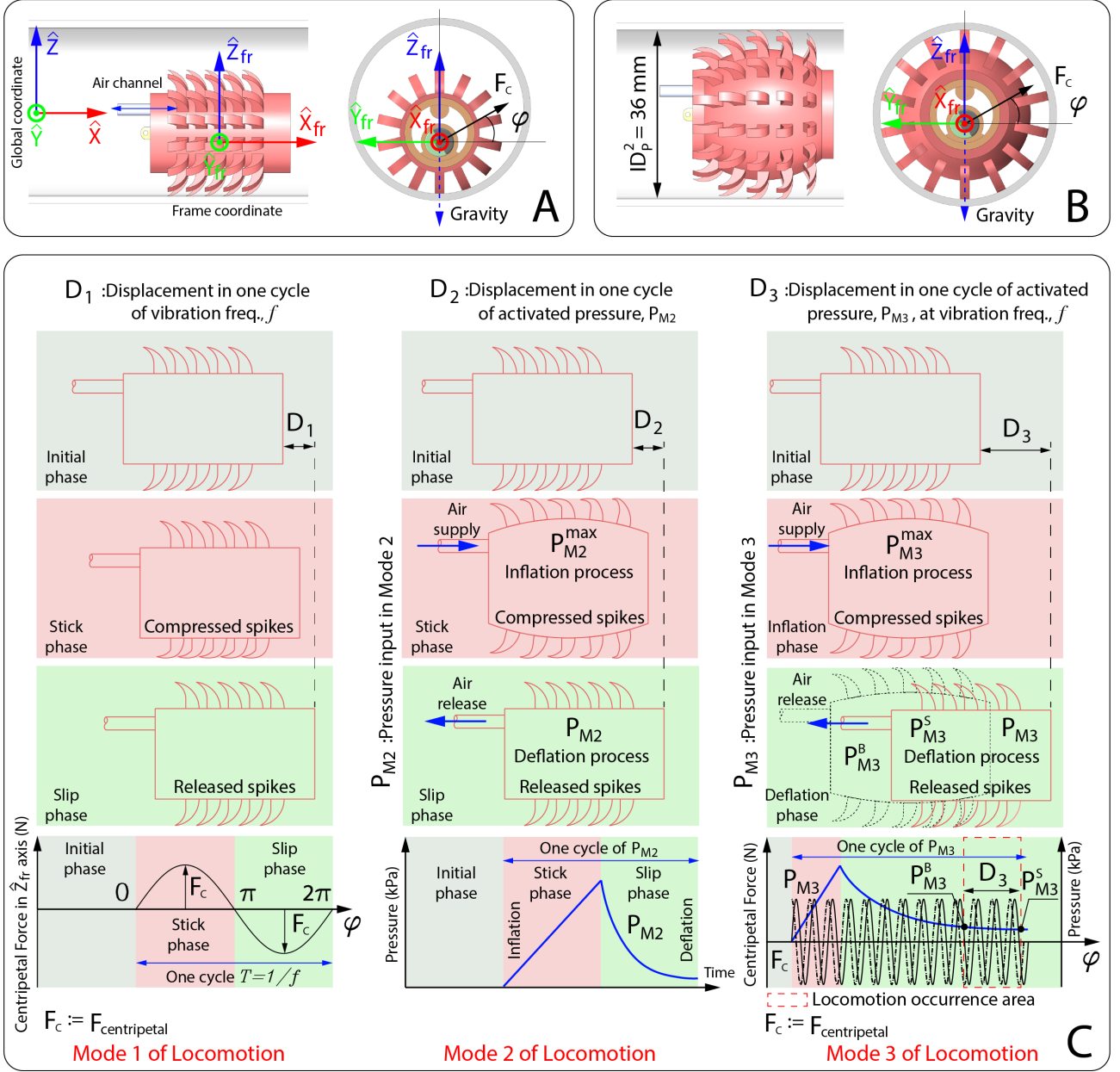


Figure 4.6: Operation principle and locomotion modes of PFR. (A) the PFR is in the tubular condition whose inner diameter exceeds the PFR's outer diameter. The PFR is in a normal state. A vector of centripetal force,  $F_c$ , is generated by the DC vibrator and relies on its rotation angle,  $\varphi$ . (B) The PFR is transformed from the normal state into the inflation state via the supplying air channel and adapts to a bigger-diameter condition of the cavity environment. (C) Modes of locomotion explanation. Mode 3 is a combination of the vibration and inflation/deflation process. In the subset figure of Mode 3, the dash-dot line and the solid line, which are out of phase by  $\pi/2$ , stand for the centripetal force vector components in the plane containing  $\hat{y}_{fr}$  axis and  $\hat{z}_{fr}$  axis.

the spikes and causing deformation. The spikes' morphology transforms this normal force into a forward-propelling horizontal force (See the stick phase in Mode 2). Consequently, Mode 2 of motion creates a solid pulling force when every limb is subjected to being highly deformed.

Hence, we capitalized on this feature in particular contexts, such as approaching target points for inspection tasks with a built-in camera, overcoming complex regions, or regions with highly resistant force.

#### 4.2.1.3 Mode 3: vibration and pressurization change mode

Mode 3 is the combination of Mode 1 and Mode 2. It is primarily utilized to manipulate PFR in cavity environments. Because we aim to develop an adaptable soft robot, PFR has to transform its outer soft skin flexibly and rapidly to adapt to varying working environments. Therefore, when encountering pipes that are bigger than PFR's outer diameter, PFR activates the air channel to expand the soft skin and anchor its soft spikes to the pipe wall. At the same time, the vibration from the eccentric mass is initiated and maintained consistently, leading to the appearance of the centripetal force (see Figure 4.6C, Mode 3). PFR obtains the forward motion in the deflation phase (the light green area) (see Mode 3 of Locomotion in Figure 4.6). Considering the deflation phase, which primarily generates forward locomotion for PFR, when the pressurized air reaches a specific pressure point,  $P_{M3}^B$ , PFR behaves roughly similarly to Mode 1 and Mode 2, where the built-in vibrator yields sinusoidal centripetal force,  $\mathbf{F}_C$ , acting on the entire soft body and the soft spikes. The stick-slip phenomenon is induced periodically, yielding a displacement,  $D_3$ , over one cycle of activated input pressure. The forward motion continues until the pressure drops below a certain threshold,  $P_{M3}^S$ , where it can no longer sustain the inflation radius required for the soft spikes to maintain contact with the tubular wall. As a result, the stick-slip mechanism ceases, and no further motion occurs until the next deflation cycle begins. Note that  $D_3$  is substantially bigger than  $D_2$ , although they both obtain a displacement after a single cycle of activated input pressure. Nevertheless, in Mode 2, PFR only undergoes one cycle of stick and slip, whereas, in Mode 3, the number of times the stick and slip occur corresponds to the vibration frequency. Therefore, the average velocity of Mode 3 far outweighs Mode 2. The reduction slope of the pressurized air is regulated via a flow control valve of SMC, model AS2052F. Similarly to Mode 2, the pressure curve during deflating is characterized by the average deflation speed, kPa/s, and defined by the  $Df_r^a$  parameter. The pressure drop might behave non-linearly depending on the pipe size. We determined the threshold of  $Df_r^a$  should be 6 kPa/s. If the pressure falls faster than 6 kPa/s, the displacement will be significantly reduced, or even the PFR will stand still in the worst scenario.

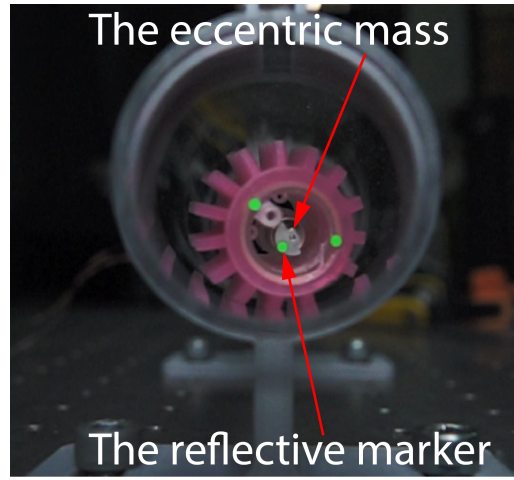
### 4.2.2 Vibration frequency

The locomotion of PFR can be activated by two input parameters, including the vibration frequency and the pressurized air. We categorized three Modes of locomotion based on these two inputs. The vibration frequency determines the influence of the centripetal force on the entire body of PFR. The frequency and the amplitude of vector  $\mathbf{F}_C$  rely on the rotation speed of the eccentric mass. As depicted in Figure 4.6A and Figure 4.6B, a frame of reference,  $\hat{X}_{fr}\hat{Y}_{fr}\hat{Z}_{fr}$ , is attached to the hollow frame on which the vibrator is mounted. When the eccentric mass rotates, the hollow-shaped frame is subjected to the centripetal force,  $\mathbf{F}_C$ , which rotates in the plane containing  $\hat{Y}_{fr}$  axis and  $\hat{Z}_{fr}$  axis. Note that the centripetal force vector direction should point toward the rotation center; however, we offset the vector's tail to the rotation center to demonstrate its influence on the rigid frame (a reaction force vector of the centripetal force). The following function determines the vector of the centripetal force:

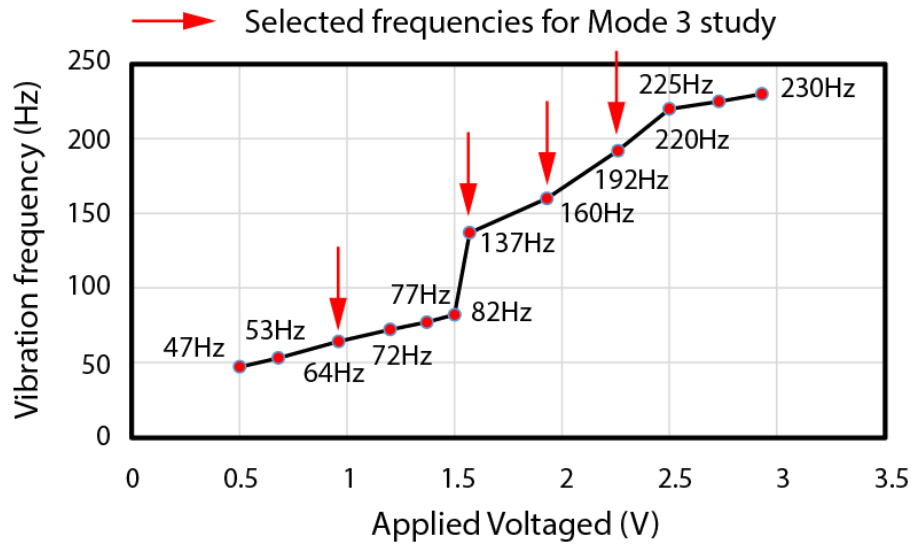
$$\mathbf{F}_C = m_e \omega_v^2 [r_e \cos(\omega_v t) \hat{\mathbf{y}}_{fr} + r_e \sin(\omega_v t) \hat{\mathbf{z}}_{fr}] + m_e \mathbf{g}, \quad (4.1)$$

In the given context,  $m_e$ ,  $r_e$ ,  $\omega_v$ , and  $\mathbf{g}$  stand for the eccentric mass, the radius from the eccentric mass to the center of rotation, the angular frequency of the rotation (rad/s), and the gravitational vector, respectively.  $\hat{\mathbf{y}}_{fr}$  and  $\hat{\mathbf{z}}_{fr}$  denote unit vectors along the  $\hat{Y}_{fr}$  and  $\hat{Z}_{fr}$  axis (see Figure 4.6A, B). We utilized a high-precision electronic scale (resolution: 0.001 gram) and an optical microscope to determine  $m_e$  and  $r_e$ . The values of  $m_e$ ,  $r_e$  are 0.572 grams and 1.72 mm.

To figure out the angular frequency  $\omega_v$  of the centripetal force, we employed a high-speed camera, SONY DSCRX10M4 model featuring 960 frames per second (fps), to capture the marker's rotation attached to the eccentric mass. The experimental setup to collect time-position data of the eccentric mass for the centripetal force is presented in Figure 4.7(a). The motion capture video was processed by the OpenCV package, and then the time-position data was extracted in the CSV format. Subsequently, this data was analyzed by the Fast Fourier Transform (FFT) to determine the dominant frequency (Hz) in the frequency domain. These dominant frequencies represent the vibration frequency (Hz) of the centripetal force corresponding to the applied voltage (V). Consequently, we can determine the relation between the vibration frequency (Hz) induced by the centripetal force and the applied voltage (V) to the DC motor. The angular frequency (rad/s) is equal to  $2\pi$  times the vibration frequency



(a) The experimental setup to measure the vibration frequency (Hz) of the eccentric mass.



(b) The relation between the applied voltage (V) and the vibration frequency (Hz).

Figure 4.7: The experiment to determine the relation between the applied voltage (V) and the vibration frequency (Hz) and its obtained results.

(Hz). The relationship between the supplied voltage and the vibration frequency (Hz) was then identified and exhibited in Figure 4.7(b).

In addition, the selection of the high-speed camera, featuring a 960-Hz sampling frequency, to determine the vibration frequencies was justified. We measured the maximum vibration frequency of the vibrator at 3V by using a piezoelectric disc (CUI Devices CEB-35D26) connected to a KEYSIGHT InfiniiVision DSOX2002A oscilloscope to determine the highest vibration frequency corresponding to the maximum applied voltage, 3V. This experiment was conducted and presented in Figure 4.4(b). The frequency of the voltage signal collected from the piezoelectric disc was approximately 235 Hz. Based on the Shannon theorem, which requires

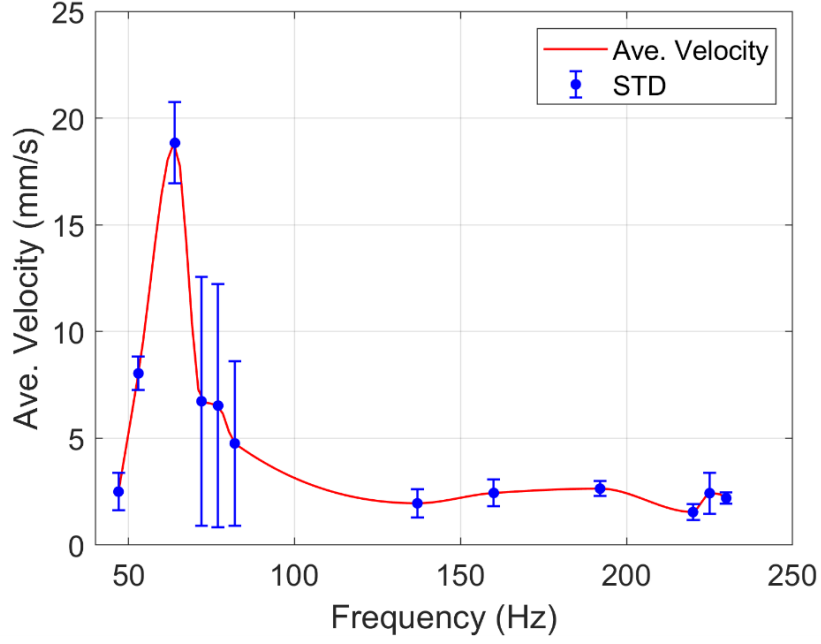


Figure 4.8: The obtained average velocity of PFR with respect to vibration frequency in Mode 1 of locomotion.

that the sampling rate must be at least twice the highest frequency of the experimental vibration frequency to capture its frequency bandwidth accurately [95], the selection of the high-speed camera in this experiment was validated.

The motor's angular frequency is proportional to the applied voltage. We utilized the 8-bit PWM output of Arduino UNO together with the LN298 driver to regulate the voltage supplied to the DC vibrator (see Figure 4.10). Besides, the LN298 driver allows us to change the rotation direction of the DC motor.

Next step, to experimentally investigate the influence of the sole vibration frequency on the PFR's locomotion, as presented in Mode 1 in Figure 4.6C, the entire body of PFR is subjected to the excitation of the centripetal force,  $\mathbf{F}_C$ , resulting in a displacement,  $D_1$  after every cycle of  $\mathbf{F}_C$ . Thus, it's imperative to elucidate the correlation between motion velocity and frequency originating from the vibration source. Figure 4.8 depicts the relationship between vibration frequency and average velocity in Mode 1 of locomotion. Mode 1 strategy is merely activated when PFR horizontally traverses in tubular conditions where the inner diameters are equal to the outer diameter of PFR,  $OD_S$ .



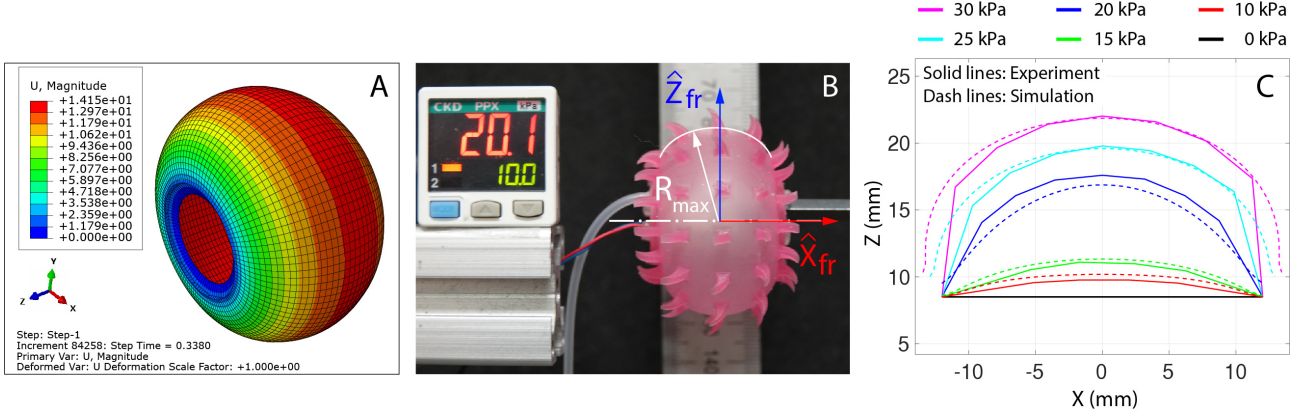


Figure 4.9: The relation between the applied pressures and the obtained expansion radii of soft skin. (A) Employing a hyperelastic simulation module of ABAQUS to identify the radius behavior corresponding to the applied pressure. The simulation can be utilized to determine arbitrary radii corresponding to desired tubular working conditions. (B) Identifying the expansion radius by capturing the inflation state. (C) The outcomes of the empirical and simulated methods were obtained.

### 4.2.3 Characterization of the inflation radius

Figure 4.6B and Figure 4.6C present the adapting and conformable mechanism of PFR's body when dealing with variable cavities. The determination of necessary pressure values to inflate PFR to reasonable radii fitting with the tubular sizes cannot be neglected. The soft skin is fabricated by the Dragon Skin 10 silicone rubber. This specification allows PFR to expand up to two and a half fold the outer diameter of PFR at the normal state. The PFR's soft skin can efficiently perform large deformations thanks to the hyperelastic characteristic of the fabricated material. To figure out the correlation between the input pressure and the expansion shape of the soft skin, we adopted the hyperelastic simulation function from ABAQUS software to handle this task, and the Yeoh model was of interest because, based on the working conditions aiming to, the maximum strain might reach up to 200%, where the Yeoh model provides the best-fit [91]. To work with the Yeoh model, three coefficients are required for the simulation model. These three material constants are referred from [91], *i.e.*,  $C_1 = 36$  kPa,  $C_2 = 0.25$  kPa, and  $C_3 = 0.023$  kPa. We then justified the simulation results with the experiment by capturing PFR states corresponding to the applied pressures. Then, we processed them with image processing software. After the empirical verification, the outcomes of the simulation will be employed to determine the needed pressure values for PFR when it encounters arbitrary boundary conditions. The expansion curves of PFR (experiment and simulation) when it is subjected to the inlet pressure are demonstrated in Figure 4.9. Note that we did not include

the soft spikes in the simulation model to reduce the calculating time. Yet, the simulation still illustrates reliable outcomes in five cases of applied pressure. These expansion performances suggest that PFR can cope with cavities that are two times bigger than PFR's body; however, it was reported that at 30kPa, there were small shaded white regions appearing on the stretched skin surface; consequently, within this design concept, we merely aim to test PFR at the  $1.5 \times OD_S$  state.

#### 4.2.4 Propulsion force examination

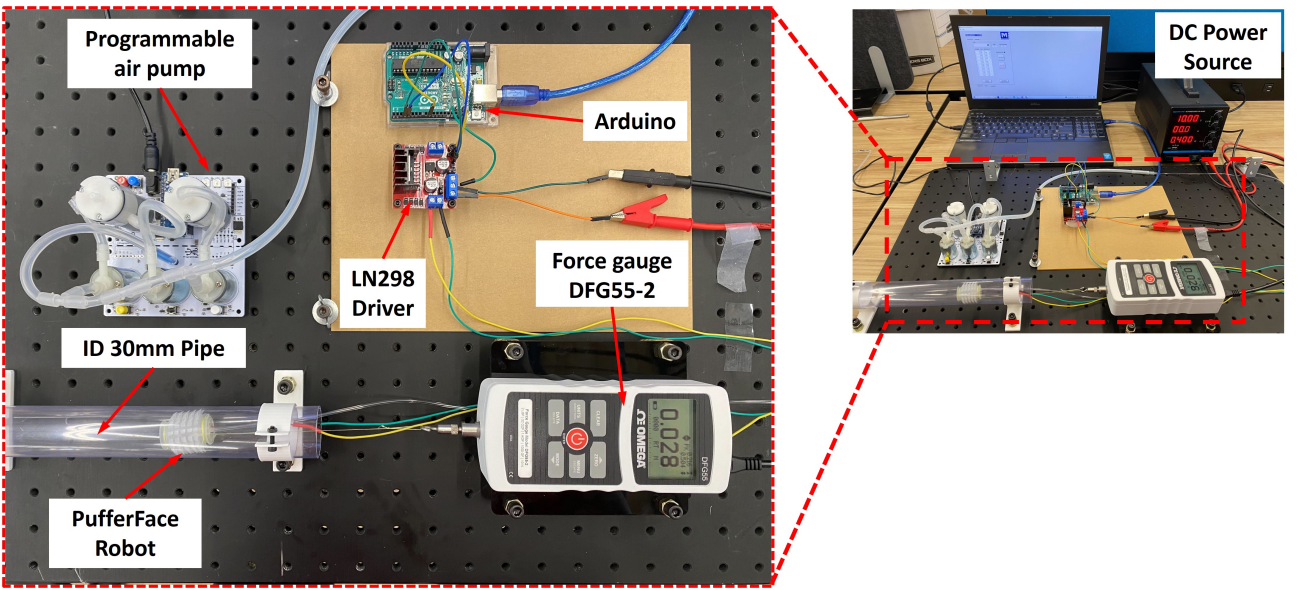


Figure 4.10: The experimental scheme to measure the propulsion force generated from the soft spike pattern.

From the very beginning, we set our goal to develop an inflatable version of PFR so that it can adapt and locomote in tubular conditions, which have diameter dimensions vary from  $1 \times OD_S$  to  $1.5 \times OD_S$  ( $OD_S$  *i.e.*, the outer diameter of the robot). Based on these boundary conditions, we examined the locomotion performances in straight and plain pipes of three inner diameter dimensions, *i.e.*,  $ID_P^1=30$  mm,  $ID_P^2=36$  mm, and  $ID_P^3=41$  mm. The purpose of these experiments was to measure the propulsion force of the proposed novel concept robot within pipes of various sizes. An overview of the experimental scheme is shown in Figure 4.10. Power was supplied to the vibrator motor through the DC power supply, and the vibration frequency of the motor was controlled via a microcontroller (Arduino Uno, Arduino) and a motor driver (L298N Motor Drive Controller). The inflation and deflation of the soft robot are controlled through the pneumatic actuation system (Programmable Air, Crowd Supply). The system

consists of two air pumps, three solenoid valves, and an air pressure sensor. With this setup, the air pressure inside the soft robot is actively controlled using the pressure sensor. The propulsion force was measured by connecting the robot and the force gauge (DFG55, OMEGA) with a tendon. In this scenario, we measured the propelled force generated from the soft spike pattern by activating Mode 3 of the locomotion of PFR. The examination was conducted in three different pipe sizes, as mentioned above. The motor's vibration frequencies are set to 64 Hz, 137 Hz, 160 Hz, and 192 Hz, while the air pressure inside the soft robot is set to 20 kPa, 23 kPa, and 26 kPa. The selection of pressure values is based on the assessment of the inflation radius and the supplying pressure so that PFR can expand to have enough contact with the pipe wall. The experiment was performed for a total of 36 cases, considering the combination of the four different motor vibration frequencies, three air pressure levels, and three pipe inner diameters. The states of PFR when it is supplied with air from the pump are presented in Figure 4.12.

Figure 4.11 exhibits 36 cases of the generated thrust force along with the inflation/deflation states of PFR. Generally, the force graph at any given vibration frequency and applied pressure always illustrates two patterns. The smooth curves are at the inflation phase, and the noisy curves are at the end of the deflation phase of the input pressure. As presented in Figure 4.6, at the inflation phase, the soft body expands and contacts the cavity wall, yielding deformations on the morphological limb pattern of PFR and leading to boosting the force. The elastic deformations from the spikes primarily account for the soaring up of the force at this step. The maximum acquiring values are from 20 to 35 times the total weight of PFR (10 grams). Looking at Figure 4.12 and Figure 4.11, it is observed that the value of the peaks of the obtained force corresponds to the number of the contacting limbs. In the 30-mm tube, four rows of PFR legs are compressed under all testing values of pressure, whereas there are only two to three rows of limbs that are deformed in the 36-mm and 41-mm experiments, causing a slight drop of the highest induced force. However, with this capability of generating force, it suggests that PFR can easily interlock its body in vertical working conditions by inflating the soft skin to serve particular inspection purposes. When PFR experiences the deflation phase, its soft body begins shrinking gradually, corresponding to the release rate of the pressure, leading to decreases in the forces; accordingly, the force curves become noisy due to the influences of the vibration excitation frequencies. The noise patterns vary according to frequencies. In the 30-mm pipe, the noises appear nearly at the end of the deflation phase, and they are formed by the stick-slip

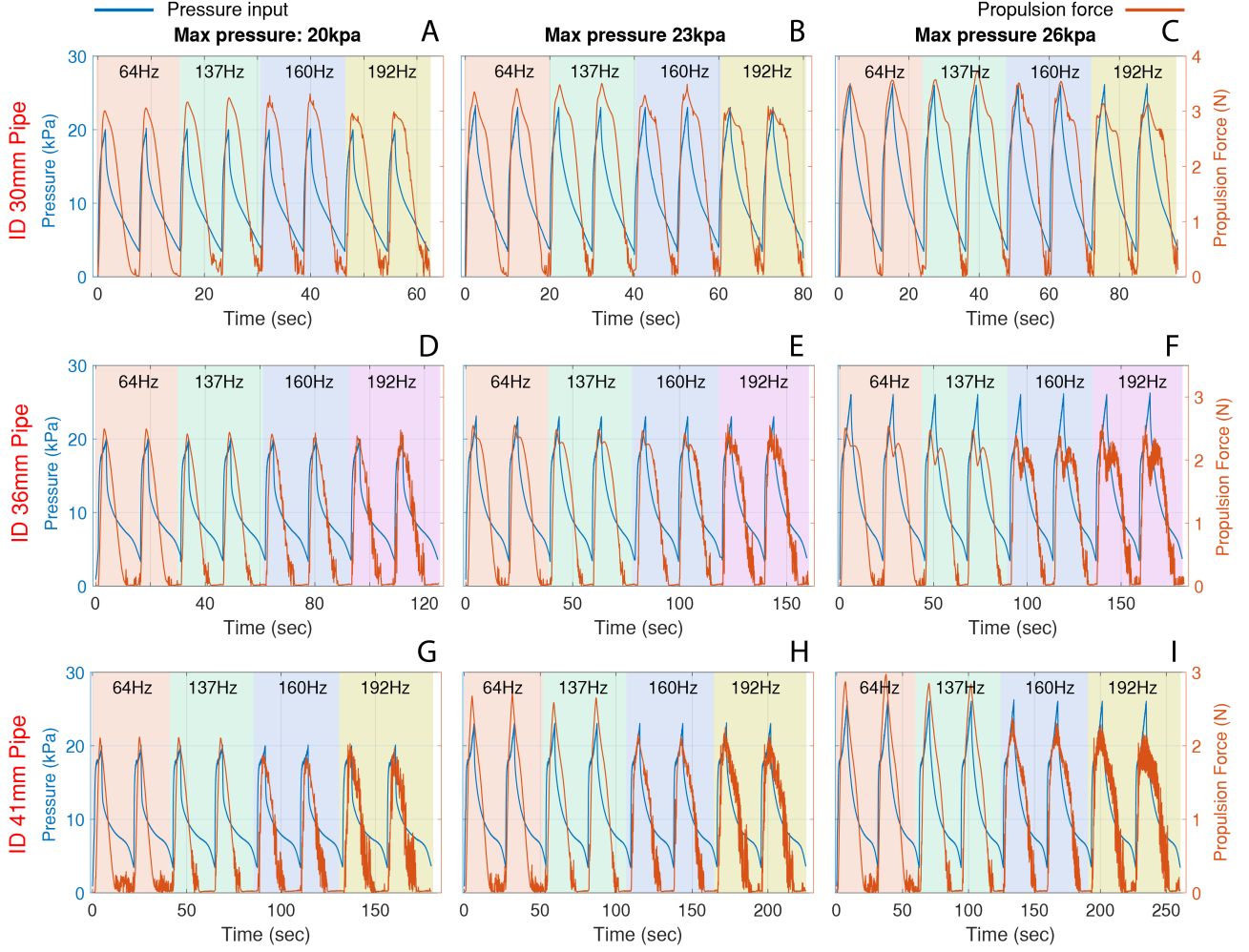


Figure 4.11: Obtained propulsion forces conducted in the  $ID_P^1=30$  mm,  $ID_P^2=36$  mm, and  $ID_P^3=41$  mm pipes in the aforementioned pre-setting conditions. (A, D, G), (B, E, H), and (C, F, I) demonstrate the results in the cases of applying pressures 20 kPa, 23 kPa, and 26 kPa, respectively.

mechanism, which is explained in Figure 4.6.

The locomotion was also reported to occur at this deflation area. The forward movement begins when the pressure falls to a specific level,  $P_{M3}^B$ . The pressure continues to decrease until it reaches another threshold,  $P_{M3}^S$ , at which the inflation of the soft skin is not sufficient to maintain contact with the pipe wall, causing the locomotion to stop in a single pressure cycle (see Mode 3 of locomotion explanation in Figure 4.6). When the pipe diameters are larger than ODS, the 36-mm and 41-mm ones, it was observed the more the DC motor vibrates, the earlier and the noisier the force curves behave. This indicates that in these contexts, PFR might obtain higher displacements. In addition, it is noticed in Figure 4.11 that in the 30 mm pipe, there are no significant differences between the response at 23 kPa and 26 kPa. Analogous observations can be figured out in the 36-mm and the 41-mm cases. The interaction states



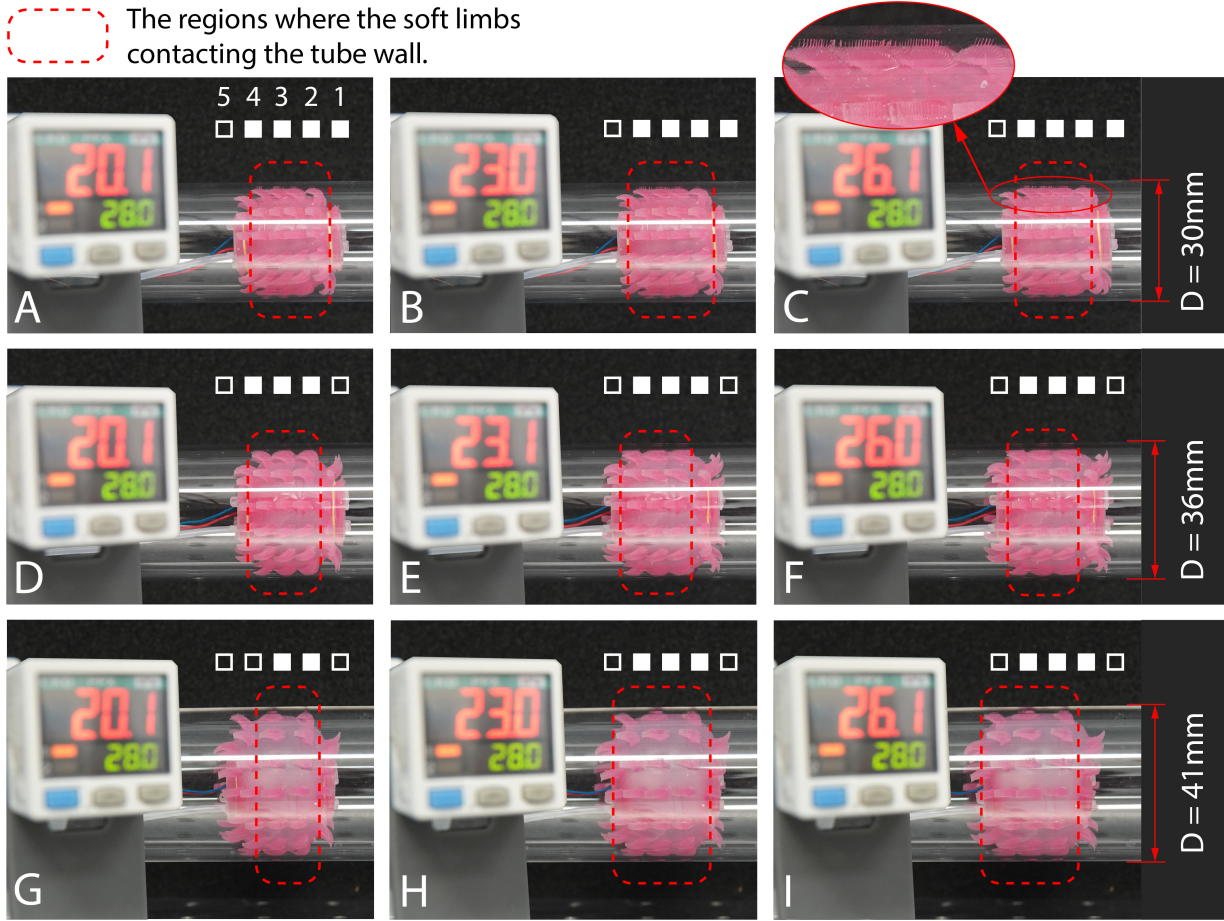


Figure 4.12: The shapes of the soft skin when subjected to three pressure air values in three tube dimensions. (A, B, C), (D, E, F), and (G, H, I) are cases in which PFR is tested in 30-mm, 36-mm, and 41-mm tubes, respectively. The inset figure in (C) illustrates the traces of the contacting soft limbs with the wall. The white infill squares stand for the contacting spikes, whereas the sole-solid-line squares represent the non-contacting spikes. Each row of soft spikes in the radial direction is numbered from one to five from right to left. Each white square stands for 14 radially distributed soft spikes.

of PFR can explain this behavior (see Figure 4.12), as the number of soft spikes deformed during inflation remains consistent between 23 kPa and 26 kPa. From these force curves and the deformed conditions of PFR's limbs in pipes at 23 kPa and 26 kPa, it can be advocated that the generated displacement could be similar between 23 kPa and 26 kPa.

## Chapter 5

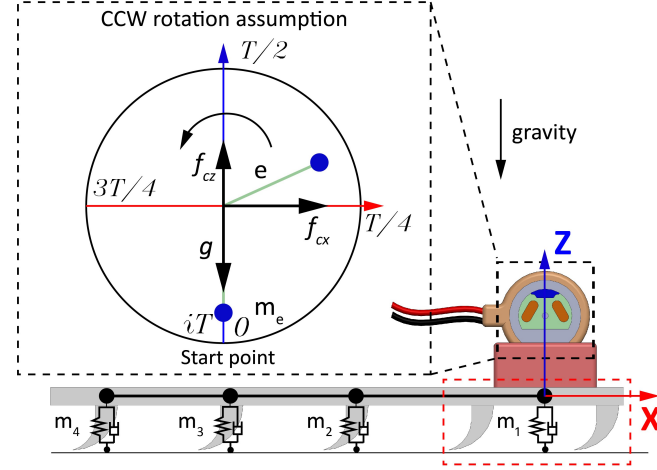
# Showcase of Vibration-driven Design in Planar Conditions: *Leafbot*

### 5.1 Constructing analytical model of *Leafbot*

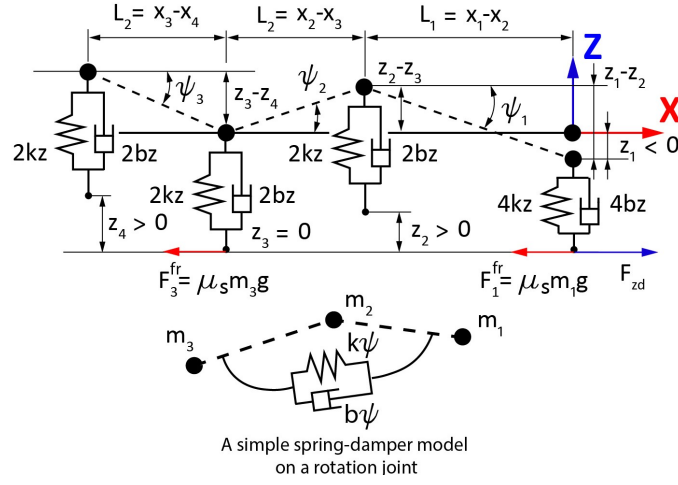
As presented in Section 3.1, the vibrator is the main source of actuation that allows the robot to move forward. The applied voltage to this vibrator can vary from 3 V to 5 V, which consumes a current of 67 mA to 110 mA, respectively. The equations to determine the centripetal force are shown in 3.1 and 3.2. In order to specify the values of eccentric mass:  $m_e$  and the effective radius from the eccentric mass to the center of rotation:  $e$ , we opened a vibrator and disassembled all inner parts. We employed an optical microscope and a high-precision electronic scale (resolution: 0.001 gr) to determine  $e$  and  $m_e$ . These parameters are illustrated in the Appendix B.

Next, we present our analytical model for the locomotion posture of Leafbot that enables us to generalize to three design patterns, *i.e.* Leafbot3, Leafbot5, and Leafbot9. Moreover, the model explains the observed physical phenomena of our proposed vibration-based soft robot. Note that Leafbot5 is the standard version, whereas Leafbot3 and Leafbot9 are additionally developed versions to compare with Leafbot5 in terms of dynamics performance and terra-dynamics study for this design concept. We first focus on Leafbot5, as our dynamics model can be generalized and applied to Leafbot3 and Leafbot9 configurations.

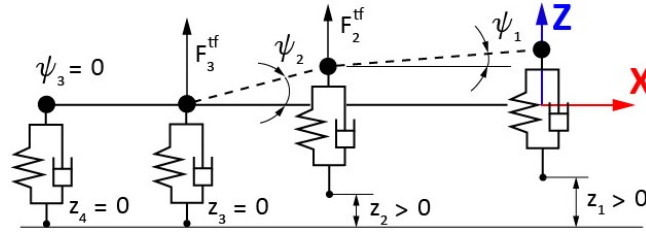
Figure 5.1 illustrates the dynamics scheme of our model. The vibrator is modeled as a source of centripetal forces,  $f_{cx}$  and  $f_{cz}$ , characterized by Eqs. (3.1), (3.2). It is then transformed into a simplified model as presented in the dash-line square in Figure 5.1(a), depicting how the centripetal force is generated within the vibrator. The blue circle represents the eccentric mass. The centripetal force generated by the rotating mass varies with the rotation angle, affecting  $f_{cx}$  and  $f_{cz}$ . We assume that the blue-circular mass starts rotating from the lowest point, named the *Start point*, in a counter-clockwise (CCW) direction.



(a) The simplified model of the vibrator.



(b) The line-segment model.



(c) The explanation for how transverse forces are generated.

Figure 5.1: The proposed dynamics scheme for the robot design. (a) The simplified model of the vibrator. All limbs in the red dashed line region are merged into a single node, attaching to an equivalent spring and damper. (b) The soft and monolithic structure of the robot body is transformed into the line-segment model and characterized by the viscoelastic model. These models characterize Leafbot's analytical model. (c) The transverse forces are induced by the transverse wave generated by the vibration source.

Subsequently, we transform the soft backbone into the line-segment model and characterize it by the viscoelastic model [96] (see Figure 5.1(b)). The robot backbone of Leafbot5 is divided into four nodes (Leafbot3 has three, and Leafbot9 has seven), placed according to the limb

location. Each node represents a particular mass and connects to the nearby nodes by a solid black line. For Leafbot5 and Leafbot9, the limbs in the vibrator placement area (see the red dashed line in Figure 5.1(a)) are merged into a single node,  $m_1$ , connecting to an equivalent spring and damper. The first node,  $m_1$ , has the biggest value because it includes the mass of the vibrator and its housing, while  $m_2$  to  $m_4$  are equal. Recorded HSC videos show that these nodes exhibit jumping gaits during forward motion. Under the excitation from the driven vibrator, the first node ( $m_1$ ) jumps forward, causing the subsequent nodes to experience displacements,  $\delta z_i = z_{i+1} - z_i$ , which generate potential energy. The displacement vectors and the corresponding deviation angle between two consecutive nodes can be determined:

$$\begin{bmatrix} \delta x_i \\ \delta z_i \end{bmatrix} = \begin{bmatrix} x_{i+1} \\ z_{i+1} \end{bmatrix} - \begin{bmatrix} x_i \\ z_i \end{bmatrix} \quad (i = 1, 2, \dots, n-1). \quad (5.1)$$

$$\psi_i = \arctan \frac{\delta z_i}{\delta x_i} \quad (i = 1, 2, \dots, n-1). \quad (5.2)$$

The global coordinate is selected at the first node,  $m_1$ , at  $t_0 = 0$  and fixed during the locomotion occurrence (see Figure 5.1). The generalized coordinates are selected as  $\mathbf{x} := [x_1 \ x_2 \ \dots \ x_n]^T \in \mathbb{R}^n$  and  $\mathbf{z} := [z_1 \ z_2 \ \dots \ z_n]^T \in \mathbb{R}^n$ . The value of  $n$  varies with Leafbot's designs:  $n = 3, 4$ , and  $7$  for Leafbot3, Leafbot5, and Leafbot9, respectively.

The kinetic energy of the whole body can be formulated as below:

$$T = \frac{1}{2} \dot{\mathbf{x}}^T \mathbf{M} \dot{\mathbf{x}} + \frac{1}{2} \dot{\mathbf{z}}^T \mathbf{M} \dot{\mathbf{z}}, \quad (5.3)$$

in which  $\dot{\mathbf{x}} = \mathbf{v}_x := [\dot{x}_1 \ \dot{x}_2 \ \dots \ \dot{x}_n]^T \in \mathbb{R}^n$ ,  $\dot{\mathbf{z}} = \mathbf{v}_z := [\dot{z}_1 \ \dot{z}_2 \ \dots \ \dot{z}_n]^T \in \mathbb{R}^n$ , and  $\mathbf{M} := \text{diag}(m_1, m_2, \dots, m_n) \in \mathbb{R}^{n \times n}$ .

Under the excitation of the vibrator, the backbone of the mini robot is bent to a particular angle, leading to generating the potential energy,  $U_b$ . The backbone damping,  $b_\psi$ , is not considered because the influence on Leafbot's dynamics in the  $Z$  direction is not critical; thus,  $U_b$  is only formulated by  $k_\psi$ :

$$U_b = \sum_{i=1}^{n-1} \frac{1}{2} k_\psi \psi_i^2. \quad (5.4)$$

At a specific time-step that  $z_i < 0$ , node  $m_i$  experiences a deformation, resulting in inducing potential energy,  $U_d$ , which is formulated as follows:



$$U_d = \begin{cases} \sum_{i=1}^n \frac{1}{2} k_z z_i^2 & z_i < 0 \\ 0 & z_i \geq 0 \end{cases} \quad (i = 1, 2, \dots, n) . \quad (5.5)$$

The potential energy caused by gravity on every node,  $m_i$ , is only applied when  $z_i > 0$ :

$$U_g = \begin{cases} \sum_{i=1}^n m_i g z_i & z_i > 0 \\ 0 & z_i \leq 0 \end{cases} \quad (i = 1, 2, \dots, n) . \quad (5.6)$$

Applying the geometric constraint to ensure the length between consecutive nodes is equal to  $L_i$ :

$$R_i \triangleq \sqrt{\delta x_i^2 + \delta z_i^2} - L_i. \quad (5.7)$$

Lagrangian is obtained together with geometric constraints as follows:

$$\mathcal{L} = T - U_b - U_d - U_g + \sum_{i=1}^{n-1} \lambda_i R_i. \quad (5.8)$$

Lagrange's equations of motion are then derived as below:

$$\frac{d}{dt} \left( \frac{\partial \mathcal{L}}{\partial \dot{x}_i} \right) - \frac{\partial \mathcal{L}}{\partial x_i} = Q_{x_i} \quad (i = 1, 2, \dots, n), \quad (5.9)$$

$$\frac{d}{dt} \left( \frac{\partial \mathcal{L}}{\partial \dot{z}_i} \right) - \frac{\partial \mathcal{L}}{\partial z_i} = Q_{z_i} \quad (i = 1, 2, \dots, n). \quad (5.10)$$

where  $Q_{x_i}$  and  $Q_{z_i}$  are generalized forces, including dissipative forces (viscous forces). When  $i = 1$ ,  $Q_{x_i}$  and  $Q_{z_i}$  would include centripetal forces calculated in Eq. 3.1 and Eq. 3.2. In order to get the Eq. (5.9) and Eq. (5.10) solved numerically, it is necessary to incorporate the constraint stabilization method (CSM), thereby, it ensures that the constraint values quickly converges to zero upon any unexpected deflections. Here, we acquire the following equations [97]:

$$\ddot{R}_i + 2\alpha \dot{R}_i + \alpha^2 R_i = 0 \quad (i = 1, 2, \dots, n-1), \quad (5.11)$$

where  $\dot{R}_i$  and  $\ddot{R}_i$  are the first and second derivative of time, respectively. The parameter  $\alpha$  is the predetermined angular frequency and also plays as a damping coefficient for the constraints,  $R_i$ ; as a result, such constraints converge to zero rapidly. The results of  $\dot{R}_i$  and  $\ddot{R}_i$  are as follows:

$$\dot{R}_i = (v_{x_{i+1}} - v_{x_i})\delta x_i P_i + (v_{z_{i+1}} - v_{z_i})\delta z_i P_i, \quad (5.12)$$

$$\begin{aligned} \ddot{R}_i &= (\dot{v}_{x_{i+1}} - \dot{v}_{x_i})\delta x_i P_i + (\dot{v}_{z_{i+1}} - \dot{v}_{z_i})\delta z_i P_i \\ &\quad + [(v_{x_{i+1}} - v_{x_i})^2 + (v_{z_{i+1}} - v_{z_i})^2] P_i \\ &\quad - [(v_{x_{i+1}} - v_{x_i})\delta x_i + (v_{z_{i+1}} - v_{z_i})\delta z_i]^2 P_i^3, \end{aligned} \quad (5.13)$$

where

$$P_i = \frac{1}{\sqrt{\delta x_i^2 + \delta z_i^2}}. \quad (5.14)$$

Substitute  $\ddot{R}_i$ ,  $\dot{R}_i$ , and  $R_i$  into the Eq. (5.11), we can obtain the equations as below:

$$\mathbf{C}_x \dot{\mathbf{v}}_x + \mathbf{C}_z \dot{\mathbf{v}}_z = \mathbf{C}, \quad (5.15)$$

in which  $\mathbf{C}_x$  is a  $(n-1) \times n$  matrix, the value of each element is given as:

$$\begin{cases} C_{i,i} = \delta x_i P_i & (i = 1, 2, \dots, n-1) \\ C_{i,i+1} = -\delta x_i P_i & (i = 1, 2, \dots, n-1) \\ 0 & otherwise \end{cases} \quad (5.16)$$

Element values of  $\mathbf{C}_z$ , a  $(n-1) \times n$  matrix, will be likewise given with the same form, but replace  $\delta x_i$  by  $\delta z_i$ . Vector  $\mathbf{C}$  is determined as:

$$\begin{aligned} \mathbf{C}(x_i; x_{i+1}; z_i; z_{i+1}) &= [(v_{x_{i+1}} - v_{x_i})^2 + (v_{z_{i+1}} - v_{z_i})^2] P_i \\ &\quad - [(v_{x_{i+1}} - v_{x_i})\delta x_i + (v_{z_{i+1}} - v_{z_i})\delta z_i]^2 P_i^3 + 2\alpha \dot{R}_i + \alpha^2 R_i \\ &\quad (i = 1, 2, \dots, n-1). \end{aligned} \quad (5.17)$$

From the set of Eqs. (5.9), (5.10), (5.11) we will obtain the following equations of motion:

$$\begin{bmatrix} \mathbf{I} & \mathbf{0} & \mathbf{0} & \mathbf{0} & \mathbf{0} \\ \mathbf{0} & \mathbf{I} & \mathbf{0} & \mathbf{0} & \mathbf{0} \\ \mathbf{0} & \mathbf{0} & \mathbf{M} & \mathbf{0} & \mathbf{C}_x^T \\ \mathbf{0} & \mathbf{0} & \mathbf{0} & \mathbf{M} & \mathbf{C}_z^T \\ \mathbf{0} & \mathbf{0} & \mathbf{C}_x & \mathbf{C}_z & \mathbf{0} \end{bmatrix} \begin{bmatrix} \dot{\mathbf{x}} \\ \dot{\mathbf{z}} \\ \dot{\mathbf{v}}_x \\ \dot{\mathbf{v}}_z \\ \lambda \end{bmatrix} = \begin{bmatrix} \mathbf{v}_x \\ \mathbf{v}_z \\ \mathbf{F}_x \\ \mathbf{F}_z \\ \mathbf{C} \end{bmatrix}, \quad (5.18)$$

where  $\mathbf{I}_{n \times n}$  and  $\mathbf{0}_{n \times n}$  stand for unit and zero matrices;  $\mathbf{C}_x^T$  and  $\mathbf{C}_z^T$  are transpose matrix of  $\mathbf{C}_x$  and  $\mathbf{C}_z$ ;  $\mathbf{F}_x = [f_{x1} \ f_{x2} \ \dots \ f_{xn}]^T$  and  $\mathbf{F}_z = [f_{z1} \ f_{z2} \ \dots \ f_{zn}]^T$  are external force vectors that exert force on each node. In the case of Leafbot5,  $\mathbf{F}_x$  and  $\mathbf{F}_z$  are as follows:

$$\begin{bmatrix} f_{x1} \\ f_{x2} \\ f_{x3} \\ f_{x4} \end{bmatrix} = \begin{bmatrix} f_{cx}(\omega_v) - F_1^{fr} + k_\psi \psi_1 \tan \psi_1 A_1 - F_{zd} - b_x v_{x1} \\ -F_2^{fr} - k_\psi \psi_1 \tan \psi_1 A_1 + k_\psi \psi_2 \tan \psi_2 A_2 \\ -F_3^{fr} - k_\psi \psi_2 \tan \psi_2 A_2 + k_\psi \psi_3 \tan \psi_3 A_3 \\ -F_4^{fr} - k_\psi \psi_3 \tan \psi_3 A_3 \end{bmatrix}, \quad (5.19)$$

$$\begin{bmatrix} f_{z1} \\ f_{z2} \\ f_{z3} \\ f_{z4} \end{bmatrix} = \begin{bmatrix} f_{cz}(\omega_v) - k_\psi \psi_1 A_1 - 4k_z z_1 - m_1 g - b_z v_{z1} \\ F_2^{tf} + k_\psi \psi_1 A_1 - k_\psi \psi_2 A_2 - 2k_z z_2 - m_2 g - b_z v_{z2} \\ F_3^{tf} + k_\psi \psi_2 A_2 - k_\psi \psi_3 A_3 - 2k_z z_3 - m_3 g - b_z v_{z3} \\ F_4^{tf} + k_\psi \psi_3 A_3 - 2k_z z_4 - m_4 g - b_z v_{z4} \end{bmatrix}, \quad (5.20)$$

where  $F_i^{fr}$  is the friction force and is determined by the following function:

$$F_i^{fr} = \begin{cases} \mu_s m_i g & z_i \leq 0 \quad (i = 1, 2, \dots, n) \\ 0 & z_i > 0 \quad (i = 1, 2, \dots, n) \end{cases}. \quad (5.21)$$

In this context,  $\mu_s$  and  $g$  stand for the sliding friction coefficient and the gravitational constant, respectively. We only construct the model using the simplest form of friction, the Coulomb friction law. The friction coefficient  $\mu_s$  is determined by the experiment. The propelled force,  $F_{zd}$ , induced by the deformed limbs in the  $Z$  direction acting in the  $X$  direction, is acquired as the below equation. This relation is obtained by experiment and depends on the morphological limb (see Figure 3.5). In this section,  $F_{zd}$  is equal to  $F_x^{4-limb}$ , determined in Figure 3.5.

$$F_{zd} = \begin{cases} \frac{1}{2} 4k_z z_1 = 2k_z z_1 & z_1 \leq 0 \\ 0 & z_1 > 0 \end{cases}. \quad (5.22)$$

The notation  $A_i$  is the shorten form of the following expression:

$$A_i = \frac{1}{\delta x_i (\tan^2 \psi_i + 1)} \quad (i = 1, 2, \dots, n-1), \quad (5.23)$$

and  $F_i^{tf}$  stand for the transverse force caused by the transverse wave as presented in the preliminary observation section and can be calculated by the beneath equation [98]:

$$F_i^{tf} = T_f \sin \psi_{i-1} = \frac{L_w^2 \gamma}{\tau^2} \sin \psi_{i-1} \quad (i = 2, 3, \dots, n), \quad (5.24)$$

where  $T_f$  is the tension force and can be inferred from  $L_w$ ,  $\gamma$ , and  $\tau$ . The length between marker 2 and marker 3 is  $L_w$ , whereas the time difference between marker 2 and marker 3 is  $\tau$ . They are presented in the above section. The mass density of Leafbot (per unit length) is  $\gamma$  [98]. Note that nonconservative forces, including viscous forces - denoted by  $b_x v_x$  and  $b_z v_z$ ,  $F_i^{fr}$ ,  $F_{zd}$ ,  $F_i^{tf}$ , and centripetal forces, are incorporated into  $\mathbf{F}_x$  and  $\mathbf{F}_z$ .

Regarding the stiffness parameter,  $k_\psi$ , we employed a high precision force gauge, IMADA ZTS-5N whose resolution is 0.001 N, to measure the bending stiffness values of  $k_\psi$ . The stiffness  $k_z$  is presented in Figure 3.5. Concerning the damping coefficient of silicone rubber,  $b_x$ ,  $b_z$ , we initially determined the logarithmic decrement from the motion capture video to find the damping ratio as well as the damping coefficient. Refer to the Appendix section to get the experimental values. Using the *ode45* function in MATLAB to numerically solve the set of Eq. (5.18). Its solution returns position and velocity vectors in the  $X$  and  $Z$  directions.

## 5.2 Experimental scheme for Leafbot's locomotion evaluation

### 5.2.1 Experimental design for locomotion verification

We adopted the marker-based motion capture method to verify the locomotor modes of Leafbot designs. Section 4 describes our initial use of HSC to analyze Leafbot's poses. However, due to Leafbot's rapid movement, Leafbot is out of the HSC's captured range after about 0.8 seconds, limiting the model's validation over longer periods. Therefore, we proceeded with another marker-based tracking platform, OptiTrack with Motive software version 2.1.2, which is less accurate in the  $Z$  direction but effectively tracks Leafbot's trajectories over longer periods of time in the  $X$  direction.

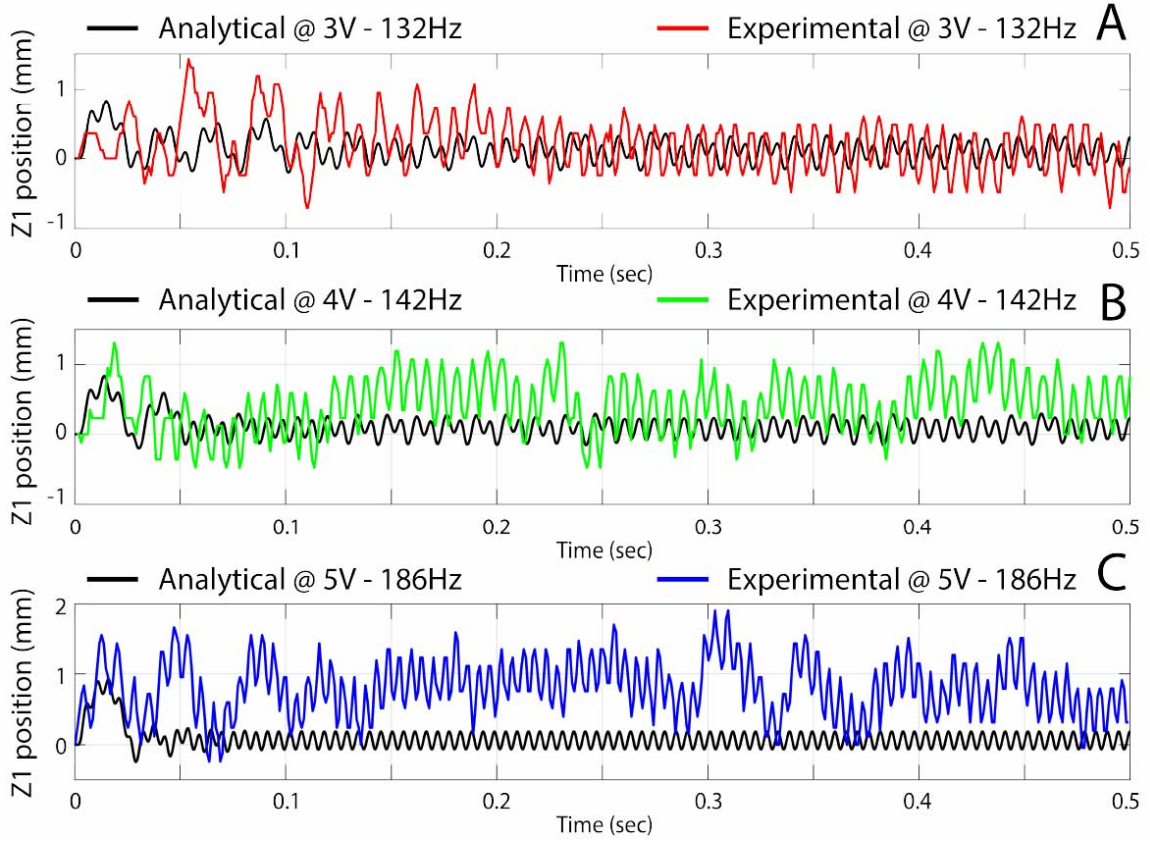


Figure 5.2: (A), (B), (C) The trajectory of the 1st marker in the  $Z$  direction determined by experimental method and analytical model under the three pre-determined excitation freqs.: 132 Hz, 142 Hz, and 186 Hz, respectively.

## 5.2.2 Outcomes obtained from the experimental and analytical methods

In the initial step, we verified the locomotion posture by analyzing all markers' motions as shown in Figure 4.1. Each marker was processed by the OpenCV module to export an array of marker's positions with respect to time  $[[t_0, \hat{x}_1^0, \hat{z}_1^0], [t_1, \hat{x}_1^1, \hat{z}_1^1] \dots [t_k, \hat{x}_1^k, \hat{z}_1^k]]$ .  $\hat{x}_1^k$  is the  $X$  position of the first marker at the time  $k$ , and  $\hat{z}_1^k$  is likewise but at the  $Z$  position. All markers were processed to collect posture information data. These coordinate values were utilized to evaluate the analytical model.

### 5.2.2.1 Results in the $Z$ direction

Regarding the pose in the  $Z$  direction, the first marker exposes the motion mode in the  $Z$  axis. Under the vibration excitation, the front-end robot section, including the vibrator and vibrator housing, bounces up and down on the moving surface. This jumping-like gait is

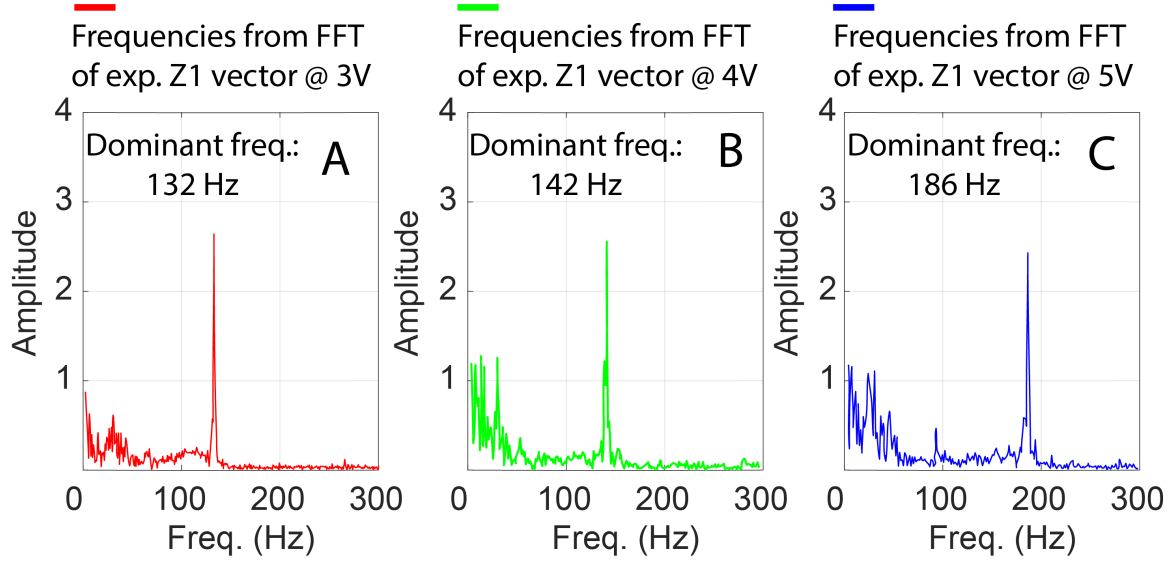


Figure 5.3: (A), (B), (C) The collected dominant freq. in freq. domain by FFT from experimental data of vector  $\hat{z}_1$  at pre-determined excitation freq. 132Hz, 142Hz, and 186Hz, correspondingly.

verified by either the analytical or empirical method in three contexts of stimulus frequencies 3V - 132 Hz, 4V - 142 Hz, and 5V - 186 Hz. The analytical results are depicted with the black lines, whereas the red, green, and blue ones represent the experimental outcomes of the applied freq. 132 Hz, 142 Hz, and 186 Hz, respectively (see Figure 5.2). The analytical graphs show that some bouncing trajectories partially fall into the negative area due to the first limb's deformation, leading to the negative values of  $z_1$  (see the selected coordinate of origin in Figure 5.1 or Figure 4.1).

The bouncing trajectories exhibit a noisy sine wave-like motion across all nodes (see Figure 5.2 and Figure 5.4). This behavior is generally induced by three main factors. Firstly, the interference of various vibrating frequencies is generated from the vibration source, especially the oscillation from the motor tether. To mitigate this, a very thin copper wire (AWG24) was used to reduce interference. Secondly, experimental errors occur during the motion capture process. With markers only 2 mm in diameter, the center of each marker may be less accurately detected by the OpenCV package. Lastly, contact between each limb and the ground during the jumping motion generates reaction forces, leading to complex motion behaviors that the analytical model cannot fully capture. Despite the noisy trajectories, the frequencies identified through the Fast Fourier Transform (FFT) from the  $Z$  data of the first marker appear dominantly in the frequency domain (see Figure 5.3). Similar results were obtained for all nodes, with each marker showing the same dominant frequencies at a given voltage. These prevailing

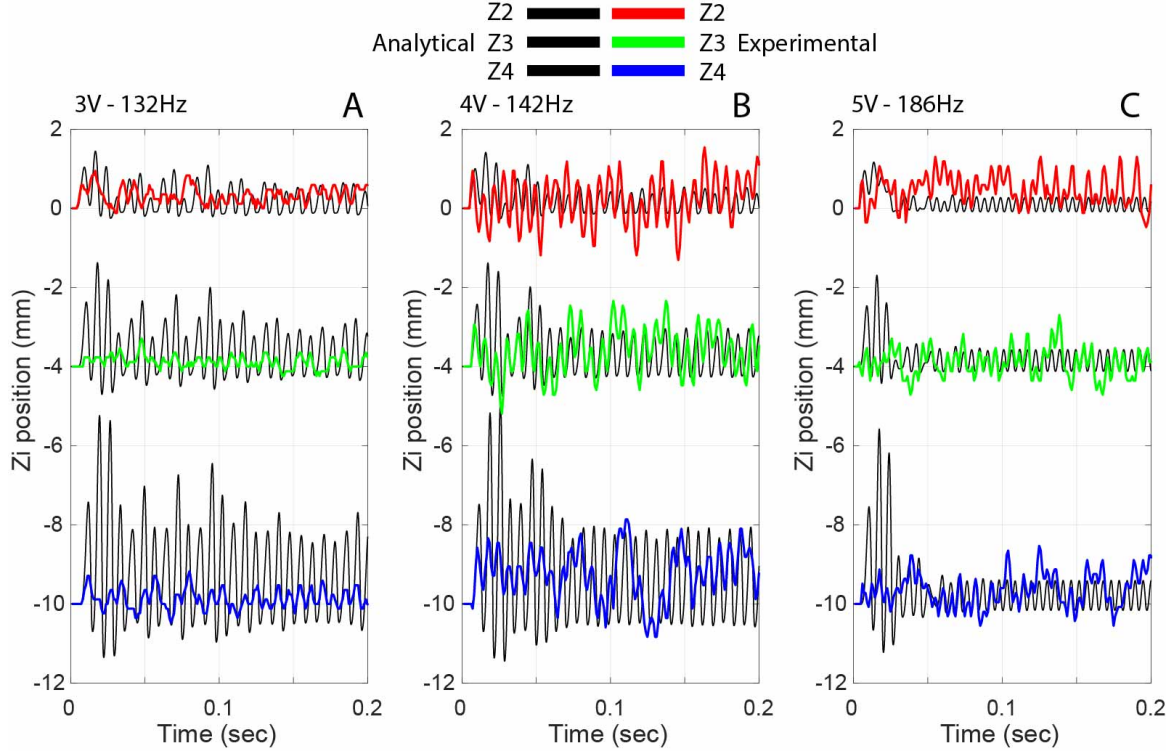


Figure 5.4: (A), (B), (C) The trajectories of the 2nd to the 4th node in the  $Z$  direction are determined by experimental method and analytical model under the three pre-determined excitation freqs.: 132 Hz, 142 Hz, and 186 Hz, respectively. For ease of observation,  $z_2$  and  $z_3$  lines are offset 4 mm, apart.  $z_3$  and  $z_4$  lines are 6 mm.

frequencies represent the angular frequencies of the employed vibration motor for each applied voltage, as discussed and verified in Section 4.1.

To sum up, the output solutions of  $z_i$  from the mathematical model are acceptable. Firstly, it presents the jumping gaits of all nodes, closely matching the trajectories of tracked markers at each oscillation frequency. Although the acquired graphs from markers appear bumpy, they all display clear and explicit sinusoidal waves and are in phase with the analytical model lines. Furthermore, the model captures limb deformation during ground interaction, resulting in sinusoidal curves that extend into the negative region of the graph (See the trajectories of the first markers in Figure 5.2). Secondly, despite the amplitude discrepancies between the model and experimental results shown in Figure 5.2 and Figure 5.4, these errors are acceptable for the following reasons: they may be due to the method of conducting the experiment, but the key concern is whether jumping gaits occur on all nodes, as this affects the total friction forces on Leafbot's limbs and impacts its forward motion. Observations reveal that at 4 V - 186 Hz and 5 V - 191 Hz, Leafbot3 does not exhibit jumping gaits at the second and third nodes, leading to a significant reduction in its average velocities.

### 5.2.2.2 Results in the $X$ direction

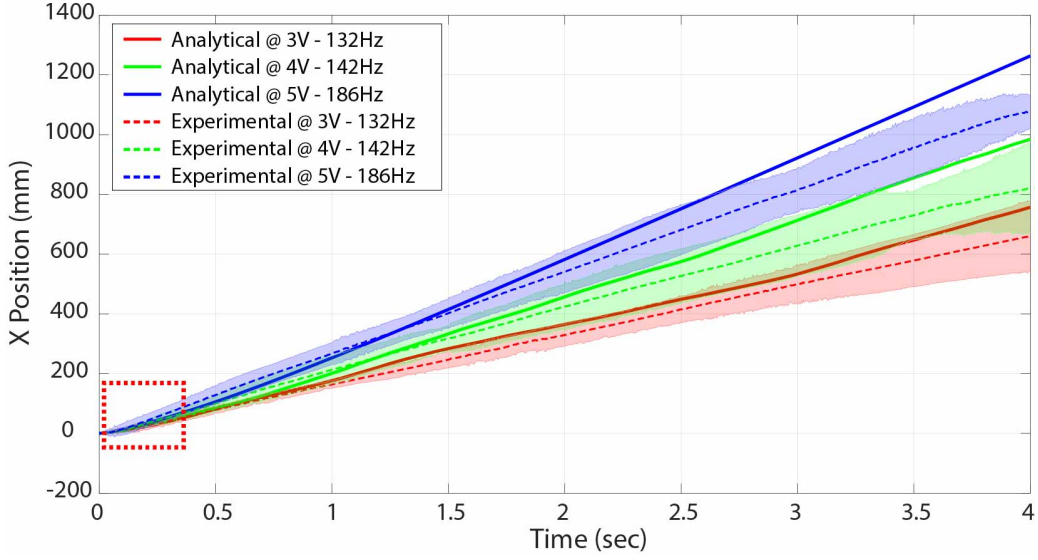


Figure 5.5: The position of the marker on Leafbot5 tracked by the OptiTrack system over time is presented between analytical and experimental data. The area enclosed by the red-dash line is presented in Figure 5.7.

To investigate the displacement of Leafbot3, Leafbot5, and Leafbot9 along the  $X$ -axis, we employed the OptiTrack optical motion capture platform to track a lightweight marker attached to Leafbot's backbone in four seconds. We still use the mocap with the HSC to track the first reflective green marker and observe the locomotion behavior of Leafbot in a very short period of time. The evaluation of our proposed model and the experimental values for Leafbot5's motion in the  $X$  direction under three different excitation frequencies are shown in Figure 5.5. The entire Leafbot moves at the same speed. Thus, the  $X$ -direction results from the tracked marker on the Leafbot's backbone match those from the first node in the mathematical model in terms of the method of obtaining data. We conducted five trials to record the position data on each vibration frequency. The dashed lines represent the mean position data, and shaded areas stand for the three standard deviations ( $3*SD$ ). We also analyzed  $X$ -direction velocity using the time-position data to better understand the motion behavior. The average velocities of the marker mounted on the soft backbone at 132 Hz, 142 Hz, and 186 Hz on an overall recorded time domain were determined. These experimental values were plotted in conjunction with the  $\dot{x}_1$  (see Figure 5.6), which was numerically computed from Eq. 5.18.

The experimental method validates the  $X$ -axis displacements from the analytical model (see Figure 5.5). The yielded solutions of  $x_1$  at three frequencies mostly fall within the shaded area ( $3*SD$ ). The errors between the model and the mean values may arise from three factors that



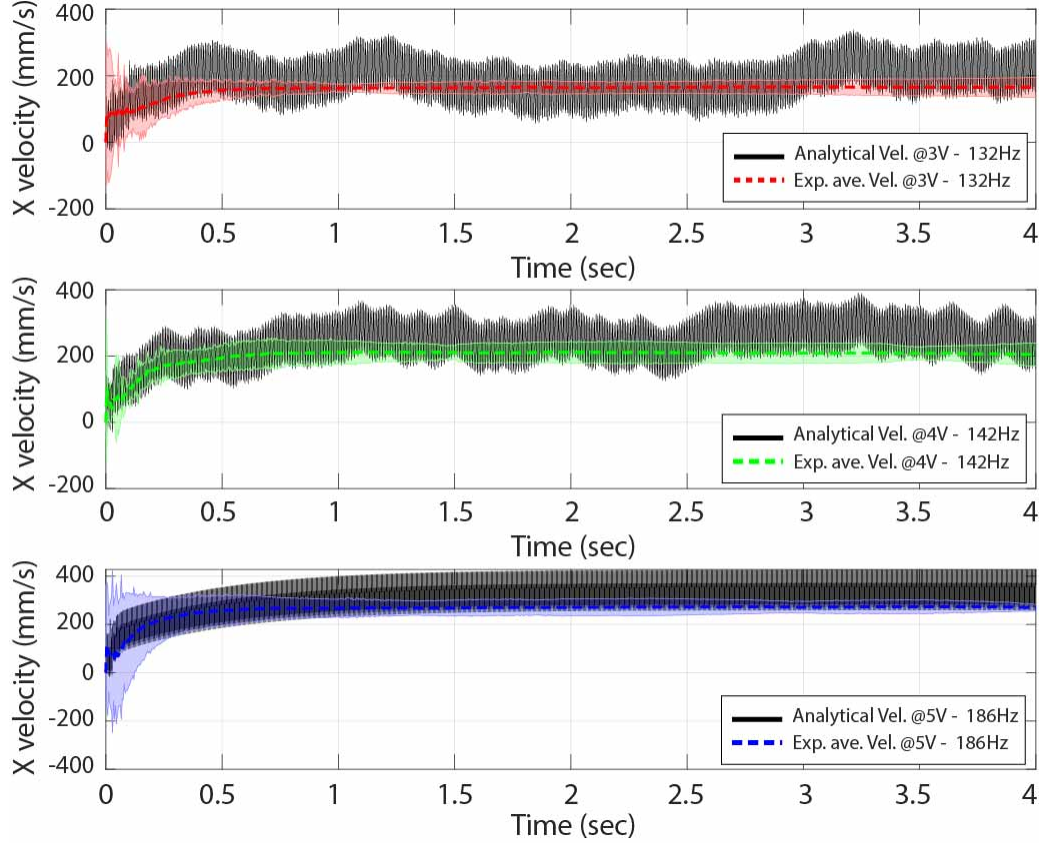


Figure 5.6: Attained velocity,  $\dot{x}_1$ , from the analytical model, and average velocity from the experimental results of the marker, tracked by OptiTrack system along the  $X$  direction.

the model cannot fully account for, including the friction between the motor tether and the environment, the complex frictional contact between limbs and the tested surface, and viscous damping of the silicone rubber material forming Leafbot.

The horizontal velocity depicted in Figure 5.6 reveals that the numerical result of  $\dot{x}_1$ , represented by the black solid line, reflects the basic principle of vibration-based locomotion in our model. The locomotion basis is not merely a uniform motion. The robot body accelerates and decelerates rapidly and repeatedly between cycles. Over a four-second period, all numerical results of  $\dot{x}_1$  increase and then fluctuate near particular converged values, *i.e.* after approximately one second,  $\dot{x}_1$  starts oscillating around 200 mm/s, 220 mm/s, and 300 mm/s at 132 Hz, 142 Hz, and 186 Hz, respectively. This phenomenon exhibits the intrinsic characteristic of the vibration-based design that the instantaneous velocity of Leafbot follows sinusoidal rather than straight lines, which were similarly observed in prior models [4, 37, 88]. This behavior is illustrated in Figure 5.7, where data is plotted in a short duration. The velocity graph also explains the  $X$  data's errors between the analytical and experimental models, with most instantaneous velocities exceeding the mean plus  $3 \times \text{SD}$ . However, due to the convergence

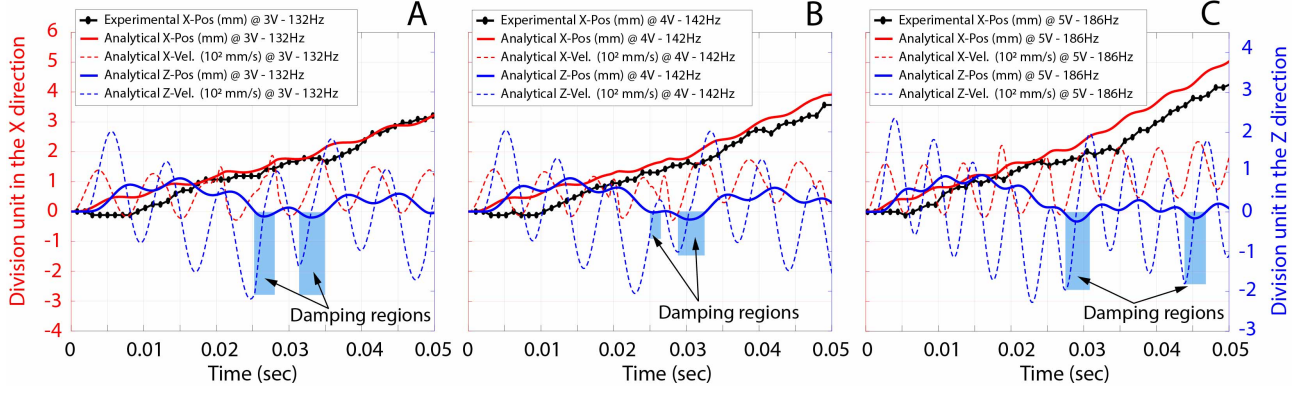


Figure 5.7: The  $x_1$ ,  $\dot{x}_1$ ,  $z_1$ , and  $\dot{z}_1$  results of Leafbot5 from the analytical model are illustrated in a very short time domain.

of  $\dot{x}_1$  oscillating around specific values, the robot's  $X$  position over time can be considered linear rather than exponential over a longer testing period. These positioning errors can be compensated by embedding Leafbot into a feedback system.

To further understand our proposed dynamics model, we present the red dashed line results from Figure 5.5 over a very short period (see Figure 5.7). Please note that the line notations in Figure 5.7 have been changed for clarity. Two points are highlighted in Figure 5.7. First, the red dashed line stands for the  $X$  velocity. Due to the sinusoidal shape of  $\dot{x}_1$ , the  $x_1$  displacement does not grow constantly but includes straight and horizontal motion steps. Analogous movements are observed in the experimental data from the first reflective marker (we employed the mocap method with the green marker and the HSC in this case). Second, when  $z_1 < 0$ , the first node contacts the ground, causing limb deformation and damping (damping regions), leading to the rapid drops of the velocities ( $\dot{z}_1$  - the blue dashed line). The blue regions are where the Eq. 5.5 and Eq. 5.22 apply.

The dynamics of Leafbot3 and Leafbot9 are shown in Figure 5.8 and Figure 5.9. Generally, the model's outcomes align with empirical data across all frequencies for both designs. Leafbot9's displacement over four seconds is lower than Leafbot5 and Leafbot3 at 3V. The greater number of limbs in Leafbot9 causes more friction, reducing displacement. Conversely, Leafbot3, with fewer limbs, travels a greater distance in four seconds at 3V. However, at 4V - 186 Hz, 5V - 191 Hz, Leafbot3 delivers abnormal results, with displacements after four seconds being lower than in other cases. This issue is due to vibration frequencies causing the second and third nodes to remain stationary. Video footage reveals that the transverse wave does not occur along the back of Leafbot3's backbone; the front limb with the vibrator was jumping while the limbs behind ceased bouncing. Consequently, the rear limbs make constant contact

with the ground, increasing friction and reducing displacement.

In conclusion, we present a study on the dynamics model of vibration-based soft robots with three different limb patterns. The model was thoroughly verified empirically. For  $X$ -axis locomotion, we focused on the first marker, which adequately and accurately reflects the robot's motion. Plotting the  $X$  position of the additional markers is unnecessary, as the entire body moves at the same velocity throughout the testing period.

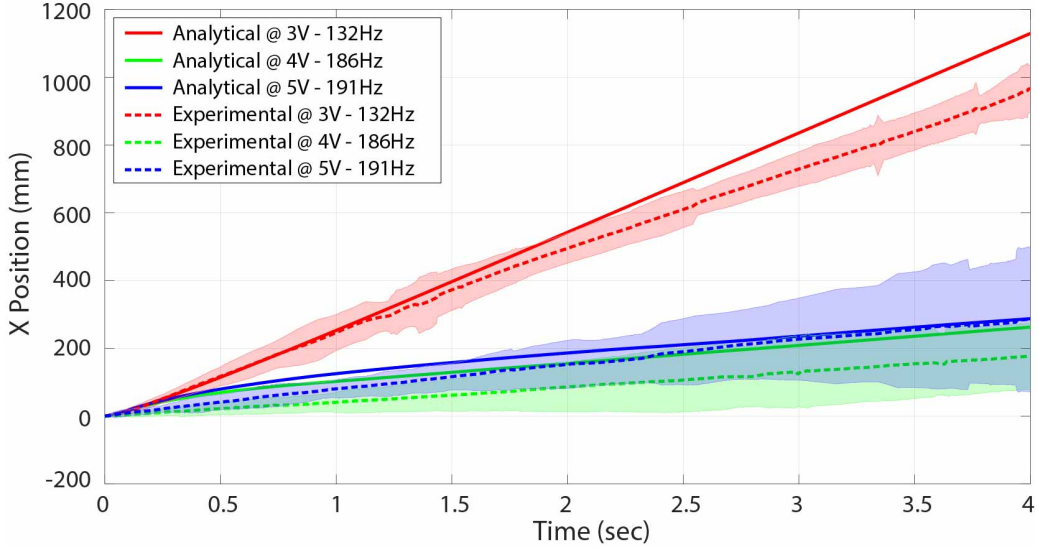


Figure 5.8: The position of the marker on Leafbot3 tracked by the OptiTrack system over time is presented between analytical and experimental data.

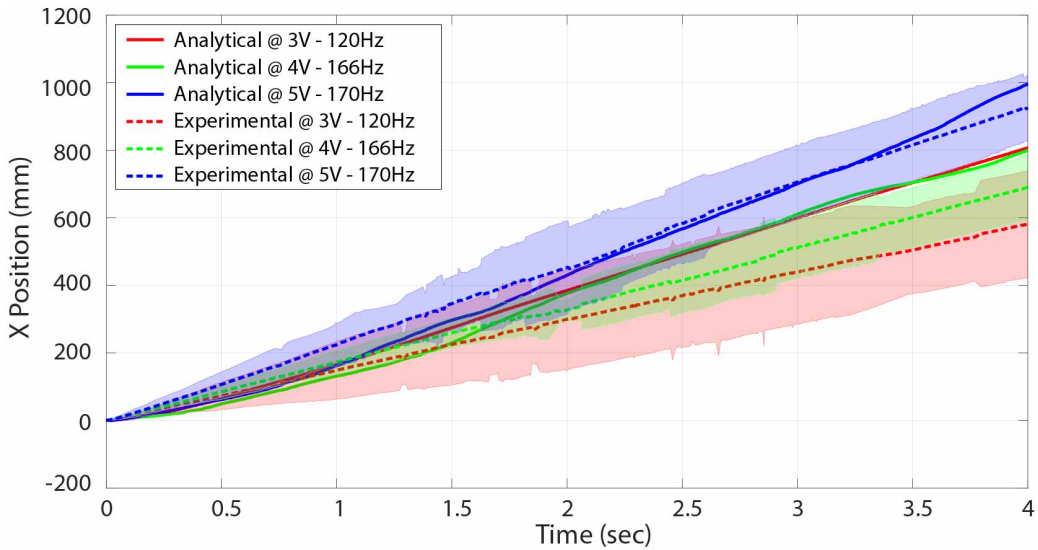


Figure 5.9: The position of the marker on Leafbot9 tracked by the OptiTrack system over time is presented between analytical and experimental data.

### 5.3 Terradynamics study of Leafbot

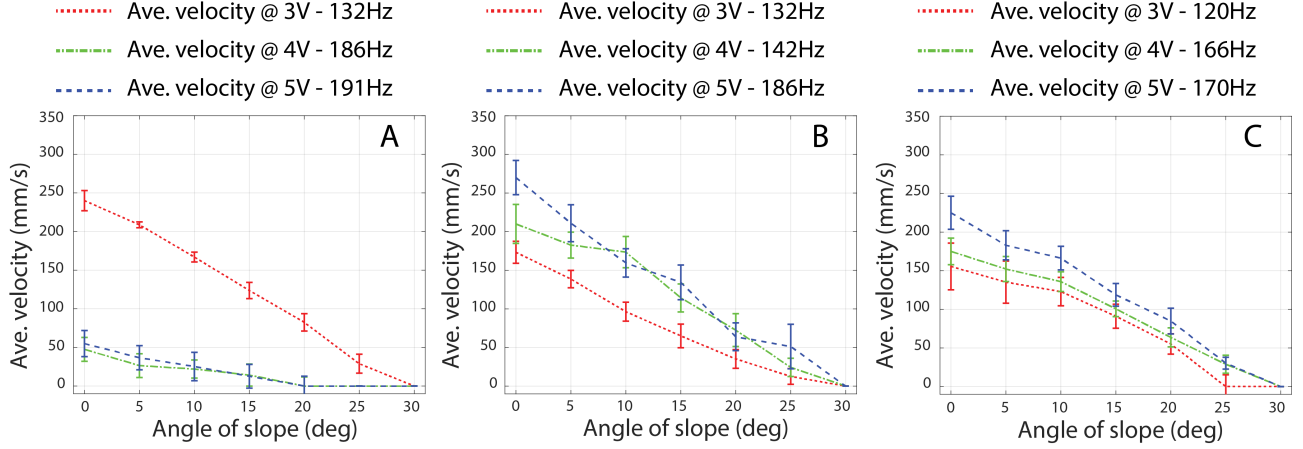


Figure 5.10: Obtained ave. velocity at three limb pattern variants on the ascending slope angle. (A) Leafbot3; (B) Leafbot5; (C) Leafbot9.

Locomotion posture in uni-direction and on flat terrain is investigated in the above section. Here, we explore the traversal capability of three limb patterns (Leafbot3, Leafbot5, Leafbot9) on various terrains (see Figure 3.8). Firstly, we assessed the average velocity of these designs on slopes (see Figure 5.10). All designs were hindered from moving forward at a 30 deg or higher slope due to the bouncing characteristics, which prevented the limbs from maintaining sufficient friction and caused the robot to slide backward under gravity. A general trend is observed: designs with more limbs deliver a slower locomotion speed. However, as demonstrated in the analytical section, Leafbot3 only outperforms Leafbot5 and Leafbot9 at 3V - 132 Hz due to having fewer limbs. At 4V - 186 Hz and at 5V - 191 Hz, Leafbot3 fails to deliver the locomotion as fast as Leafbot5 and Leafbot9.

Secondly, we further evaluated the terrain traversability of three design patterns by adopting a geometry-based methodology that characterizes the terrain properties in terms of geometry (slope, height, roughness, and rugosity) and texture (rocks or soil/sand) [14, 99–103]. Within this paper, we merely focus on investigating the effect of slopes and height of obstacles, whose parameters are mostly considered on the traversability [16, 99, 104]. We call  $S_r$  the function of the success rate of terrainability:

$$S_r(h, \beta, \kappa, \Pi) \in [0 \ 1]. \quad (5.25)$$

$S_r$  is a function of height  $h$ , slope  $\beta$ , the bending stiffness of the robot backbone  $\kappa$ , and

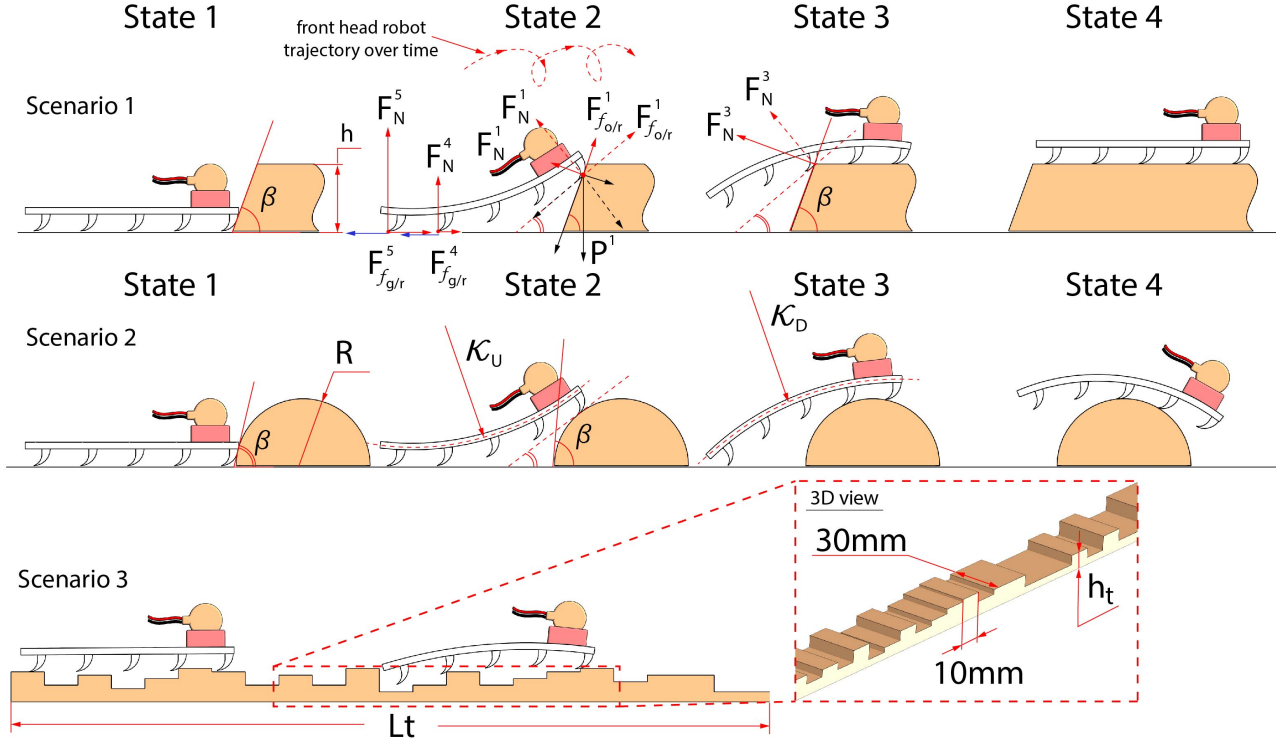


Figure 5.11: The traversability experiment scheme. Scenario 1: The robot traversed through slope obstacles characterized by slope  $\beta$  and height  $h$ . Scenario 2: The robot traversed through semi-circular-like obstacles characterized by  $R$ . Scenario 3: The robot traversed through a designed terrain characterized by the rugosity  $R_g$  factor.

limb pattern II. Note that we conducted several tests and reported that an increase in the thickness of the soft backbone leads to higher bending stiffness, which diminishes Leafbot's traversability. Nevertheless, the bending stiffness is fixed for the design within this paper. Thus, the terrainability function  $S_r$  only relies on height, slope, and limb pattern. We employed the empirical method to consider the consequence of each parameter on the overcoming obstacle success rate. Our experimental scheme is presented in Figure 5.11. We divided our test into three scenarios. The traversability of our design was evaluated in such scenarios. The obstacles and the rugose terrain in the three examined scenarios were printed with PLA material. Additionally, the front curve of the robot's limb directly contacts the obstacles' slopes and curves. The printing method should be reported since it might have a certain impact on the robot's traversal. The obstacles were placed on the printing pad like the setup shown in Figure 5.11. Each layer was printed and stacked sequentially from the base upwards. Thus, the slope and curves of the obstacles resemble fine steps. Each layer had a thickness of 0.15 mm. Now, we explain the underlying physics of the ability to negotiate irregularities of the predefined terrain of our proposed design concept.

### 5.3.1 Scenario 1: Slope locomotion

In scenario 1, we examined the traversability success rate through slope obstacles characterized by slope,  $\beta \in [30\ 90]$  deg, and height,  $h \in [1\ 5h_{hip}]$ . The hip height of our robot design is  $h_{hip} = R_1 = 5$  mm. Since the obstacle height should be considered relatively high to the robot's height when evaluating the overcoming performance, hip height is taken into consideration [16]. In scenario 1, a successful case of overcoming the obstacle is considered when the robot goes through state 1 to state 4, where the entire robot body completely gets over the slope. In State 1, the robot approaches the obstacle with the front-curved morphology ( $R_1 = 5$  mm) of the first limb tangentially contacting the slope. Because the robot's trajectory is bouncing ahead, the first limb of the robot kept crawling on the slope in State 2, which is crucial for traversing the obstacle. If the first leg is not able to securely anchor the front head to the ramp, the entire robot body can not overcome the slope. During State 2, the induced friction from the limb pattern plays a vital role in preventing the robot from slippage from the slope. The soft backbone of Leafbot is designed to bend into a necessary curve, ensuring the first limb tangentially contacts the ramp, generating sufficient friction to crawl over. This flexible design allows the robot to deal with slopes up to 90 deg as long as the obstacle height is within a specific limit.  $F_{f_{o/r}}^1$  is the induced friction between the obstacle and the first limb of the robot.  $F_{f_{g/r}}^4$  and  $F_{f_{g/r}}^5$  are the friction between the ground and the robot's fourth and fifth limbs, respectively.  $f_{o/r}$  represents the friction from the obstacle against the downward sliding of the robot limb, whereas  $f_{g/r}$  is the friction from the ground against the limb's motion. For instance, sliding friction (the blue arrows) opposes the robot's rightward movement. When the first limb contacts the slope, a resistance force is exerted on it. The steeper the  $\beta$  angle, the higher the resistance force, which creates opposing friction forces  $F_{f_{g/r}}^4, F_{f_{g/r}}^5$  (the red arrows). This friction prevents the robot from slipping backward; nevertheless, as presented above, the robot bounces during the locomotion. As a result,  $F_{f_{g/r}}^4, F_{f_{g/r}}^5$  could plunge to zero due to the non-contact or less contact between the robot limbs and the ground. A non-slip condition during State 2 can be expressed as follows, in which the left-hand side (LHS) is the total induced friction on all limbs except the first limb contacting the obstacle:



$$\sum_{i=2}^n F_N^i(c_p)\mu_g \geq [P^1 \sin \beta - F_N^1(c_p)\mu_o] \cos \beta + m_1 \left\| \frac{d\mathbf{v}_1}{dt} \right\| (1 - \cos \beta), \quad \forall \beta \in [0, \pi/2], \quad (5.26)$$

where  $F_N^i(c_p)$  is the normal force that the ground or obstacles exert on limbs in contact with them;  $P^1$  is the weight of Leafbot at the front-end region and equal to  $m_1 g$  ( $m_1$  is the mass of the first node);  $\mu_g$   $\mu_o$  are the sliding friction coefficients for the limbs with the ground and obstacle, respectively; and  $\mathbf{v}_1$  is the velocity vector of the first node. Due to the bouncing,  $F_N^i(c_p)$  relies on a contacting parameter called  $c_p$  as shown below:

$$c_p = \begin{cases} > 0 & \text{non-contact} \\ \leq 0 & \text{contact} \end{cases}. \quad (5.27)$$

The normal force is completely dependent on the contact condition and defined by  $c_p$ . The friction force is likewise, either depending on the normal force or  $c_p$ :

$$F_N^i(c_p) = \begin{cases} 0 & c_p > 0 \\ m_i g & c_p \leq 0 \end{cases}, \quad (5.28)$$

$$F_{f_{g/r}}^i = \begin{cases} 0 & c_p > 0 \\ F_N^i(c_p)\mu_g & c_p \leq 0 \end{cases}. \quad (5.29)$$

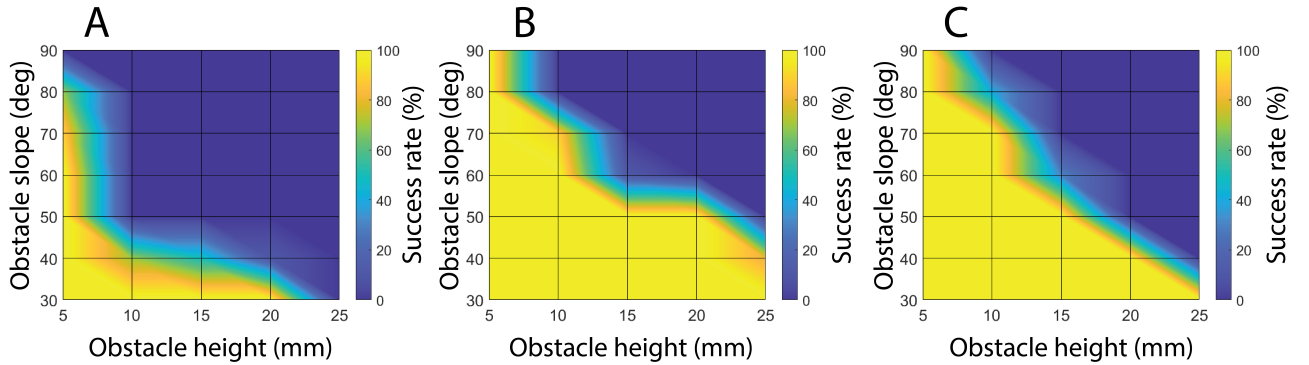


Figure 5.12: The traversal success rate,  $S_r$ , of Leafbot's patterns in Scenario 1. (A) Leafbot3; (B) Leafbot5; (C) Leafbot9.

If the non-slip condition is satisfied, the first limb of the robot will overcome the slope and enter State 3, where the front head of the robot is on the obstacle, while the rest of the body is obstructed by the soft backbone's deformation. The front head must generate an

adequate thrust force to surpass the resistant force on the remaining legs to bring the entire body into State 4. These four states illustrate the mechanism by which our robot overcame predetermined obstacles. However, solving Eq. (5.26) or determining  $c_p$  is challenging due to the robot's locomotion characteristics. The complexity of the trajectory of each limb led to the difficulty in identifying the time at which the contact of a particular limb took place. As a result, Eq. (5.26) is not always satisfied during obstacle traversal. However, by increasing the value of  $n$  (the number of limbs), the total induced friction can be enhanced, reducing the chance of slippage in State 2 and increasing the likelihood of reaching State 3. This means the model should be designed with more limbs to gain more friction.

Here, we verified this solution by evaluating the success rate of overcoming the obstacles of three designs [16, 17]. For each design pattern, we tested seven values of the slope,  $\beta = \{30, 40, 50, 60, 70, 80, 90\}$  deg and five values of obstacle heights  $h = \{5, 10, 15, 20, 25\}$  mm, equivalent to one to five times the robot's hip height,  $h_{hip} = R_1 = 5$  mm. We conducted ten trials on each pair of slopes and bumps,  $\beta, h$ , respectively, starting with the highest values and moving to the lower ones. When a pair of  $\beta$  and  $h$  achieved 100% success rate, we tested lower values in five trials to save time. The traversal success rate of each pattern is shown in Figure 5.12. The color regions between examined pairs of height and slope are obtained by the interpolation method provided by MATLAB software. Leafbot3 shows the poorest terrain traversal ability, managing to pass low-slope terrains of 30 deg or less. It only has a high chance of overcoming slopes greater than 30 deg if the obstacle height is 10 mm ( $2h_{hip}$ ) or less. In contrast, Leafbot5 and Leafbot9 demonstrate much better traversability, effortlessly overcoming slopes of 40 deg or less with almost any height value. Nevertheless, both patterns struggle with slopes greater than 50 deg. At this point, the robot solely performs efficiently with  $h \approx 4h_{hip}$ . When slopes approaching 90 deg, Leafbot5 and Leafbot9 can only deal with  $h \approx 2h_{hip}$ . Leafbot5 slightly outperforms Leafbot9 in Scenario 1 since it is able to traverse at ( $h = 20$  mm;  $\beta = 50$  deg) and ( $h = 25$  mm;  $\beta = 40$  deg), while Leafbot9 locomotion is completely obstructed at these testing parameters.

### 5.3.2 Scenario 2: Semi-circular obstacles traversability

In scenario 2, we examined the traversability with the semi-circular obstacles. In Scenario 1, due to the geometric features of the bumps, fewer limbs contacted the obstacle, resulting in less friction. Therefore, in Scenario 2, we considered curved objects to evaluate the contact



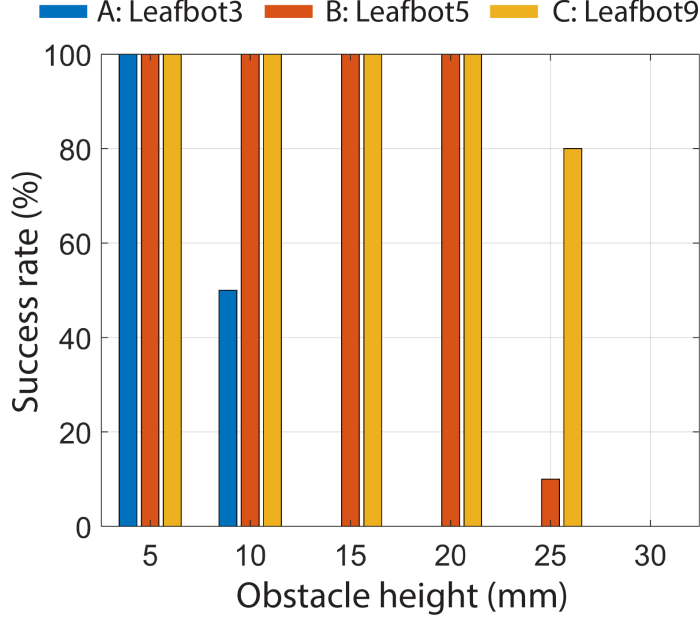


Figure 5.13: The traversal success rate,  $S_r$ , of Leafbot's patterns in Scenario 2: (A) Leafbot3, (B) Leafbot5, and (C) Leafbot9.

mechanism of different patterns further. The bendability of the robot backbone was expected to increase limb contact with the semi-circular obstacles, enhancing the sum of the LHS of the Eq. (5.26). The experiment proceeded likewise in Scenario 1. Each pattern design was set to go through semi-circular obstacles. The radius of the tested obstacle  $R = \{5, 10, 15, 20, 25\}$  mm, equal to one to five times the robot's hip height. Based on the radius of the curve, shown below:

$$Oz(x) = \sqrt{R^2 - (x - a)^2} \quad (0 \leq x \leq a = R), \quad (5.30)$$

the slope at each contact point can also be inferred from the derivative of the semi-circular equation. The success rate of the traversability of the robot in Scenario 2 is shown in Figure 5.13.

The outcome of this experimental scenario shows that Leafbot3 still delivers the worst traversability performance on semi-circular obstacles, overcoming a maximum height of twice its hip height  $h_{hip}$ . Leafbot5 can traverse obstacles up to four times its hip height with a 100% success rate, but this drops to 10% for obstacles with a radius of  $R = 5h_{hip}$ , which means the robot could only succeed one in ten trials. Leafbot9 brings the best performance when dealing with semi-circular objects up to five times its hip height, only failing at heights greater than six times  $h_{hip}$ .

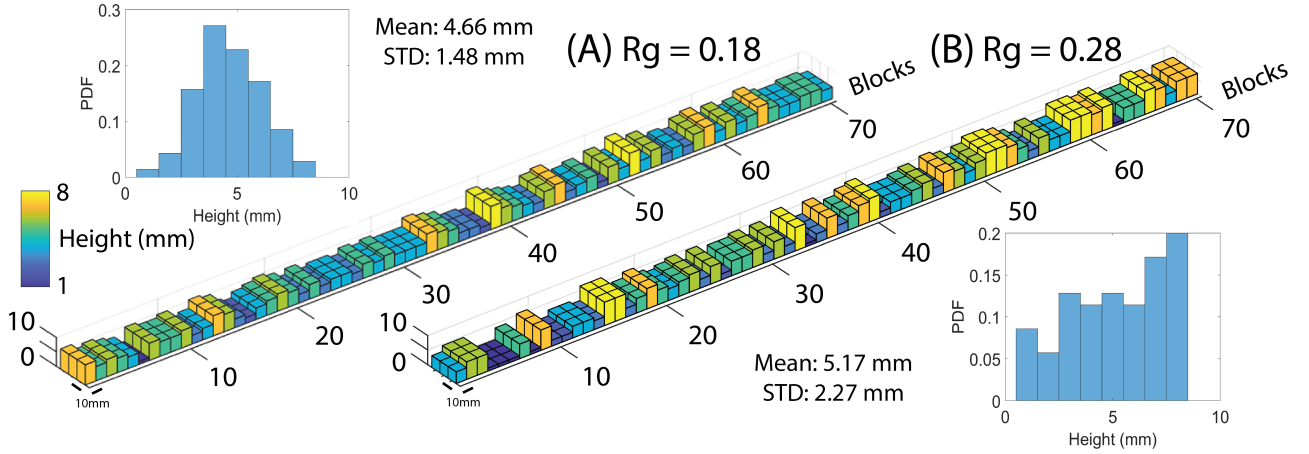


Figure 5.14: The step-field terrain was constructed based on the rugosity. (A)  $R_g = 0.18$ , (B)  $R_g = 0.28$ .

### 5.3.3 Scenario 3: Rugose terrain traversability

In scenario 3, we evaluated the terrainability of the robot based on the rugosity factor,  $R_g$ . This step-field terrain has been used to assess the robot's mobility performance [14, 87]. The terrain was constructed by combining various blocks of size ( $10 \text{ mm} \times 30 \text{ mm} \times h_t$ ) (see Figure 5.11 Scenario 3). These block dimensions were advised to be selected relative to the robot dimension, and the robot's footprint was considered as large as 1/4 to 1/3 the area of the step-field block [87]. The height values ( $h_t$ ) of these blocks were randomly distributed and characterized via the terrain rugosity factor  $R_g$ . This factor is expressed as the normalized standard deviation of the block heights relative to the maximum height, which is approximately 1.5 times the center of Leafbot's mass (5 mm). (see Figure 5.14). The block height,  $h_t$ , varies from 1 mm to 8 mm with 1 mm increment. By this method, two terrains with a mean and standard deviation of 4.66 mm and 1.48 mm for the  $R_g = 0.18$  terrain and 5.17 mm and 2.27 mm for the  $R_g = 0.28$  terrain, respectively, were obtained. A set of 70 random numbers of  $h_t$  is generated by MATLAB, following a normal distribution, to form the corresponding terrains with the length,  $L_t = 700 \text{ mm}$ . Since MATLAB might generate numbers outside the range of one to eight, constraints are applied to these out-of-range values as follows:

$$h_t = \begin{cases} 1 & h_t < 1 \\ 8 & h_t > 8 \end{cases}. \quad (5.31)$$

With this technique, we can obtain a set of 70 random numbers ranging from one to eight. After being printed by a 3D printer with PLA material, 70 blocks, sizing ( $10 \text{ mm} \times 30 \text{ mm} \times h_t$ ),

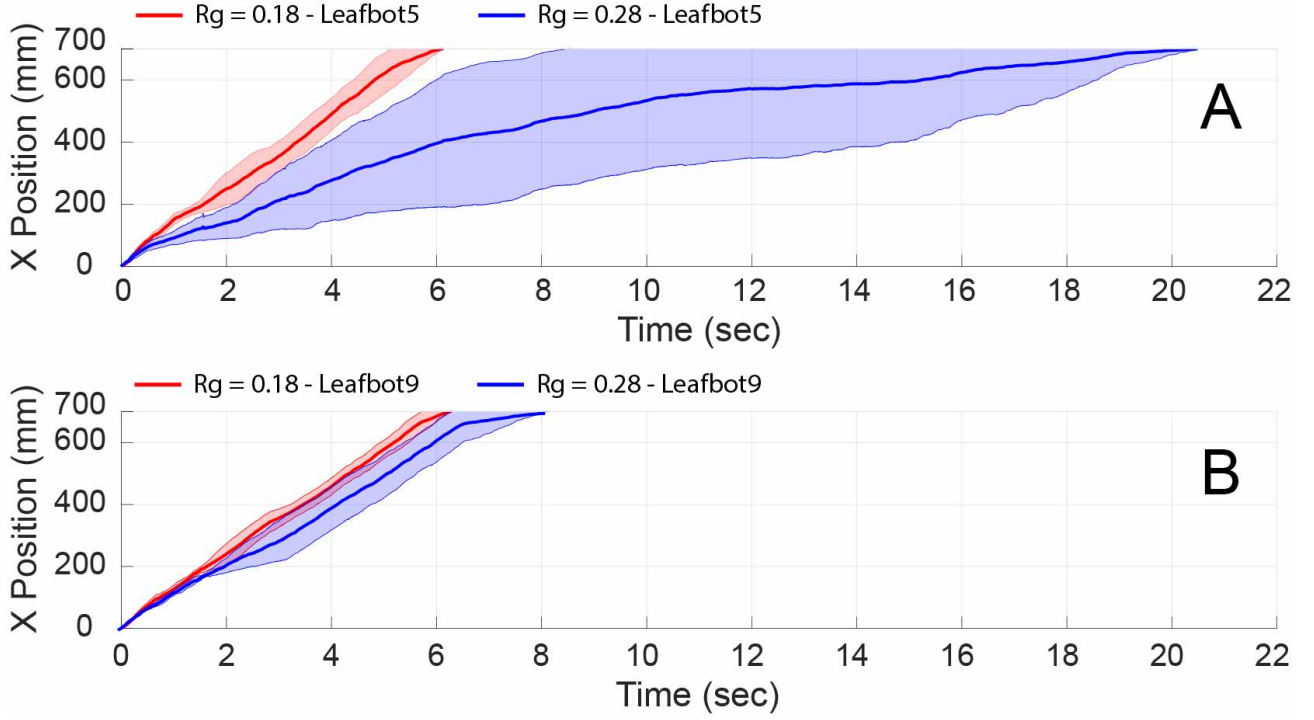


Figure 5.15: The empirical traverse duration of patterns in two rugose terrains,  $R_g = 0.18$  and  $R_g = 0.28$ . (A) the traverse duration of Leafbot5. (B) the traverse duration of Leafbot9. The duration of Leafbot3 does not appear in this figure since Leafbot3 fails to overcome both designed terrains, which means the duration becomes infinite.

were placed consecutively. Two bar graphs in Figure 5.14 stand for the normalized probability density distribution of  $h_t$  in both terrains  $R_g = 0.18$  and  $R_g = 0.28$ . We tested three design patterns in both rugose terrains,  $R_g = 0.18$  and  $R_g = 0.28$ . The robot's motion over the traveling distance of 700 mm was tracked by the OptiTrack system. Because  $h_t$  is automatically determined by MATLAB, we randomly mix these numbers to create three different terrains with each data set of  $h_t$ . The results corresponding to the rugosity study are presented in Figure. 5.15. The mean and the standard deviation (SD) of time of Leafbot5 to complete both rugose terrains are shown in Figure 5.15A, while Figure 5.15B illustrates the performance of Leafbot9. Leafbot3 results do not appear in Figure 5.15 because such a design fails to overcome both rugose terrains, which indicates the traverse duration of Leafbot3 comes to infinite. In the less-rough terrain condition,  $R_g = 0.18$ , the traverse duration of both patterns can be considered roughly similar or obtain similar average velocities. Nevertheless, in rougher terrain,  $R_g = 0.28$ , Leafbot5 takes much longer time to finish the  $L_t = 700$  mm pathway and has a larger SD. In contrast, Leafbot9 performs better, with a shorter traverse duration and a smaller SD. This indicates that Leafbot9's additional limbs enhance traversability in rough terrain conditions.

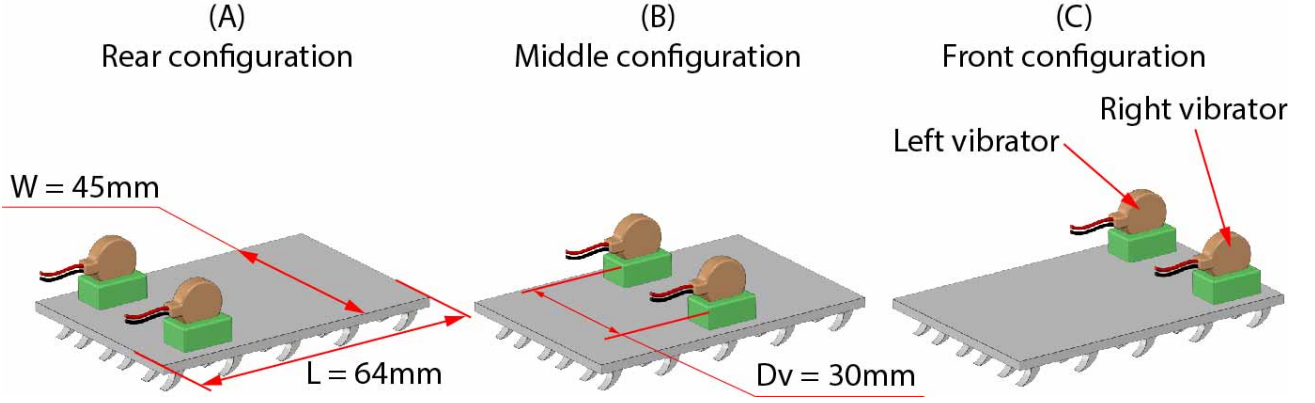


Figure 5.16: The vibrator configurations. (A) Two side vibrators are placed at the rear of the body; (B) Two vibrators are placed in the middle of the body; (C) Two side vibrators are installed at the front. Two vibrators are placed  $D_v = 30\text{ mm}$  apart.

## 5.4 In-plane locomotion verification of *Leafbot*

### 5.4.1 Modified design

Previously, we discussed the straight-line motion of our monolithic soft-body robot. This section presents our evaluation of the robot’s locomotion performance in a 2D planar environment. To achieve this goal, we modified the design by widening the robot body to accommodate more vibration sources. We used an enlarged version of the standard Leafbot, Leafbot5, named Leafbot-X5, which has two vibrators. This modification aims to enhance steering capability through multiple vibration sources, as proven effective in a previous study [36]. We investigated the influence of the vibration on the navigation performance based on the vibrator configurations as presented in Figure 5.16.

### 5.4.2 Experimental setup

We also adopted the motion capture method to track the robot’s trajectories. The HSC recorded the locomotion of the two side vibrators, and the video was processed by the OpenCV package (see Figure 5.17 for the experimental setup). The strategy to maneuver the robot to turn left is to constantly activate the right vibrator and vice versa. The center trajectory is determined from the left and right vibrators’ paths. Three configurations are similarly tested as in other experiments above at three applied voltages: 3V, 4V, and 5V, which generate vibration frequencies of 95 Hz, 115 Hz, and 150 Hz, respectively. Every configuration was examined to turn left five times and turn right five times with each frequency mentioned above. The goal

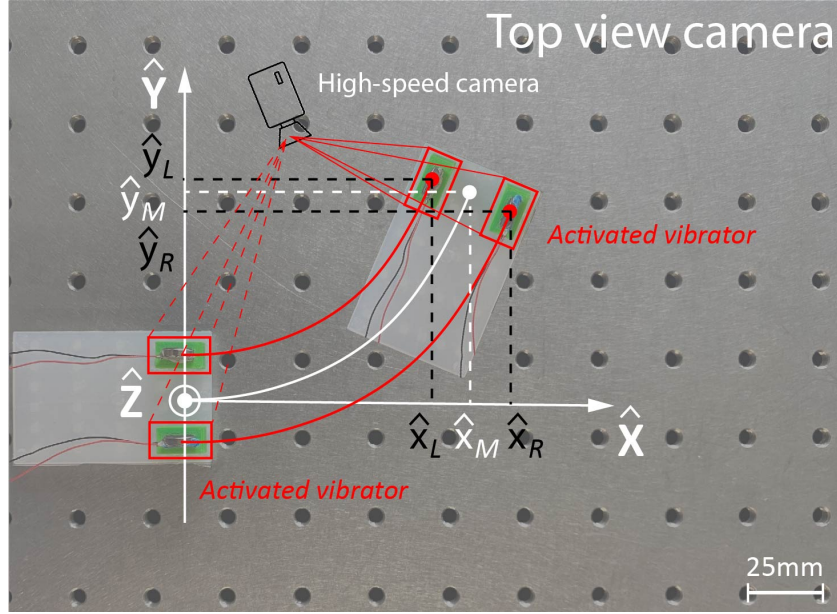


Figure 5.17: The experiment setup to explore the trajectories of Leafbot-X5 in 2D space. The center trajectory, the white line, is determined from the trajectories at both sides of Leafbot.

is to discover the behavior of each configuration to the navigation capability. The vibration was applied for two seconds in each experiment. Apart from evaluating steering capability, straight-line locomotion was also assessed. The strategy to manipulate Leafbot-X5 into moving straight is to activate both side vibrators simultaneously. They were applied for 3V - 95 Hz constantly for three seconds. The capability of moving in a straight line of Leafbot-X5 is shown in Figure 5.19.

### 5.4.3 Outcomes

Figure 5.18 exhibits the steering capability of three configurations at 95 Hz, 115 Hz, and 150 Hz. We determined the average curvatures,  $K_s$  ( $\text{mm}^{-1}$ ), from  $X$  and  $Y$  position data to evaluate steering performance. Table 5.1 presents the attained average curvatures. All configurations can navigate in 2D space, but the middle design consistently offers the best steering performance at all frequencies, with uniform steering for both directions. The front and rear designs of Leafbot-X5 only perform the steering similarly in both directions at 95 Hz; at 115 Hz and 150 Hz, the errors of  $K_s$  between both directions are generated more. Four key factors influence the uneven navigation of the front and rear configurations, especially at high frequencies:

- The inconsistent quality between vibration motors leads to the difference in vibration frequencies and the centripetal force, even at the same applied voltage.

- The inevitable effect of the vibration from the motor tethers.
- The placement of vibration motors affects the moment of inertia.
- Friction variability due to inconsistent limb quality. Our fabrication method poses challenges that prevent well-formed circular limb shapes.

These factors contribute to the asymmetric steering performance of Leafbot-X5. The middle configuration, with vibrators aligned at the center of mass (the least moment-of-inertia location), experiences less impact from these factors, resulting in better steering performance.

Figure 5.19 indicates that all configurations of Leafbot-X5 are possible to obtain straight-line locomotion in 2D space. However, due to unavoidable factors, Leafbot-X5 still experiences perpendicular displacement from the forward direction after three seconds. This suggests that maintaining a straight-line motion over long durations may be challenging. To reduce this displacement, we propose supplying voltage intermittently rather than continuously and using feedback control systems to mitigate errors. In addition, when different vibration frequencies are applied to both vibrators, Leafbot-X5 tends to turn toward the weaker frequency.

In conclusion, we demonstrate the capability of steering in 2D space of Leafbot-X5 design concept. However, we do not construct the analytical model in this scenario due to the complex phenomena induced by vibration systems and the four major factors presented above. This will be addressed in future work.

Table 5.1: The average curvatures,  $K_s$  ( $mm^{-1}$ ), derived from the obtained data set of the tracking position in  $X$  and  $Y$  direction.

Vibration freq.	Steering dir.	Configuration		
		Rear	Middle	Front
3V - 95 Hz	Left	0.015	0.014	0.018
	Right	0.015	0.014	0.017
4V - 115 Hz	Left	0.009	0.015	0.016
	Right	0.013	0.014	0.010
5V - 150 Hz	Left	0.008	0.015	0.015
	Right	0.004	0.017	0.008

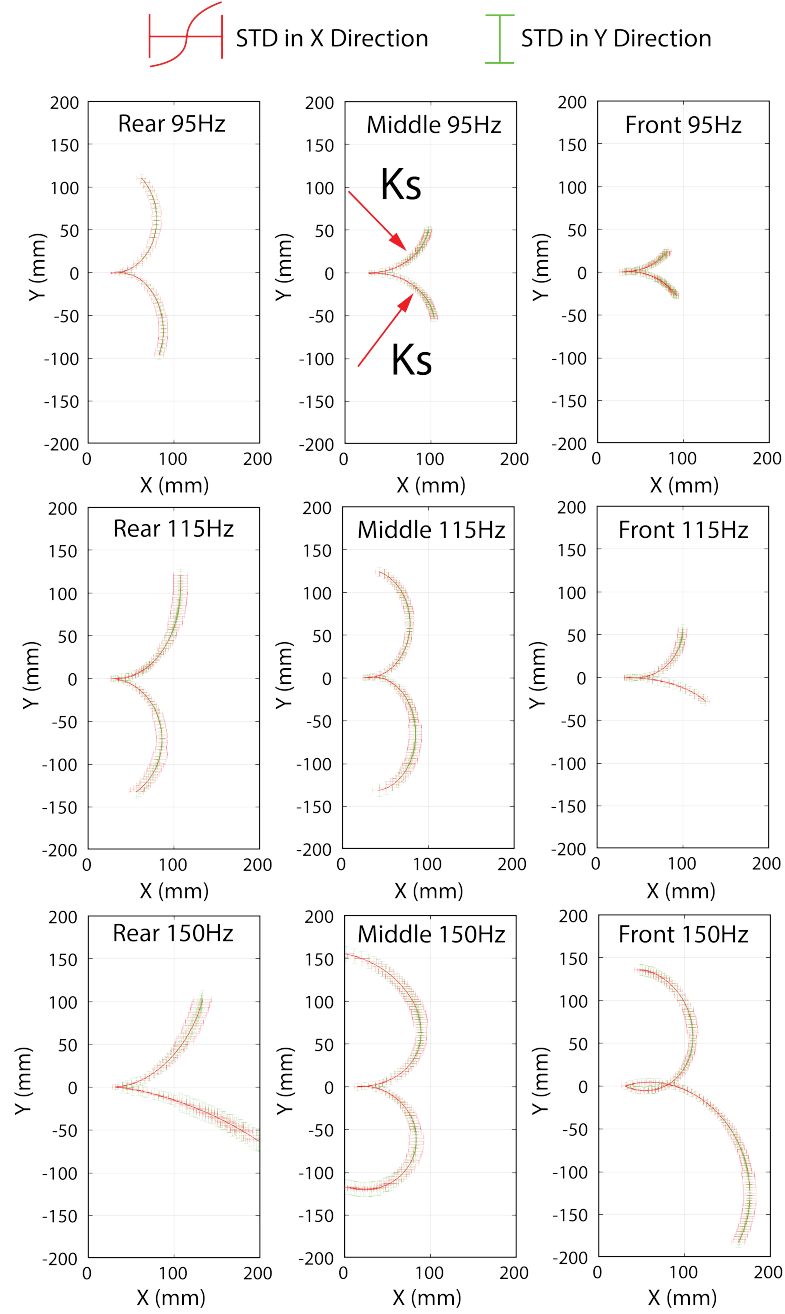


Figure 5.18: The navigation performance of Leafbot-X5's configurations when equipped with two side vibrators at different vibration frequencies. The duration of the applying vibration to the driven vibrator was two seconds in every experiment.

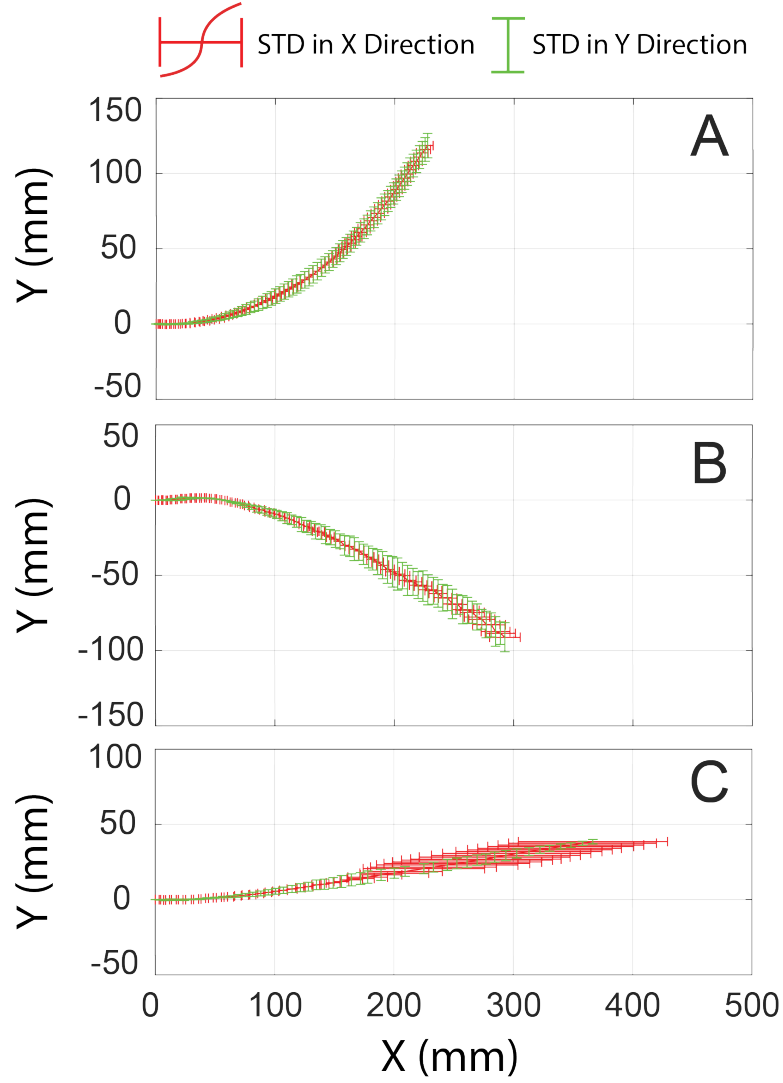


Figure 5.19: The performance of Leafbot-X5 in delivering the straight-line locomotion by simultaneously activating two side vibrators at 3V in three seconds (the correspondingly induced frequency is 95Hz). (A), (B), (C) The trace of Front, Middle, and Rear configuration, respectively.





## Chapter 6

# Showcase of Vibration-driven Design in Constrained Cavity Conditions: *PufferFace Robot* - *PFR*

### 6.1 Experimental scheme for PFR locomotion verification in the horizontal condition

In the above sections, we present the explanations for the locomotion modes. Mode 3 is the primary mode that delivers the forward motion of PFR in cavities. Hence, we focused on investigating the motion performance of PFR when Mode 3 was being activated. The experimental parameters were applied analogously to the propulsion force test, including testing in three boundary conditions, *i.e.*, 30-mm, 36-mm, and 41-mm pipes; four vibration frequencies: 64 Hz, 137 Hz, 160 Hz, and 192 Hz; three levels of input pressure: 20 kPa, 23 kPa, and 26 kPa. The measurement scheme is shown in Figure 6.1. To observe the  $X$  position of PFR corresponding to the applying pressure, we connected the programmable air pump, a 5 Degree Of Freedom (DOF) electromagnetic tracking (EM) sensor (Aurora 5 DOF Sensor Northern Digital Inc., Canada), and a micro-controller, an Arduino UNO board, to the Robot Operating System (ROS) environment installed on an external computer. The utilized EM sensor is small, compact, and lightweight (the size of the sensor tip - 0.3×2.5 mm). The sensor tether was small, tiny in diameter, and had highly bendable and flexible properties. Such features allowed us to eliminate the influence of the sensor mass on displacement outcome and diminish the induced friction force acting on the sensor tether. ROS enabled us to collect the sensing data together with the pressure data in real-time.

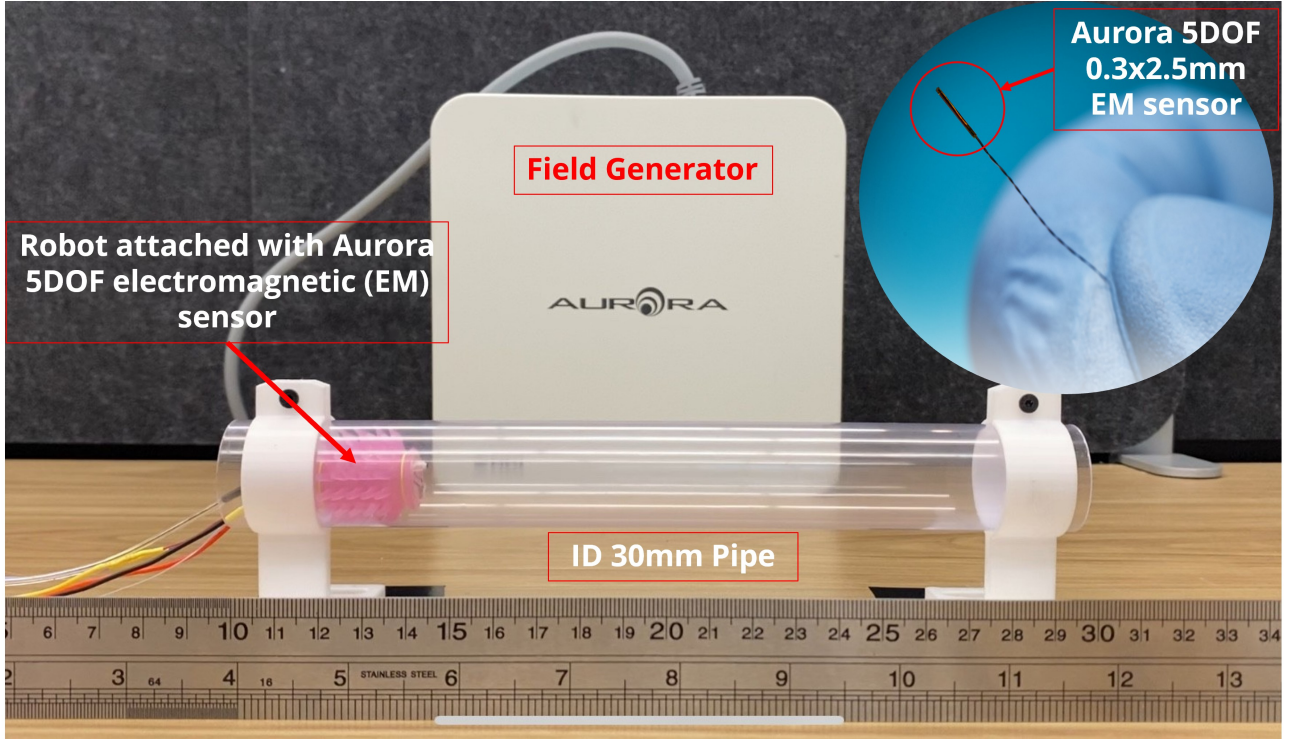


Figure 6.1: The experimental scheme to measure the displacement of PFR over time in the horizontal condition.

## 6.2 Constructing the Finite Element Analysis (FEA) simulation model of PFR

Although analytical models for vibration-driven robots in tubular conditions were developed in prior studies, these frameworks can be merely applied to robots with fixed sizes, whereas our proposed design can flexibly vary the dimension of the PFR's body to adapt to the variable cavities. Additionally, the inflation/deflation mechanism in Mode 3 of locomotion (see Figure 4.6) primarily yields the forward motion of PFR. However, this entire process over one cycle of pressure activation is complicated; thus, we decided to simulate the locomotion of PFR by adopting the FEA simulation model, which is a reasonable selection for solving complex models. To address this problem, we proceeded with the dynamics analysis in a similar way to the characterization of the inflation radius. The Dynamic Explicit module of ABAQUS was utilized for this task. In the FEA-based simulation, the soft skin with spikes was characterized by the Yeoh model, known for accurately modeling hyperelastic material deformation [91]. Instead of using a full 3D model of PFR, we simplified it into a 2D model for three reasons. The first reason relates to the generated mesh at the tips of the soft spikes. It was reported that the simulation program could not be completed due to failures originating from the generated

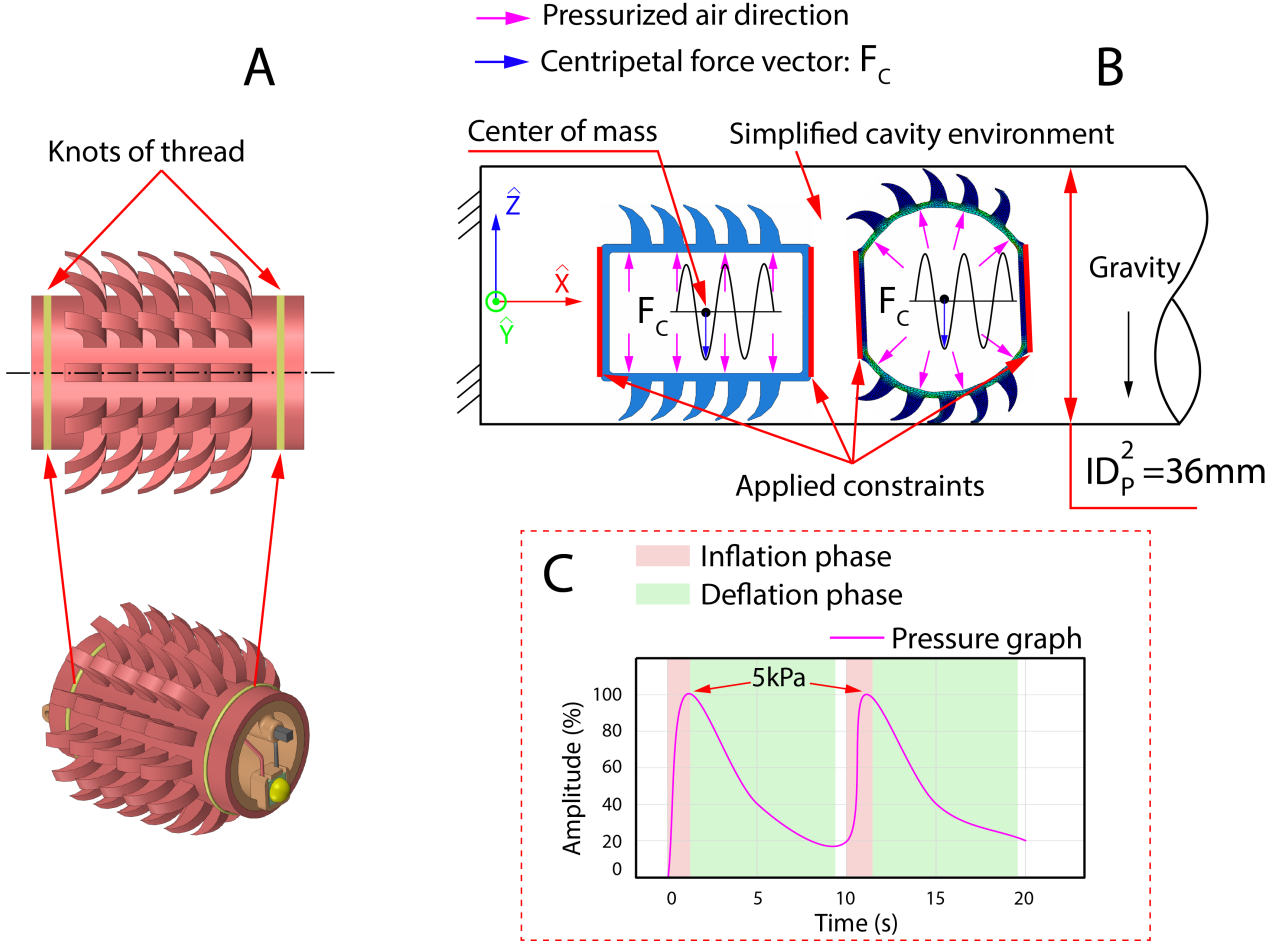


Figure 6.2: FEM simulation procedure with ABAQUS. (A) The removal of unnecessary parts for the simulation. (B) The simplified model of the cavity and the soft skin of PFR. How physical factors, including sinusoidal centripetal force  $F_C$  and pressurized air, come into play in the model. (C) The characterization of the inflation and deflation phases.

mesh at the spikes. However, if we convert to the 2D structure of PFR, less mesh is generated. Consequently, we rarely encounter failure in the simulation. The primary reason for this failure is the limitation of the computer's computational capacity. During a simulation task, if a simulation generates too many elements for the computer to process effectively, errors can accumulate during deformation, causing some elements not to be restored correctly and leading to mesh distortion. By simplifying a 3D model to a 2D simulation, the computational load is reduced, enhancing the stability of the simulation model. The second reason is to reduce the computational cost. It takes us up to 72 hours to complete a simulation for the 3D model, while the 2D model can complete one simulation in 15 minutes with the same simulated condition. The last is that the outcomes of the 2D simulation still reflect the actual feature of the vibration-based locomotion and match the displacement results from the empirical method. Thanks to the cylindrical structure of PFR, as well as the pipeline, these conditions allowed us to replace

the symmetric 3D frame with a 2D cross-section of both PFR and the flow channel of the working environment. Hence, the simplification still represents the nature of the simulation of PFR in actual working conditions. The simplified procedure of the simulation proceeds as follows.

In the first step, we reconstructed the cavity environment by using the Wire Model to represent the 3D symmetric structure of the tube by two solid lines. The distance between the two lines is similar to the diameter of the pipe. Subsequently, the PFR's design is likewise symmetric; thus, it could be equivalently converted from the 3D to 2D model. To obtain the most simplified model, the parts, including the DC vibrator, the hollow frame, the LED, the camera, the air inlet, and the motor tethers, are all omitted. These components are represented by one node with mass, which is placed at the center of the mass of the 2D model of PFR and influenced by gravity. Figure 6.2 demonstrates the simplified simulation model on Abaqus. Figure 6.2A shows the removal of unnecessary parts for the simulation. The regions of the soft skin that are taken into account in the simulation are between two knots. Figure 6.2B exhibits the simplified model of the cavity and the soft skin of PFR. Because inflation only occurs at the soft skin regions limited between two knots, we applied the constraints at both ends of the soft skin. Thus, the deformation would not happen at the front and the rear. The pink arrows stand for the pressurized air that causes the skin to inflate. Based on the mechanism of Mode 3, we likewise specified the input pressure graph in the simulation as the pressure behavior in the experiment. Figure 6.2C presents the pressure curves that we characterized in the Abaqus model. Keep in mind that because this is the 2D simplified model, the simulated pressure differs from the actual one. Therefore, it is essential to determine the proper values in the 2D model that correspond to the utilizing values of pressure in the experiment. In this case, since we were focusing on simulating the performance of PFR at 23 kPa, the corresponding value in the 2D model is 5 kPa. This equivalent pressure value in the 2D model was chosen because we observed that at 23 kPa in the 3D environment, all spikes from  $j_2$  to  $j_4$  would contact the pipe wall. Therefore, a pressure of 5 kPa was selected in the 2D model to achieve the same spike contact behavior.

Regarding the centripetal force,  $\mathbf{F}_C$ , it is required to input the frequency and the amplitude of the oscillation.  $\mathbf{F}_C$  is placed at the center of the mass of the model because the vibration affects similarly to every point of the frame. In addition, we followed the procedure below to obtain the simplified values of centripetal force for the 2D simulation tasks. Firstly, we

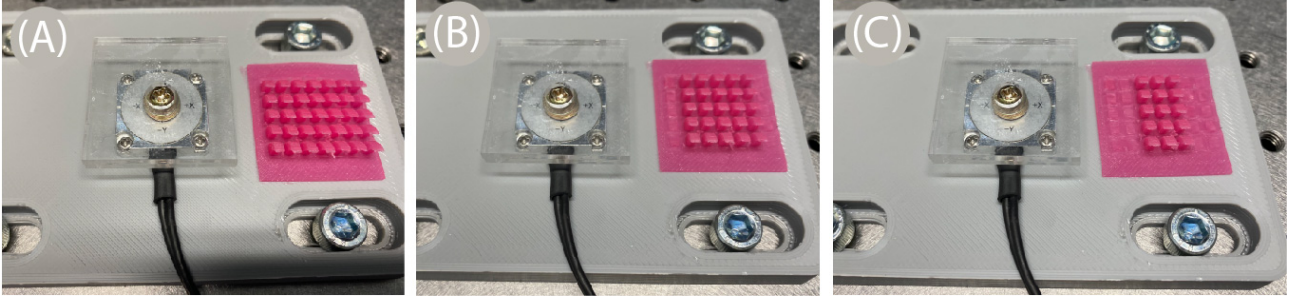


Figure 6.3: Prepared samples to measure the stiffness behaviors of three patterns of soft spikes. (A) A  $7 \times 5$  pattern sample ( $i_1$  to  $i_7$ ;  $j_1$  to  $j_5$ ). (B)  $5 \times 5$  pattern sample ( $i_1$  to  $i_5$ ;  $j_1$  to  $j_5$ ). (C)  $3 \times 5$  pattern sample ( $i_1$  to  $i_3$ ;  $j_1$  to  $j_5$ ).

determined the stiffness behaviors of the soft limb patterns in three cases with different ranges of  $i$ . The 1st case, from  $i_1$  to  $i_7$ ; the 2nd case, from  $i_1$  to  $i_5$ , and the 3rd case, from  $i_1$  to  $i_3$ . Note that because PFR's structure is symmetric, we only considered one-half of the PFR body. Subsequently, we employed a 3-axis sensor, resolution 0.001N, to measure the stiffness of these soft spike patterns (Dragon Skin 10 material). Figure 6.3 presents the experimental samples. We carried out the testing procedure similarly to those in Figure 3.5. The results are displayed in Figure 6.4. These results indicate that stiffness can be linearly scaled with the number of spikes. Since the generated centripetal force at the maximum tested frequency of 192 Hz was minimal, the relationship between the normal force and deformation was also considered linear. Therefore, the scaled centripetal force in the 2D environment was conducted based on this method. Table 6.1 exhibits the input data of  $\mathbf{F}_C$  amplitude and frequency.

Table 6.1: The vibration frequencies and the corresponding amplitudes of the sinusoidal signals of the centripetal force.

Vibration frequency (Hz)	64	137	160	192
Amplitude (N)	0.0008	0.004	0.0054	0.0077

## 6.3 Experiment and FEA simulation outcomes in horizontal pipes

### 6.3.1 Experimental results

Figure 6.5 depicts the collected results of the horizontal displacement of PFR. In order to plot a position line with a shaded area, three standard deviations area -  $3 \times \text{SD}$ , we repeated each experiment three times on each pair of pressures and vibration frequencies. In general,

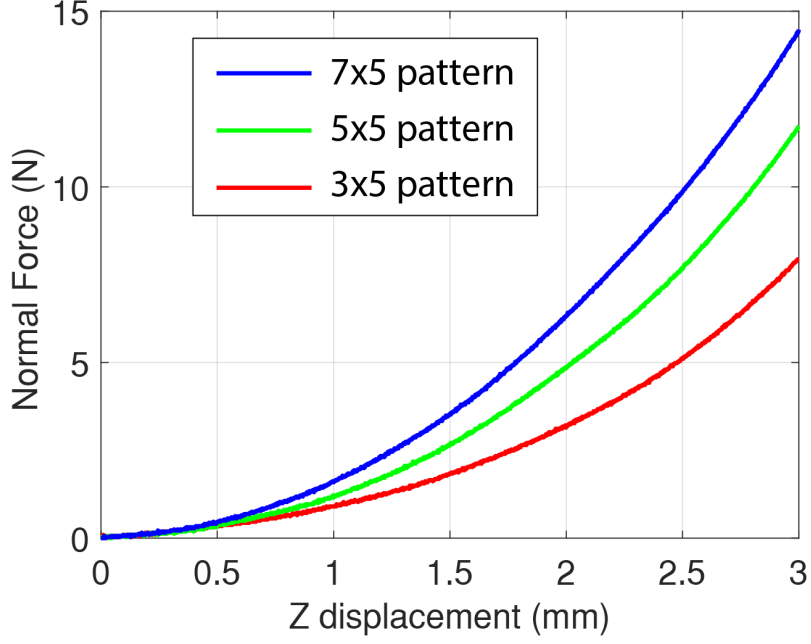


Figure 6.4: The stiffness behaviors of three patterns, *i.e.*,  $3 \times 5$ ,  $5 \times 5$ , and  $7 \times 5$  soft spike patterns.

Figure 6.5 demonstrated that the higher the vibration frequency is applied, the higher the displacement is generated in Mode 3. At the lowest tested frequency (*i.e.*, 64 Hz), PFR barely moves even though this frequency brings the highest velocity in Mode 1 of locomotion. In contrast, the average velocity at 192 Hz appears in the lower-than 5 mm/s zone in Mode 1 but gains the highest displacement values in Mode 3. Movements in Mode 3 have the same behaviors that always occur during the deflation phase. The locomotion of PFR can only be achieved within a specific pressure range, from  $P_{M3}^B$  to  $P_{M3}^S$ , of the deflation phase. The displacements in the 36-mm and 41-mm circumstances demonstrate better results than the 30-mm cases in terms of achieving displacement over one applied pressure cycle. This response comes from the average deflation rate,  $Df_r^a$ . As demonstrated in Figure 4.12, in spaces whose cross sections are as approximately small as PFR size, PFR faces difficulty in retaining the curvy shape due to the restriction of the boundary; consequently, more soft spikes come into contact with the pipe wall, yielding more compression force on the soft skin. Thereby, the soft skin more rapidly shrinks in the deflation phase, leading to the reduction of the deflation spans. In the 36 mm and 41 mm pipes, there is more space for PFR to acquire the curved shape, so there are fewer soft limbs contacting the boundary wall (see Figure 4.12). Hence, the deflation phase lasts longer in those contexts in exchange for more induced displacement.

In addition, it can be noticed in the pressure curves of Figure 6.5, especially the regions in



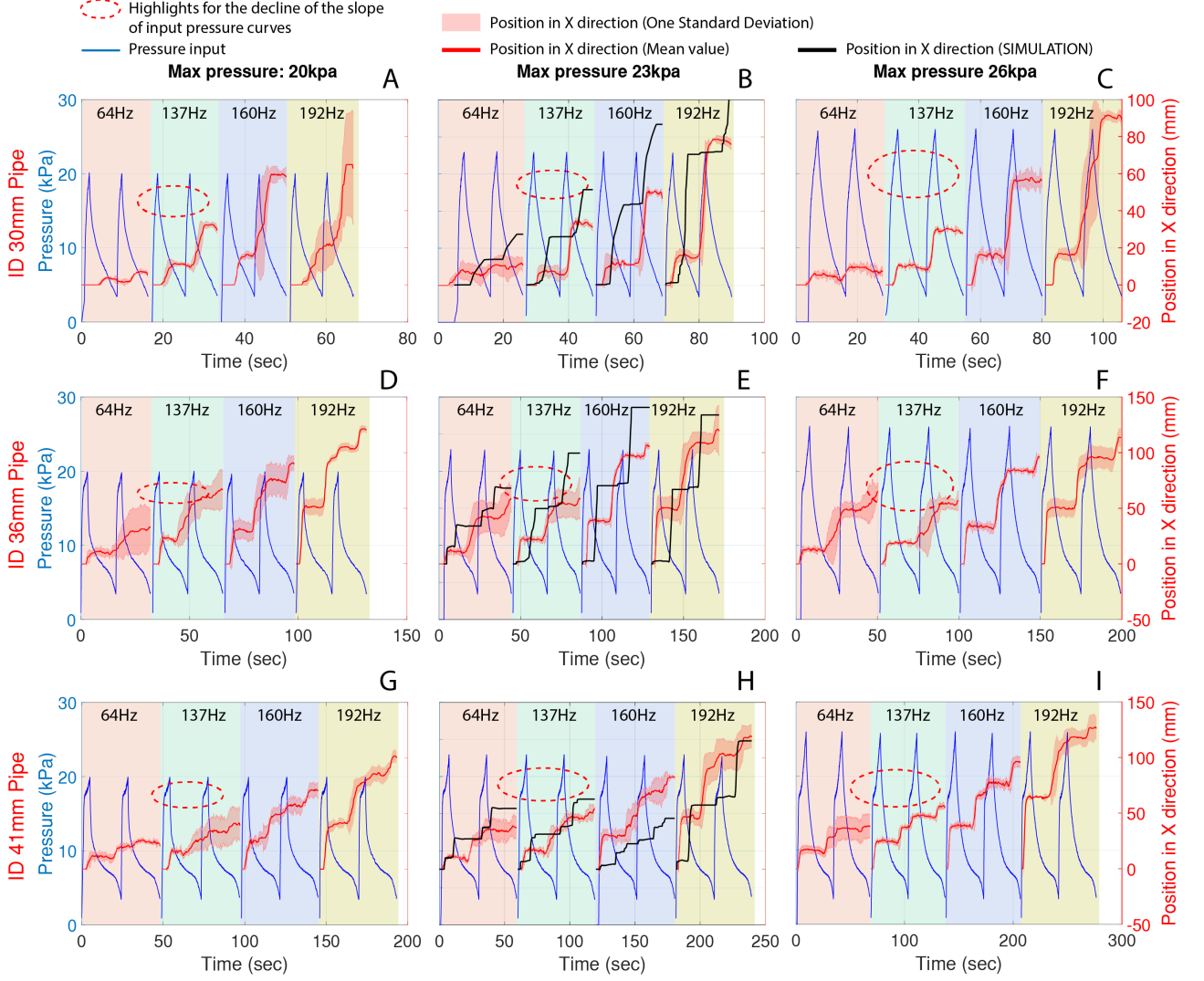


Figure 6.5: The PFR's position data in X direction was collected when testing in  $ID_P^1 = 30$  mm,  $ID_P^2 = 36$  mm and  $ID_P^3 = 41$  mm pipes in the aforementioned pre-setting conditions. (A, D, G), (B, E, H), (C, F, I) illustrate the results in the cases of applying pressures 20 kpa, 23 kpa, and 26 kpa, respectively.

the red dash ovals, that the appearances of the pressure curves differ from pipe sizes. When the diameter increases, the growth of the pressure in the inflation phase exhibits the same transformations that the slopes of the pressure curves suddenly decrease at the tip regions of the curves. The bigger the pipe, the more the slope declines. From these characteristics of the pressure behaviors, PFR can actively detect the change in the dimension of the interacting cavity environment, *i.e.*, in complicated pipeline networks, where operators cannot determine the variation of the tubular dimension. Besides, these displacement performances reveal the best pair of values, applied pressure:  $P_{M3} = 23$  kPa and vibration frequency  $f = 192$  Hz so that they allow PFR to travel through all testing cavity conditions. Although these performances do not dominate the locomotion speed compared to most other developed terrestrial soft designs [9],



the locomotion mechanism of PFR demonstrates an effective way of controlling. The induced displacement outcomes reveal a template that PFR is able to traverse through any pipeline systems with diameter sizes varying from 1 to 1.5 times the outer diameter of PFR by a simple form of controlling method.

### 6.3.2 FEA simulation results in ABAQUS

Based on the acquired position dataset, we decided only to take the best-determined input parameters, *i.e.*, 23 kPa, and 192 Hz, for the simulation model. The simulation to investigate the displacements of PFR in the horizontal case in the ABAQUS environment was followed by the procedure presented in Figure 6.2A. The obtained simulated data of PFR are plotted to be associated with the empirical results in Figure 6.5, the black lines.

Firstly, although the simulation is simplified into the 2D model, the response of the simulation well reflects the basis of Mode 3 locomotion in two points: the standstill phase occurs when input pressure is higher than  $P_{M3}^B$  value, and motion begins when the pressure drops below  $P_{M3}^B$  value and then stops when the pressure falls below  $P_{M3}^S$ . Secondly, the generated displacements over one cycle of applying pressure quite match the experimental values. Although there are discrepancies between the simulation and the experiment outcomes, these differences can be attributed to the friction between the tethers and the tube wall and the tethers' vibration, which regularly caused the entanglement between the wires and the tube edge. However, these barriers can be handled by applying a cable deployment mechanism. With these simulated results, we conclude that our proposed simplified FEM simulation model is reliable and acceptable. First, it correctly reflected the locomotion mechanism of PFR when it is activated simultaneously with pressurized air and vibration frequency. Second, the simulated position data over time is nearly aligned with the experimental data. The errors of the maximum displacements between the simulation and experiment after two cycles of air activation are not substantial.

## 6.4 Investigate the influence of $Df_r^a$ and $P_{M3}^S$ to locomotion performance in horizontal and vertical conditions

The aforementioned outcomes show how PFR locomotion performs in different scenarios of pressure values, vibration frequencies, and pipe sizes, the results also indicate the best pair of

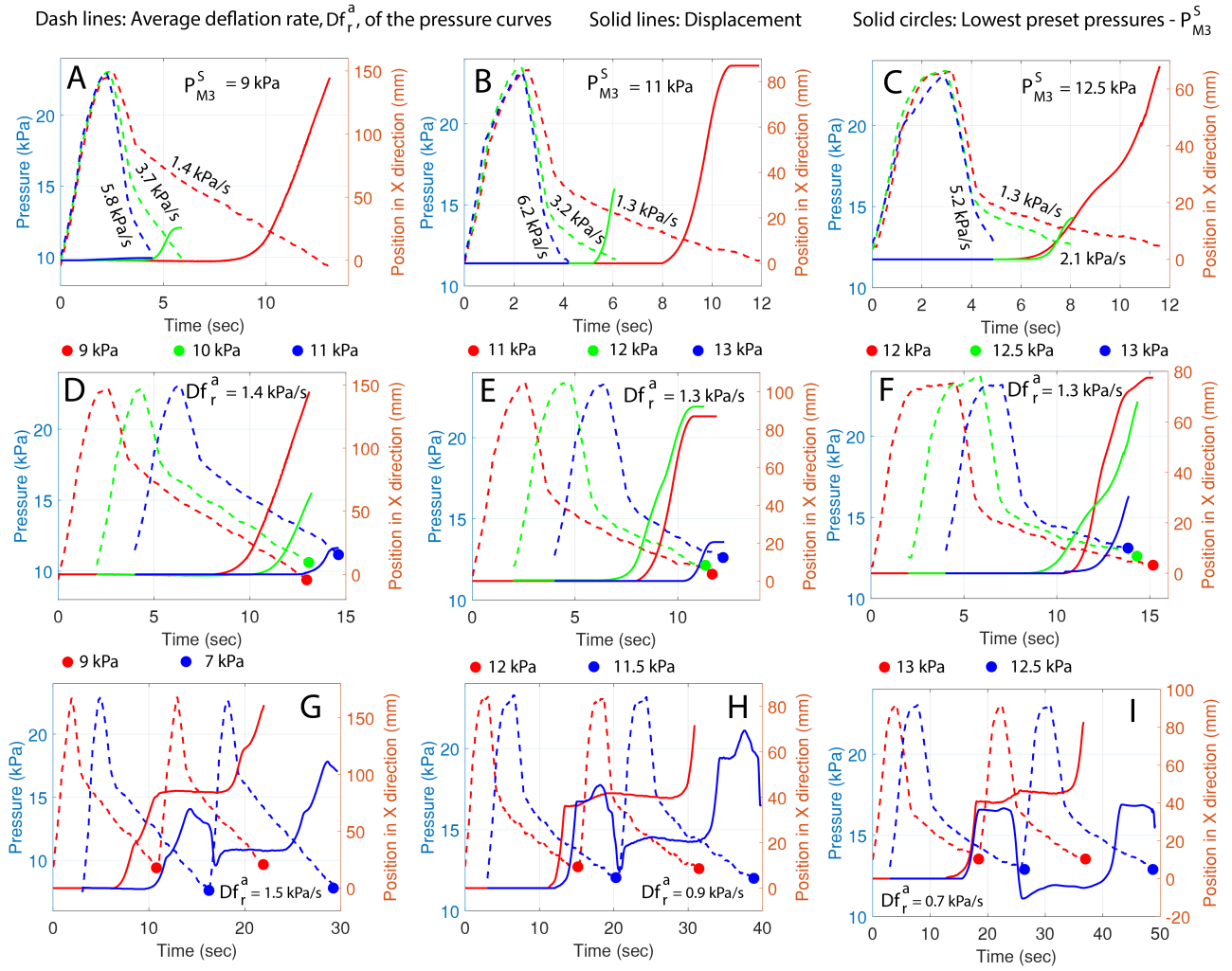


Figure 6.6: The displacement behaviors vary according to different average deflation rates,  $Df_r^a$ , and the lowest threshold pressure,  $P_{M3}^S$ . (A, B, C) the displacement behavior varies according to the average deflation rate,  $Df_r^a$ , in the 30-mm, 36-mm, and 41-mm cases, respectively. (D, E, F) the displacement behavior varies according to the lowest threshold pressure,  $P_{M3}^S$ , in the 30-mm, 36-mm, and 41-mm cases, respectively. (G, H, I) The variations of displacement in the 30-mm, 36-mm, and 41-mm vertical pipes correspond to the thresholds of  $P_{M3}^S$ , *i.e.*, 9 kPa, 12 kPa, 13 kPa, respectively.

oscillation frequency and maximum pressure values, *i.e.*, 23 kPa and 192 Hz. This experimental data is still concerned with how displacement would vary if the average deflation rate,  $Df_r^a$ , were kept consistent. The pressure curves in Figure 6.5 were generated by allowing the compressed air inside the soft skin to deflate naturally, resulting in differing behavior of the curves. Thus, to address this question, we conducted additional experiments to assess displacement behaviors under the same average deflation rate. Based on the results in Figure 6.5, we selected the maximum applied pressure and the vibration frequency at 23 kPa and 192 Hz for the following experiment.

Figure 6.6 exhibits the behaviors of PFR displacement according to two pressure variables, including the average deflation rate,  $Df_r^a$ , and the minimum threshold pressure,  $P_{M3}^S$ . The dotted line represents the air pressure inside the soft skin, while the solid line represents the distance the robot moved inside the pipe. The slope of the solid line indicates the robot's moving speed. The experimental outcomes in Figure 6.6A, B, C suggest that at  $Df_r^a$  approximately 1.3 kPa/s, PFR can obtain the farthest distance in one pressure cycle. In contrast to the performance in Figure 6.5, where the deflation mechanism is not specified, the PFR displacement in the 30-mm pipe is greater than in the 36-mm and 41-mm pipes. This is because the lower deflation speed allows the soft spikes to maintain contact with the pipe for a longer duration. The distance traveled in a single pressure cycle decreases as the deflation speed increases, and if the pressure drops faster than roughly 6 kPa/s, the forward motion may come to a complete halt. Besides, note that in Figure 6.6A, B, C, the  $P_{M3}^S$  values represent the minimum pressure at which the pattern of the spikes barely touches the tubular wall.

As described, the pressure curve is characterized by three variables, *i.e.*, the maximum pressure value, the average deflation rate,  $Df_r^a$ , and the minimum threshold pressure,  $P_{M3}^S$ . We clarified the influences of the highest pressure and the  $Df_r^a$  to the motion capability. Now, we investigate the effects of the lowest pressure,  $P_{M3}^S$ , in which the forward motion is achievable. This value is specified beforehand in the closed-loop pressure control device. Figure 6.6D, E, F indicate the displacement results at various preset values of  $P_{M3}^S$  (note that these experiments proceeded with the best deflation speed  $Df_r^a \approx 1.3$  kPa/s). These graphs highlight the importance of the pressure curve. If  $P_{M3}^S$  is set too high, causing the soft spikes to remain heavily compressed. Therefore, there is less opportunity for the stick-slip mechanism to occur, limiting the generation of locomotion. In contrast, in vertical cases, the robot will fall off if it cannot retain sufficient pressure to anchor itself securely to the wall. Therefore, the role of  $P_{M3}^S$  is vital in vertical conditions. Further, additional experiments were conducted to identify the proper thresholds, ensuring upward motion while preventing the robot from losing height when the pressure drops below certain limits. Figure 6.6G, H, I displays the minimum values of  $P_{M3}^S$  at which upward motion is sustained without the robot falling.

Finally, we assessed the average locomotion speed of the PFR at different pipe inclination angles. Using the most effective parameters characterizing the pressure curve (*i.e.*, maximum pressure, average deflation rate,  $Df_r^a$ , and the minimum threshold pressures,  $P_{M3}^S$ ), we examined the motion speed, which can be later used to assess robot's performance in terms of its relative

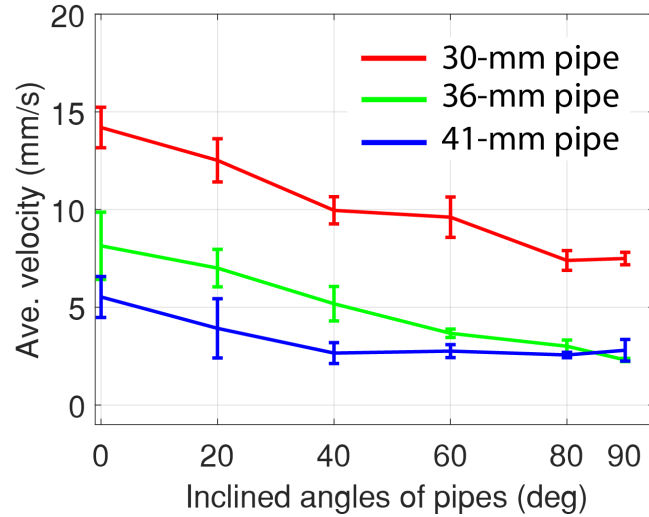


Figure 6.7: The average locomotion speed of PFR in different inclined angles of pipe configurations

speed versus its body length (Body Length/second - BL/s) compared with other similar robots. Table 6.2 presents the utilized parameters for the average velocity experiment. Also, Figure 6.7 illustrates the average speed performance of PFR in three cavity environments, *i.e.*, the 30-mm, 36-mm, and 41-mm pipes.

Table 6.2: The parameters applied to PFR to examine the average locomotion speed at different pipe inclination angles.

Pipe sizes	The most effective parameters			
	Max pressure (kPa)	$Df_r^a$ (kPa/s)	$P_{M3}^S$ (kPa)	Vibration frequency (Hz)
30mm	23	1.4	9	192
36mm	23	1.3	11	192
41mm	23	1.3	12.5	192

## 6.5 Estimate the maximum traveling distance in certain circumstances

Considering practical applications, the maximum traveling distance capability of the PFR was indirectly analyzed through additional experiments. The outcomes from the propulsion force experiment suggested that the robot can obtain a long travel distance relative to its body length. Thus, it is rather challenging to set up a long pipeline to verify the longest achievable traveling distance. We only focus on examining the traveling distance in the straight pipe placed horizontally and vertically. In the vertical condition, the traveling distance is merely

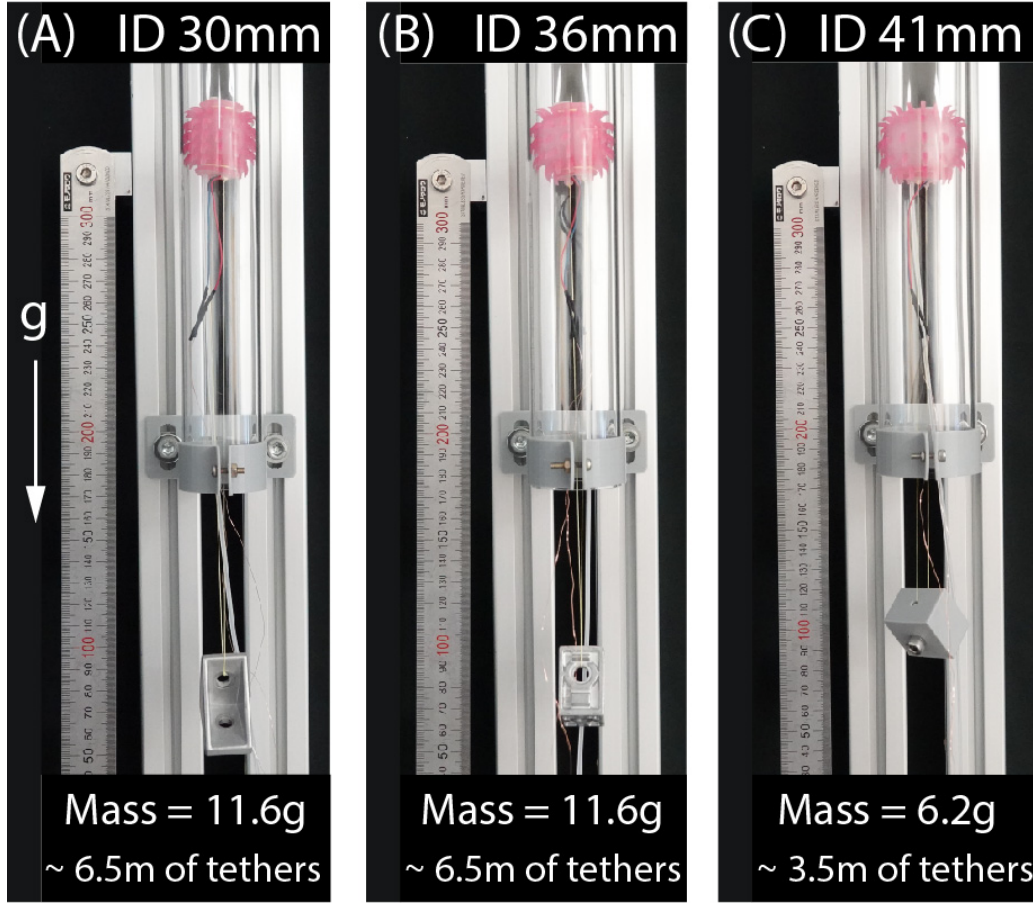


Figure 6.8: The experimental set-up to indirectly evaluate the maximum traveling distances. (A), (B), (C) PFR carries extra mass and the equivalent length of tethers in the 30-mm, 36-mm, and 41-mm pipes, respectively.

influenced by the mass of the tethers, including the motor wires and the air supply tether, which are the required components to generate the locomotion. We did not consider the influence of the camera and the LED tether because we are still facing difficulties in lessening these masses; however, we suppose that there should be a solution to minimize the mass of these additional devices. Figure 6.8 shows the experimental outcome of the maximum extra masses equivalent to the length of the tether that the robot can carry in vertical conditions. These results indicate the maximum traveling distance of the robot traveling vertically in three pipe sizes. In horizontal conditions, the traveling distance is higher than or equal to the distance of the vertical case because it is only influenced by the tether's friction. We also tested the static friction coefficient of one meter of the air supply tether (a polyurethane tube, TU0212C-20 SMC) with the acrylic pipe. The static friction coefficient result varies from 0.5 to 0.75. This outcome suggests that the robot might travel a distance of 1.3 to 2 times the distance of the vertical cases. The experiments estimated that the PFR could horizontally travel a maximum

distance of approximately 8.45 m - 13 m with the 30-mm and 36-mm pipes and 4.5 m - 7 m with the 41-mm pipe. The average velocity remarkably drops in these contexts. If the mass of the camera and electrical wires connected to the robot can be further reduced in the future, the maximum traveling distance is expected to improve. However, the maximum traveling distance may vary depending on changes in the environment in which the robot operates.

## 6.6 Terradynamics study of PFR through critical and hybrid conditions of a pipeline system by empirical and experimental approaches

In the above sections, the research presents the locomotion investigation of PFR by both the experiment and simulation model in regular conditions, such as straight pipes. Nonetheless, inspection robots might encounter more complicated scenarios when being deployed to actual pipeline systems. In Section 5.3, this work shows the terradynamics study of Leafbot designs. This approach clarified the traversability of Leafbot's patterns with predetermined terrains. Although terradynamics studies have been merely investigated in planar contexts thus far, this framework has appeared to be very useful in assessing the traversal ability of robots with complex environments. Hence, within this dissertation, we extended the scope of terradynamics to cavity scenarios, aiming to develop a comprehensive assessment method for robots operating in variable environments.

To investigate the terradynamics features of PFR in hollow-constrained environments, we challenged PFR's capability of traversing through critical zones of any pipeline system, including **the elbow turning sections – high curvature sections, branches, traveling horizontally to vertically transition areas from small to big cavity and vice versa in both horizontal and vertical conditions, and the steering ability when dealing with T-shaped pipe** [44].

Because PFR features adaptive morphology, which can advance its traversability through various constrained situations in cavities without requiring complex controlling algorithms, the Mode 3 strategy of locomotion was adopted to evaluate PFR's adaptability to critical sections in a pipeline. The applied vibration frequency and the maximum supplying pressure are 192 Hz and 23 kPa. These tasks were initially simulated by the Dynamic Explicit module in ABAQUS, then justified by experiment. Figure 6.9 presents the performance of PFR in those conditions.



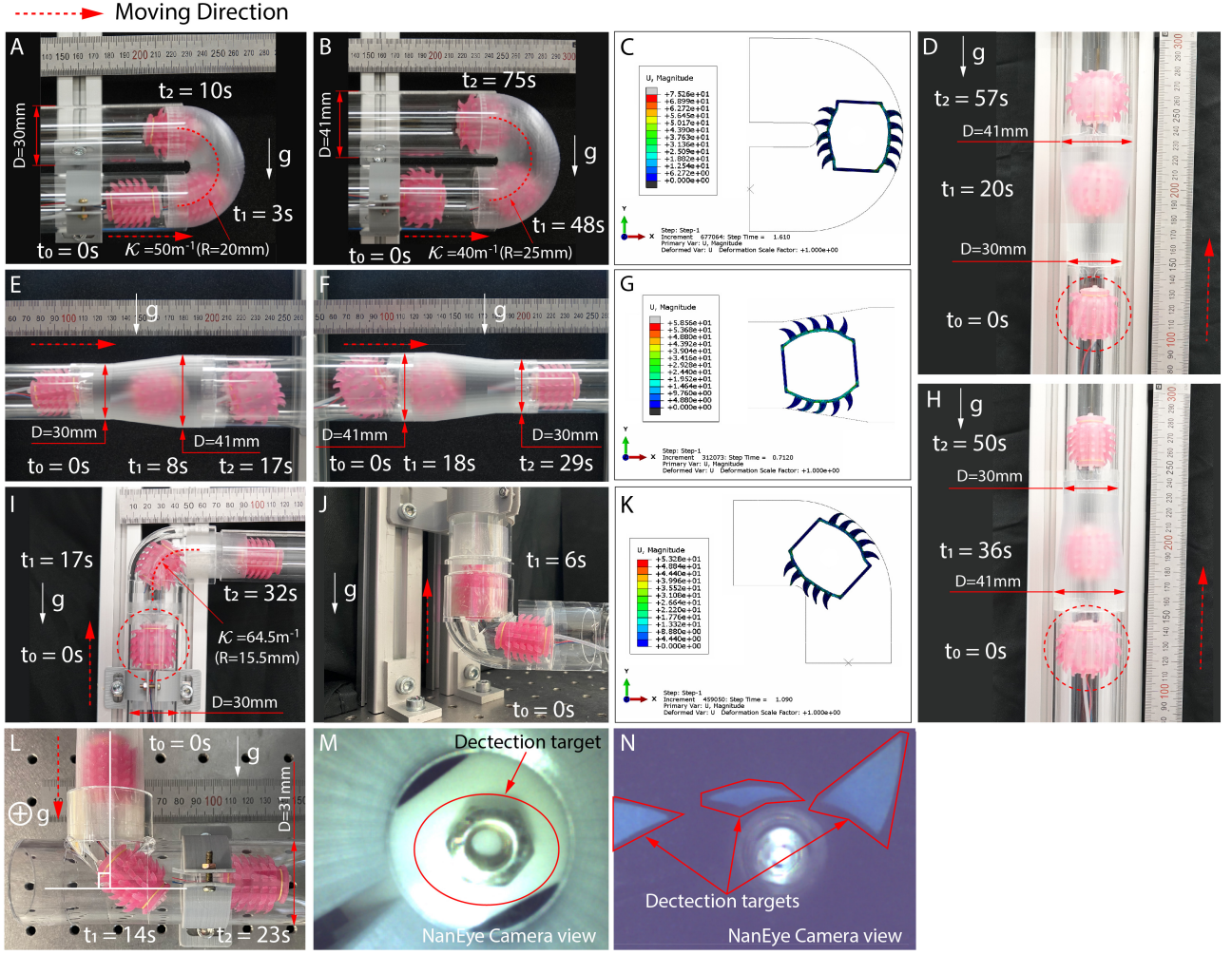


Figure 6.9: The evaluation of PFR performance when coping with critical zones in pipeline systems by the empirical and simulation approaches. (A, B, I, J) PFR overcomes elbow turning sections in real conditions and in the simulation environment in (C, K). (D, E, F, H) PFR surpasses transition areas in real conditions, whose diameters vary from small to big ones, especially in (D, H), gravity against the forward motion of PFR. (G) PFR traverses a small-to-big transition area in the simulation environment. (L) PFR performs the steering ability by changing the rotation direction of the vibration. (M, N) PFR proceeds with inspection missions in dark conditions. The high-lumen LED is activated to support the record from the NanEye camera. In (D, H, I), the red dash circles demonstrate positions where PFR hangs its body to prepare for the upward motion against gravity. Note that the diameter dimensions in this figure stand for the inner diameters of the pipe.

From Figure 6.9A to Figure 6.9L, PFR could completely traverse all these designed set-ups of the experiment. Figure 6.9A to Figure 6.9H are adaptability experiments. PFR was deployed in variable cavities with the inner diameter varying from 1 to 1.5 times the outer diameter of PFR. In general, the speed of PFR drops when it has to deal with larger pipes because the PFR needs to inflate to bigger radii, leading to the extension of the deflation spans. For the cases of traveling through transition areas, in Figure 6.9D, E, F, H, it is easier and faster to move

horizontally than vertically. Moreover, PFR finds it less complicated to go through the small-to-big transition areas due to the inclined angle of the soft spike's design. Notably, the simulation tool also exhibited the same result as the tests for traversing transition areas (see Figure 6.9G). Next, we wanted to examine PFR's capability of overcoming extreme curvature conditions in a network of pipes, such as a 90-degree elbow configuration. The PFR demonstrated its ability to navigate zones with sharp curvatures, successfully handling C-shaped and 90-degree turns even under the influence of gravity (see Figure 6.9A, B, I, J). Additionally, the simulation model showed successful traversal on these challenging curves before being tested in actual conditions (see Figure 6.9C, K). PFR is a vibration-based soft design, and the source of vibration is a DC motor equipped with an eccentric mass. Therefore, we figured out that PFR can navigate to the left or right at branch locations by changing the rotation direction of the eccentric mass. Figure 6.9L illustrates the navigation ability of PFR at the T branch section. Finally, from these evaluations, it is suggested that the proposed simulation framework can be utilized to pre-assess the success rate of PFR when dealing with an arbitrary pipeline condition before deploying the robot to the actual site. Thanks to the adaptive function attributed to the body morphology, PFR can deliver locomotion through variable working environments with a simple control method, Mode 3.

Additionally, we took the inspection ability into consideration. A high-lumen LED and a tiny camera, a NanEye camera, are integrated into the rigid frame of PFR for handling inspection missions in dark conditions. Figure 6.9M, N show the recorded images from the NanEye camera with the aid of the light from the LED.





# Chapter 7

## Discussion and Conclusion

### 7.1 Leafbot design

#### 7.1.1 Design and fabrication

We aimed to develop a vibration-based design capable of navigating complicated and uneven terrain, addressing limitations in previous models. We proposed a soft, monolithic silicone rubber structure and focused on limb morphology to improve obstacle handling. We were interested in the curved shape because of its geometrical properties. However, such geometric designs are challenging to fabricate. The current process involves creating a mold with a laser cutting machine, which can lead to parts being over- or under-fitted, complicating assembly and placement in the Mold Star 16 FAST compound. The tips of the limbs are not often fully filled with silicone because the air bubbles can not be removed completely by a vacuum chamber. These issues remain unresolved. Additionally, keeping Dragon Skin 30 parts A and B in cool condition is essential to maintain the silicone's low viscosity for effective molding.

#### 7.1.2 Dynamics and *Terradynamics study*

In our dynamics study, we analyzed the locomotion of our vibration-based soft robot using both analytical and empirical methods. The mathematical model shows a jumping gait in the  $Z$  direction (Fig. 5.2) and a sine-wave-like instantaneous velocity (Fig. 5.6) in the  $X$  direction. Both analytical and experimental models were tested on flat surfaces. However, the analytical model focused solely on uni-directional motion rather than planar conditions. The equations of motion were derived using the Lagrange method, which describes the system's dynamics through energy and generalized coordinates. While the Lagrange approach effectively accommodates complex constraints, it is not directly suited for control design in the same way as state-space functions. However, this dissertation has not yet presented the state-space functions, as the primary focus was on elucidating the complex physical phenomena that

govern the behavior of Leafbot, where constrained functions play a critical role and cannot be overlooked. Future work will expand on the state-space representation to enable the application of control techniques. Determining the frequency in the mathematical model involves complex steps: capturing motion with a high-speed camera, analyzing marker data, and performing the Fast Fourier Transform (FFT) to identify dominant frequencies related to applied voltages. Inconsistent quality between vibrators also affects frequency accuracy. Although the vibration frequencies directly influence the output states of Leafbot, this study did not focus on verifying the resonant frequencies of Leafbot due to the complex physical behaviors during the locomotion occurrence. This remaining problem will be addressed in our future work.

In our *terradynamics* study, we assessed our vibration-based design’s navigational capability across three scenarios, each providing benchmarks for robot mobility on various terrains. The first two scenarios evaluated terrain slope and height, focusing on geometry-based traversability analysis. The third scenario tested traversal in step-field terrains, which were characterized by the rugosity factor,  $R_g$ . Results showed that Leafbot performed promisingly thanks to its soft and flexible design. However, the study focused on uni-directional movement rather than 2D surfaces, and only rigid obstacles and terrains were tested. Environments with granular or cluster conditions were not explored. In the first scenario, all patterns struggled with bump-like obstacles at  $\beta = 90$  deg and  $h = 10$  mm  $= 2h_{hip}$ . This means the robot might be unable to overcome a bump higher than two times the robot’s hip height. But Leafbot5 and Leafbot9 can effortlessly handle semi-circular obstacles up to four times  $h_{hip}$ , even five times  $h_{hip}$  of Leafbot9.

### 7.1.3 In-plane locomotion verification

First, we tested the steering capability by adding two additional vibrators to the left and right sides of Leafbot, a method shown to bring the navigation ability [36]. We identified the best configuration for steering curvature and turning potential. However, navigation evaluation relied mainly on empirical methods due to the complexity of constructing an analytical model. The *terradynamics* of Leafbot with multiple vibrators have not been addressed in this paper.

### 7.1.4 Conclusion

This study introduces our soft monolithic structure for vibration-based robots, designed to handle complex environments beyond flat surfaces. The analytical model has been verified only for flat, unidirectional conditions. The fundamental principle of our design involves vibration-

induced centripetal force and asymmetric friction from the robot’s limb morphology. This non-symmetry, resulting from the limb design, enhances the robot’s ability to navigate challenging terrains and obstacles. Our *terradynamics* study demonstrates the robot’s performance on irregular terrains and its capability for 2D navigation, fulfilling the goals for advanced vibration-driven locomotion.

### 7.1.5 Future works

This vibration-driven design concept can deliver better locomotion performance and feature useful functions with specific technical improvements. Firstly, the current fabrication process is multi-step and lacks complete control over the quality of the limb structure, which impacts the Leafbot-X’s steering in 2D spaces. Secondly, the Leafbot body morphology is a soft monolithic structure; thus, the elastic properties of the backbone and the limb pattern are similar, which might not be optimized for locomotion. Using materials with different shore hardness for each, such as Dragon Skin 30 for the backbone and a stiffer material for the limbs, could increase Leafbot’s speed and overall performance. Finally, we aim to enhance the Leafbot-X design by equipping it with a wireless control module and a miniature camera, aiming for inspection missions at a miniature scale.

## 7.2 PufferFace Robot-PFR design

### 7.2.1 Design and fabrication

Our goal was to develop a vibration-drive robot design that enables it to adapt to variable cavities in pipeline systems. The design concept drew inspiration from a pufferfish. Thus, the PFR was equipped with soft skin to facilitate the adaptive function. Because of the monolithic structure, the soft skin was made from silicone rubber material and fabricated by the molding technique, which was inherited and slightly modified from the fabrication method of Leafbot design. Instead of making a core from acrylic sheets, we utilized a 3D printer to prepare the mold. Although PFR’s shape is symmetric and cylindrical, the soft skin still needs to be pre-cast in a flat form because it would be very challenging and complicated if it were cast in a cylindrical shape. Therefore, we must take one more step to make the flat skin turn into a cylindrical shape by adhering one side to the other of the skin with the same silicone rubber of the skin on the rigid frame. This step is essential and requires rigor because if we add too much

silicone, the stiffness of the skin will not be distributed equally, resulting in the un-uniform inflation of skin and affecting the locomotion performance. In general, the fabrication process is still complicated and takes a lot of steps.

It is worth highlighting that the current design is the result of experiments performed under various conditions, where we used different types of miniature vibrators and three types of silicone materials (Dragon Skin 10, Dragon Skin 30, and Ecoflex 00-30). Locomotion can be improved by using a harder material (Dragon Skin 30) for the spike structure while keeping the skin as Dragon Skin 10 for easier inflation, though this makes the fabrication process more complicated.

The entire structure of PFR is influenced by the vibrator size. It is almost impossible to obtain  $OD_S$  lower than 20 mm with the currently utilized vibration actuation mechanism.

### 7.2.2 Locomotion performance

PFR can obtain three modes of locomotion based on the combination of two input parameters. Mode 3 primarily delivers propulsive motion with the adaptive ability to varying tubular conditions, whereas Mode 2 is suitable for the approach to inspecting targets at close ranges due to the slow speed, and Mode 1 is only feasible when the size of constrained environments is roughly equal to the outer diameter of PFR,  $OD_S$ . Additionally, since Mode 2 can securely anchor the body to the pipe wall, it is well-suited for inspection tasks in vertical conditions, where the robot needs to suspend its body against gravity for extended periods. Based on the experimental data, PFR in Mode 2 can generate a static propelled force that is 20-fold to 35-fold more than the weight of PFR. However, Mode 2 locomotion is limited to forward motion in horizontal pipes.

Besides the high adaptability, the soft skin of PFR also brings another advantage when it can indirectly determine the transformation in the diameter of the interacting cavity environment based on the change of the pressure curve at the inflation phase.

The traverse ability of PFR was assessed based on the *terradynamics* approach in critical conditions of a pipeline network, including the high curvature pipes, the 90-degree elbow tubes, the small-pipe-to-big-pipe transition areas and vice versa, even with the influence of gravity, and the steering at the T branch. In addition, PFR is equipped with a miniature camera and light source to assist the inspection task in dark conditions.

Additional experiments were performed to quantitatively analyze the effect of air pressure

inside the soft skin on the robot’s moving speed. The robot achieves the highest speed when the air pressure sufficiently decreases during deflation, allowing the spikes on the soft skin to create appropriate friction with the inner surface of the pipe. However, the relationship between the air pressure inside the soft skin, the friction between the spikes and the inner surface of the pipe during the inflation/deflation process, and the moving speed have not been mathematically defined in this study, which limits our ability to determine the optimal air pressure for achieving the highest moving speed.

Being inherited from the morphological design of Leafbot’s limb, PFR can easily generate forward motion through a vibration mechanism. However, the disadvantage is that the current morphology model of PFR’s soft spikes to drive PFR forward is unable to perform backward locomotion.

### 7.2.3 FEA-based simulation model

The paper presents a FEA-based simulation model that simplifies a complex 3D model into a 2D model, substantially lowering computational costs while still accurately capturing the essential physical behaviors of the real system. The aim is to assess the PFR’s ability to navigate predefined constrained environments before deploying it in real-world conditions and to analyze the impact of parameters such as vibration frequency and average deflation rate on its motion performance. Overall, the proposed simplified simulation approach is acceptable for the following reasons:

- We reported that the simplified simulation model accurately captures the key features of Mode 3, including the standstill during the inflation phase and locomotion during the deflation phase.
- Although the model was tested under twelve different conditions – comprising three pipe sizes and four vibration frequencies with one pressure threshold – the simulation data consistently showed that displacement increases corresponding to the rising vibration frequency across all scenarios.
- The model also demonstrated the adaptability of the soft skin to various pipe sizes, using a single equivalent activated pressure value to the applied pressure set at 23 kPa.

Nevertheless, there are discrepancies between the simulation outcomes and the experimental results in terms of displacement values and the out-of-phase time-position data between the

simulated and the experiment approach. These errors might come from factors that are challenging to cover in the simulation procedure, including the effects of the tether vibration, the friction between wires and the inner wall of the pipes, and the defects of the soft skin and spikes during the fabrication process. The simplified process from the 3D to the 2D space cannot fully represent all physical features of the actual model. The non-linear properties of the hyperelastic material also made it difficult to capture precise displacement data. Therefore, this paper did not attempt to develop a simulation model with high accuracy of displacement data. Instead, the focus is on exploring the underlying physical behaviors, such as the effects of the inflation/deflation mechanism and the vibration frequency on the locomotion, and evaluating the traversal capability to critical constraints that can be used for the intuitive design of the proposed robot.

#### **7.2.4 Evaluate the cavity traversal performance based on the *terradynamics* approach**

Thanks to the adaptive morphology of the soft spikes and skin, PFR can adapt to varying tubular conditions with ease. PFR presented the capability of traversing critical positions that can be regularly found in many pipeline systems, *i.e.*, branches, elbow turnings, T-shaped sections, horizontal and vertical transitions between different sizes of pipes, *etc.* In general, PFR effortlessly overcame these challenging areas; however, the design concept still has a limitation when coping with special zones such as T intersections placed in vertical configurations. These conditions might require two modules of PFR connected in series to traverse. To the best of my knowledge, although many proposed models have been particularly developed for small-scale applications in cavities, they can not manage to traverse the T-connector regions with vertical configuration.

#### **7.2.5 Conclusion**

In this study, we introduced an innovative design for a bio-inspired robot, named the PufferFace Robot (PFR), which utilizes a hybrid propulsion system. The proposed robot has the following contributions: adaptability to diverse cavity environments, a hollow structure that allows efficient gas and fluid flow during inspections, and an adaptive design that enables PFR to navigate complex tubular systems with simple control. In addition, we present an FEA-

based method to simulate the locomotion of PFR in the aforementioned testing scenarios. The purpose is to evaluate the capability of overcoming predefined constrained environments before deploying the PFR to actual conditions. The outcomes of the simulation are consistent with the experimental results.

### 7.2.6 Future work

In our future works, we will focus on mathematically modeling the required number and size of spikes, along with the resulting propulsion force, to determine their patterns on the limited surface area of the soft skin. This aims to establish a method for optimizing propulsion force for various applied environments. We also will focus on developing a mathematical model of the relationship between the air pressure inside the soft skin and the robot's moving speed, as well as a closed-loop control strategy based on this mathematical model to achieve the optimal moving speed of the robot. In addition, the system controlling the deflation rate of PFR needs to be improved to fully characterize the non-linear behavior of the pressure curve during deflating instead of using the average deflation rate parameter,  $Df_r^a$ .





# Achievements

## Papers submission and other publications as co-author:

- [1] **L. V. Nguyen**, K. T. Nguyen and V. A. Ho, “Terradynamics of Monolithic Soft Robot Driven by Vibration Mechanism,” in *IEEE Transactions on Robotics*, vol. 41, pp. 1436-1455, 2025, doi: 10.1109/TRO.2025.3532499. Journal Impact Factor: 9.4 (2023).
- [2] **Linh Viet Nguyen**, Hansoul Kim, Khoi Thanh Nguyen, Farshid Alambeigi, and Van Anh Ho, “Adaptable Cavities Exploration: Bioinspired Vibration-Propelled PufferFace Robot with Morphable Body,” *Science Advances* (Under revision - Revised and Resubmitted). Journal Impact Factor: 11.7 (2023).
- [3] M. Kusunoki, **L. V. Nguyen**, et al., “Scalable and Foldable Origami-Inspired Supernumerary Robotic Limbs for Daily Tasks,” *IEEE Access*, 2024.
- [4] M. Kusunoki, **L. V. Nguyen**, et al., “Integration of Origami Twisted Tower to Soft Mechanism Through Rapid Fabrication Process,” In 2024 IEEE/SICE International Symposium on System Integration (SII), pp. 01-02. IEEE, 2024.
- [5] O. Yukiko, Q. K. Luu, and **L. V. Nguyen**. “Integration of Soft Tactile Sensing Skin with Controllable Thermal Display toward Pleasant Human-Robot Interaction.” In 2024 IEEE/SICE International Symposium on System Integration (SII), pp. 369-375. IEEE, 2024.

## Patent

**Linh Viet Nguyen**, Farshid Alambeigi, and Van Anh Ho, “APPARATUS AND METHODS FOR LOCOMOTION WITHIN CONSTRAINED ENVIRONMENTS,” in the process of filing a patent in the United States of America.

## Honors and awards

- 2024 Finalist of Best Poster Award at 2024 IEEE/RSJ International Conference on Intelligent Robots and Systems (IROS 2024) Workshop:  
**“The Soft Frontier Adaptive Technology in Soft Robotics”.**
- 2024 Finalist of Best Designs Award in a Competition of “*Soft Robotics on a Budget Challenge*” at 2024 IEEE-RAS International Conference on Soft Robotics (ROBOTSOFT 2024) Workshop:  
**“Democratization of Soft Robotics through Embodied Intelligence”.**
- 2024 Finalist of Best Paper Award at 2024 IEEE/SICE International Symposium on System Integration (SII)
- 2021 - 2025 MEXT Scholarship for Ph.D. student

# Appendix A

## Limb morphology of Leafbot

We employed the Dynamic Explicit Module in ABAQUS to numerically evaluate the dynamics properties of Leafbot designs featuring different limb patterns. The Yeoh model was utilized for simulation tasks. Leafbot5 pattern was applied for evaluation. The inclination angle of the straight limb is selected at 57deg so that the curved and the straight designs both have an equivalent lumped stiffness.

Vibration frequency: 170 Hz. The amplitude of centripetal force in the  $X$  and  $Z$  directions: 0.0065 N. The tails of centripetal force vectors are placed between the first and the second limbs.

The 2D model of two limb patterns are both subjected to gravity in the simulation environment.

The material constants applied to the Yeoh model are as follows:  $C_1 = 96 \text{ kPa}$ ,  $C_2 = 9.5 \text{ kPa}$  [91].



# Appendix B

## Experimental values of Leafbot

The experimental values for section 5.1 are shown in Table B.1.

Table B.1: The experimental values for the analytical model.

Experimental parameters	$m_e$ (kg)	$e$ (m)	$\mu_s$	$k_z$ (N/m)
Values	$0.082 \times 10^{-3}$	$3.4 \times 10^{-3}$	0.7	250
Experimental parameters	$k_\psi$ (Nm/rad)	$b_z$ (Ns/m)	$b_x$ (Ns/m)	
Values	0.002	1.3	0.01	

The nodes' mass on Leafbot designs are shown in Table B.2, which are also input parameters for the analytical model.

Table B.2: The nodes' mass on Leafbot designs

	Nodes' mass (kg)	
Leafbot3	$m_1$	$m_2$ and $m_3$
	$2.1 \times 10^{-3}$	$0.23 \times 10^{-3}$
Leafbot5	$m_1$	$m_2$ to $m_4$
	$2.6 \times 10^{-3}$	$0.5 \times 10^{-3}$
Leafbot9	$m_1$	$m_2$ to $m_7$
	$3 \times 10^{-3}$	$0.3 \times 10^{-3}$



# References

- [1] R. Pfeifer, *How the body shapes the way we think: A New View of intelligence*. MIT Press, 2006.
- [2] E. W. Hawkes, L. H. Blumenschein, J. D. Greer, and A. M. Okamura, “A soft robot that navigates its environment through growth,” *Science Robotics*, vol. 2, no. 8, p. eaan3028, 2017.
- [3] H. Lu, M. Zhang, Y. Yang, Q. Huang, T. Fukuda, Z. Wang, and Y. Shen, “A bioinspired multilegged soft millirobot that functions in both dry and wet conditions,” *Nature communications*, vol. 9, no. 1, p. 3944, 2018.
- [4] D. Kim, Z. Hao, A. R. Mohazab, and A. Ansari, “On the forward and backward motion of milli-bristlebots,” *International Journal of Non-Linear Mechanics*, vol. 127, p. 103551, 2020.
- [5] G. Notomista, S. Mayya, A. Mazumdar, S. Hutchinson, and M. Egerstedt, “A study of a class of vibration-driven robots: Modeling, analysis, control and design of the brushbot,” in *2019 IEEE/RSJ International Conference on Intelligent Robots and Systems (IROS)*. IEEE, 2019, pp. 5101–5106.
- [6] F. Becker, S. Boerner, V. Lysenko, I. Zeidis, and K. Zimmermann, “On the mechanics of bristle-bots-modeling, simulation and experiments,” in *ISR/Robotik 2014; 41st international symposium on robotics*. VDE, 2014, pp. 1–6.
- [7] W. P. Weston-Dawkes, I. Adibnazari, Y.-W. Hu, M. Everman, N. Gravish, and M. T. Tolley, “Gas-lubricated vibration-based adhesion for robotics,” *Advanced Intelligent Systems*, vol. 3, no. 7, p. 2100001, 2021.
- [8] A. Sabbadini, M. A. Atalla, and M. Wiertlewski, “Simple and fast locomotion of vibrating asymmetric soft robots,” *Soft Robotics*, vol. 10, no. 6, pp. 1199–1208, 2023.



- [9] C. Tang, B. Du, S. Jiang, Q. Shao, X. Dong, X.-J. Liu, and H. Zhao, “A pipeline inspection robot for navigating tubular environments in the sub-centimeter scale,” *Science Robotics*, vol. 7, no. 66, p. eabm8597, 2022.
- [10] F. Becker, S. Börner, T. Kästner, V. Lysenko, I. Zeidis, and K. Zimmermann, “Spy bristle bot—a vibration-driven robot for the inspection of pipelines,” in *58th Ilmenau Scientific Colloquium*, 2014, pp. 1–7.
- [11] C. Hong, Y. Wu, C. Wang, Z. Ren, C. Wang, Z. Liu, W. Hu, and M. Sitti, “Wireless flow-powered miniature robot capable of traversing tubular structures,” *Science Robotics*, vol. 9, no. 88, p. eadi5155, 2024.
- [12] I. Stewart and P. Tallapragada, “A fast steerable soft robot for navigating a pipe network,” in *2023 IEEE/RSJ International Conference on Intelligent Robots and Systems (IROS)*. IEEE, 2023, pp. 4322–4327.
- [13] L. Xu, L. Zhang, J. Zhao, and K. Kim, “Cornering algorithm for a crawler in-pipe inspection robot,” *Symmetry*, vol. 12, no. 12, p. 2016, 2020.
- [14] B. Chong, J. He, D. Soto, T. Wang, D. Irvine, G. Blekherman, and D. I. Goldman, “Multilegged matter transport: A framework for locomotion on noisy landscapes,” *Science*, vol. 380, no. 6644, pp. 509–515, 2023.
- [15] C. Li, T. Zhang, and D. I. Goldman, “A terradynamics of legged locomotion on granular media,” *science*, vol. 339, no. 6126, pp. 1408–1412, 2013.
- [16] S. W. Gart and C. Li, “Body-terrain interaction affects large bump traversal of insects and legged robots,” *Bioinspiration & Biomimetics*, vol. 13, no. 2, p. 026005, 2018.
- [17] S. W. Gart, C. Yan, R. Othayoth, Z. Ren, and C. Li, “Dynamic traversal of large gaps by insects and legged robots reveals a template,” *Bioinspiration & biomimetics*, vol. 13, no. 2, p. 026006, 2018.
- [18] A. Kakogawa, S. Ma, and S. Hirose, “An in-pipe robot with underactuated parallelogram crawler modules,” in *2014 IEEE international conference on robotics and automation (ICRA)*. IEEE, 2014, pp. 1687–1692.

- [19] E. Rhee, R. Hunt, S. J. Thomson, and D. M. Harris, “Surferbot: A wave-propelled aquatic vibrobot,” *arXiv preprint arXiv:2203.15896*, 2022.
- [20] D. Q. Nguyen and V. A. Ho, “Anguilliform swimming performance of an eel-inspired soft robot,” *Soft Robotics*, vol. 9, no. 3, pp. 425–439, 2022.
- [21] R. J. Clapham and H. Hu, “isplash: Realizing fast carangiform swimming to outperform a real fish,” *Robot fish: bio-inspired fishlike underwater robots*, pp. 193–218, 2015.
- [22] M. Wehner, R. L. Truby, D. J. Fitzgerald, B. Mosadegh, G. M. Whitesides, J. A. Lewis, and R. J. Wood, “An integrated design and fabrication strategy for entirely soft, autonomous robots,” *nature*, vol. 536, no. 7617, pp. 451–455, 2016.
- [23] L. Van Duong *et al.*, “Large-scale vision-based tactile sensing for robot links: Design, modeling, and evaluation,” *IEEE Transactions on Robotics*, vol. 37, no. 2, pp. 390–403, 2020.
- [24] Q. K. Luu, N. H. Nguyen *et al.*, “Simulation, learning, and application of vision-based tactile sensing at large scale,” *IEEE Transactions on Robotics*, 2023.
- [25] E. Brown, N. Rodenberg, J. Amend, A. Mozeika, E. Steltz, M. R. Zakin, H. Lipson, and H. M. Jaeger, “Universal robotic gripper based on the jamming of granular material,” *Proceedings of the National Academy of Sciences*, vol. 107, no. 44, pp. 18 809–18 814, 2010.
- [26] V. Consumi, J. Merlin, L. Lindenroth, D. Stoyanov, and A. Stilli, “A novel soft shape-shifting robot with track-based locomotion for in-pipe inspection,” *arXiv preprint*, 2022.
- [27] L. Manfredi, E. Capoccia, G. Ciuti, and A. Cuschieri, “As oft p neumatic i nchworm d ouble balloon (spid) for colonoscopy,” *Scientific reports*, vol. 9, no. 1, p. 11109, 2019.
- [28] Y. Tang, Y. Chi, J. Sun, T.-H. Huang, O. H. Maghsoudi, A. Spence, J. Zhao, H. Su, and J. Yin, “Leveraging elastic instabilities for amplified performance: Spine-inspired high-speed and high-force soft robots,” *Science advances*, vol. 6, no. 19, p. eaaz6912, 2020.
- [29] L. Xu, R. J. Wagner, S. Liu, Q. He, T. Li, W. Pan, Y. Feng, H. Feng, Q. Meng, X. Zou *et al.*, “Locomotion of an untethered, worm-inspired soft robot driven by a shape-memory alloy skeleton,” *Scientific Reports*, vol. 12, no. 1, p. 12392, 2022.

- [30] S. C. Van Den Berg, R. B. Scharff, Z. Rusák, and J. Wu, “Openfish: Biomimetic design of a soft robotic fish for high speed locomotion,” *HardwareX*, vol. 12, p. e00320, 2022.
- [31] T. F. Nygaard, C. P. Martin, D. Howard, J. Torresen, and K. Glette, “Environmental adaptation of robot morphology and control through real-world evolution,” *Evolutionary Computation*, vol. 29, no. 4, pp. 441–461, 2021.
- [32] V. C. Müller and M. Hoffmann, “What is morphological computation? on how the body contributes to cognition and control,” *Artificial life*, vol. 23, no. 1, pp. 1–24, 2017.
- [33] M. Calisti, G. Picardi, and C. Laschi, “Fundamentals of soft robot locomotion,” *Journal of The Royal Society Interface*, vol. 14, no. 130, p. 20170101, 2017.
- [34] Y. Sun, A. Abudula, H. Yang, S.-S. Chiang, Z. Wan, S. Ozel, R. Hall, E. Skorina, M. Luo, and C. D. Onal, “Soft mobile robots: A review of soft robotic locomotion modes,” *Current Robotics Reports*, vol. 2, pp. 371–397, 2021.
- [35] L. Giomi, N. Hawley-Weld, and L. Mahadevan, “Swarming, swirling and stasis in sequestered bristle-bots,” *Proceedings of the Royal Society A: Mathematical, Physical and Engineering Sciences*, vol. 469, no. 2151, p. 20120637, 2013.
- [36] K. Ioi, “A mobile micro-robot using centrifugal forces,” in *1999 IEEE/ASME International Conference on Advanced Intelligent Mechatronics (Cat. No. 99TH8399)*. IEEE, 1999, pp. 736–741.
- [37] F. Becker, “An approach to the dynamics of vibration-driven robots with bristles,” *IFAC-PapersOnLine*, vol. 48, no. 1, pp. 842–843, 2015.
- [38] C. Li, A. O. Pullin, D. W. Haldane, H. K. Lam, R. S. Fearing, and R. J. Full, “Teradynamically streamlined shapes in animals and robots enhance traversability through densely cluttered terrain,” *Bioinspiration & biomimetics*, vol. 10, no. 4, p. 046003, 2015.
- [39] G. Cicconofri and A. DeSimone, “Motility of a model bristle-bot: A theoretical analysis,” *International Journal of Non-Linear Mechanics*, vol. 76, pp. 233–239, 2015.
- [40] A. DeSimone and A. Tatone, “Crawling motility through the analysis of model locomotors: two case studies,” *The European Physical Journal E*, vol. 35, pp. 1–8, 2012.

- [41] H. H. Hariri, L. A. Prasetya, S. Foong, G. S. Soh, K. N. Otto, and K. L. Wood, “A tetherless legged piezoelectric miniature robot using bounding gait locomotion for bidirectional motion,” in *2016 IEEE International Conference on Robotics and Automation (ICRA)*. IEEE, 2016, pp. 4743–4749.
- [42] B. John and M. Shafeek, “Pipe inspection robots: a review,” in *IOP Conference Series: Materials Science and Engineering*, vol. 1272, no. 1. IOP Publishing, 2022, p. 012016.
- [43] X. Liu, M. Song, Y. Fang, Y. Zhao, and C. Cao, “Worm-inspired soft robots enable adaptable pipeline and tunnel inspection,” *Advanced Intelligent Systems*, vol. 4, no. 1, p. 2100128, 2022.
- [44] H. Choi and S. Ryew, “Robotic system with active steering capability for internal inspection of urban gas pipelines,” *Mechatronics*, vol. 12, no. 5, pp. 713–736, 2002.
- [45] P. Palanisamy, R. E. Mohan, A. Semwal, L. M. Jun Melivin, B. Félix Gómez, S. Balakrishnan, K. Elangovan, B. Ramalingam, and D. N. Terntzer, “Drain structural defect detection and mapping using ai-enabled reconfigurable robot raptor and iort framework,” *Sensors*, vol. 21, no. 21, p. 7287, 2021.
- [46] D. V.-K. Le, Z. Chen, and R. Rajkumar, “Multi-sensors in-line inspection robot for pipe flaws detection,” *IET Science, Measurement & Technology*, vol. 14, no. 1, pp. 71–82, 2020.
- [47] Y. Wang and J. Zhang, “Autonomous air duct cleaning robot system,” in *2006 49th IEEE International Midwest Symposium on Circuits and Systems*, vol. 1. IEEE, 2006, pp. 510–513.
- [48] W. Zhao, M. Kamezaki, K. Yamaguchi, M. Konno, A. Onuki, and S. Sugano, “A wheeled robot chain control system for underground facilities inspection using visible light communication and solar panel receivers,” *IEEE/ASME Transactions on Mechatronics*, vol. 27, no. 1, pp. 180–189, 2021.
- [49] A. Kakogawa, T. Nishimura, and S. Ma, “Designing arm length of a screw drive in-pipe robot for climbing vertically positioned bent pipes,” *Robotica*, vol. 34, no. 2, pp. 306–327, 2016.

- [50] V. Korendiy, O. Kotsiumbas, V. Borovets, V. Gurey, and R. Predko, “Mathematical modeling and computer simulation of the wheeled vibration-driven in-pipe robot motion,” *Vibroengineering Procedia*, vol. 44, pp. 1–7, 2022.
- [51] A. Zagler and F. Pfeiffer, “” moritz” a pipe crawler for tube junctions,” in *2003 IEEE international conference on robotics and automation (Cat. No. 03CH37422)*, vol. 3. IEEE, 2003, pp. 2954–2959.
- [52] P. Valdastri, R. J. Webster, C. Quaglia, M. Quirini, A. Menciassi, and P. Dario, “A new mechanism for mesoscale legged locomotion in compliant tubular environments,” *IEEE Transactions on Robotics*, vol. 25, no. 5, pp. 1047–1057, 2009.
- [53] H. Yaguchi and T. Izumikawa, “Cableless in-piping magnetic actuator system capable of inspection over long distances,” *IEEE Transactions on Magnetics*, vol. 50, no. 11, pp. 1–4, 2014.
- [54] Y. Lin, Y.-X. Xu, and J.-Y. Juang, “Single-actuator soft robot for in-pipe crawling,” *Soft Robotics*, vol. 10, no. 1, pp. 174–186, 2023.
- [55] K. Ohno, S. Kawatsuma, T. Okada, E. Takeuchi, K. Higashi, and S. Tadokoro, “Robotic control vehicle for measuring radiation in fukushima daiichi nuclear power plant,” in *2011 IEEE International Symposium on Safety, Security, and Rescue Robotics*. IEEE, 2011, pp. 38–43.
- [56] K. Nagaya, T. Yoshino, M. Katayama, I. Murakami, and Y. Ando, “Wireless piping inspection vehicle using magnetic adsorption force,” *Ieee/Asme Transactions on Mechatronics*, vol. 17, no. 3, pp. 472–479, 2012.
- [57] L. Brown, J. Carrasco, S. Watson, and B. Lennox, “Elbow detection in pipes for autonomous navigation of inspection robots,” *Journal of Intelligent & Robotic Systems*, vol. 95, pp. 527–541, 2019.
- [58] Y.-S. Kwon and B.-J. Yi, “Design and motion planning of a two-module collaborative indoor pipeline inspection robot,” *IEEE Transactions on Robotics*, vol. 28, no. 3, pp. 681–696, 2012.

- [59] C. Li and X. He, “A bio-mimetic pipe crawling microrobot driven based on self-excited vibration,” in *2007 IEEE International Conference on Robotics and Biomimetics (ROBIO)*. IEEE, 2007, pp. 984–988.
- [60] S. F. Jatsun, K. Zimmerman, I. Zeidis, and A. S. Jatsun, “Vibration driven robots for in pipe inspection,” in *2007 IEEE International Conference on Mechatronics*. IEEE, 2007, pp. 1–5.
- [61] H. Zhang, M. Gao, Z. Li, and Q. Wu, “Vibration analysis of an in-pipe inspection robot considering fluid-structure coupling,” *International Journal of Structural Stability and Dynamics*, vol. 22, no. 05, p. 2250055, 2022.
- [62] R. R. Sattarov and M. A. Almaev, “Electromagnetic worm-like locomotion system for in-pipe robots: design and vibration-driven motion analysis,” in *2017 Dynamics of Systems, Mechanisms and Machines (Dynamics)*. IEEE, 2017, pp. 1–6.
- [63] S.-g. Roh and H. R. Choi, “Differential-drive in-pipe robot for moving inside urban gas pipelines,” *IEEE transactions on robotics*, vol. 21, no. 1, pp. 1–17, 2005.
- [64] Z. Wang and H. Gu, “A bristle-based pipeline robot for ill-constraint pipes,” *IEEE/ASME Transactions On Mechatronics*, vol. 13, no. 3, pp. 383–392, 2008.
- [65] P. Liu, Z. Wen, and L. Sun, “An in-pipe micro robot actuated by piezoelectric bimorphs,” *Chinese science bulletin*, vol. 54, no. 12, pp. 2134–2142, 2009.
- [66] T. Idogaki, H. Kanayama, N. Ohya, H. Suzuki, and T. Hattori, “Characteristics of piezoelectric locomotive mechanism for an in-pipe micro inspection machine,” in *MHS’95. Proceedings of the Sixth International Symposium on Micro Machine and Human Science*. IEEE, 1995, pp. 193–198.
- [67] J. Xing, C. Ning, Y. Liu, and I. Howard, “Piezoelectric inertial robot for operating in small pipelines based on stick-slip mechanism: modeling and experiment,” *Frontiers of Mechanical Engineering*, vol. 17, no. 3, p. 41, 2022.
- [68] L. Sun, Y. Zhang, P. Sun, and Z. Gong, “Study on robots with pzt actuator for small pipe,” in *MHS2001. Proceedings of 2001 International Symposium on Micromechatronics and Human Science (Cat. No. 01TH8583)*. IEEE, 2001, pp. 149–154.

- [69] X. Ji, X. Liu, V. Cacucciolo, M. Imboden, Y. Civet, A. El Haitami, S. Cantin, Y. Perriard, and H. Shea, “An autonomous untethered fast soft robotic insect driven by low-voltage dielectric elastomer actuators,” *Science Robotics*, vol. 4, no. 37, p. eaaz6451, 2019.
- [70] M. Duduta, D. R. Clarke, and R. J. Wood, “A high speed soft robot based on dielectric elastomer actuators,” in *2017 IEEE International Conference on Robotics and Automation (ICRA)*. IEEE, 2017, pp. 4346–4351.
- [71] A. Minaminosono, H. Shigemune, Y. Okuno, T. Katsumata, N. Hosoya, and S. Maeda, “A deformable motor driven by dielectric elastomer actuators and flexible mechanisms,” *Frontiers in Robotics and AI*, vol. 6, p. 1, 2019.
- [72] E.-F. M. Henke, S. Schlatter, and I. A. Anderson, “Soft dielectric elastomer oscillators driving bioinspired robots,” *Soft robotics*, vol. 4, no. 4, pp. 353–366, 2017.
- [73] R. F. Shepherd, F. Ilievski, W. Choi, S. A. Morin, A. A. Stokes, A. D. Mazzeo, X. Chen, M. Wang, and G. M. Whitesides, “Multigait soft robot,” *Proceedings of the national academy of sciences*, vol. 108, no. 51, pp. 20 400–20 403, 2011.
- [74] H. Zhao, K. O’Brien, S. Li, and R. F. Shepherd, “Optoelectronically innervated soft prosthetic hand via stretchable optical waveguides,” *Science robotics*, vol. 1, no. 1, p. eaai7529, 2016.
- [75] M. Luo, W. Tao, F. Chen, T. K. Khuu, S. Ozel, and C. D. Onal, “Design improvements and dynamic characterization on fluidic elastomer actuators for a soft robotic snake,” in *2014 IEEE International Conference on Technologies for Practical Robot Applications (TePRA)*. IEEE, 2014, pp. 1–6.
- [76] C. D. Onal and D. Rus, “Autonomous undulatory serpentine locomotion utilizing body dynamics of a fluidic soft robot,” *Bioinspiration & biomimetics*, vol. 8, no. 2, p. 026003, 2013.
- [77] H. Yuk, S. Lin, C. Ma, M. Takaffoli, N. X. Fang, and X. Zhao, “Hydraulic hydrogel actuators and robots optically and sonically camouflaged in water,” *Nature communications*, vol. 8, no. 1, p. 14230, 2017.

- [78] Y. Chen, Y. Zhang, H. Li, J. Shen, F. Zhang, J. He, J. Lin, B. Wang, S. Niu, Z. Han *et al.*, “Bioinspired hydrogel actuator for soft robotics: Opportunity and challenges,” *Nano Today*, vol. 49, p. 101764, 2023.
- [79] D. Jiao, Q. L. Zhu, C. Y. Li, Q. Zheng, and Z. L. Wu, “Programmable morphing hydrogels for soft actuators and robots: from structure designs to active functions,” *Accounts of Chemical Research*, vol. 55, no. 11, pp. 1533–1545, 2022.
- [80] H.-T. Lin, G. G. Leisk, and B. Trimmer, “Goqbot: a caterpillar-inspired soft-bodied rolling robot,” *Bioinspiration & biomimetics*, vol. 6, no. 2, p. 026007, 2011.
- [81] B. Kim, M. G. Lee, Y. P. Lee, Y. Kim, and G. Lee, “An earthworm-like micro robot using shape memory alloy actuator,” *Sensors and Actuators A: Physical*, vol. 125, no. 2, pp. 429–437, 2006.
- [82] X. Huang, K. Kumar, M. K. Jawed, A. Mohammadi Nasab, Z. Ye, W. Shan, and C. Majidi, “Highly dynamic shape memory alloy actuator for fast moving soft robots,” *Advanced Materials Technologies*, vol. 4, no. 4, p. 1800540, 2019.
- [83] M. Sun, C. Tian, L. Mao, X. Meng, X. Shen, B. Hao, X. Wang, H. Xie, and L. Zhang, “Reconfigurable magnetic slime robot: deformation, adaptability, and multifunction,” *Advanced Functional Materials*, vol. 32, no. 26, p. 2112508, 2022.
- [84] K. Zhu, H. Li, W. Zhao, X. Zhang, S. Li, K. Zhang, and T. Xu, “A millimeter-scale micro crawling robot with fast-moving driven by a miniature electromagnetic linear actuator,” *Advanced Intelligent Systems*, p. 2300909, 2024.
- [85] H. Lu, Y. Hong, Y. Yang, Z. Yang, and Y. Shen, “Battery-less soft millirobot that can move, sense, and communicate remotely by coupling the magnetic and piezoelectric effects,” *Advanced Science*, vol. 7, no. 13, p. 2000069, 2020.
- [86] L. Yehezkel, S. Berman, and D. Zarrouk, “Overcoming obstacles with a reconfigurable robot using reinforcement learning,” *IEEE Access*, vol. 8, pp. 217 541–217 553, 2020.
- [87] A. Jacoff, A. Downs, A. Virts, and E. Messina, “Stepfield pallets: Repeatable terrain for evaluating robot mobility,” in *Proceedings of the 8th workshop on performance metrics for intelligent systems*, 2008, pp. 29–34.



- [88] P. Vartholomeos and E. Papadopoulos, “Analysis and experiments on the force capabilities of centripetal-force-actuated microrobotic platforms,” *IEEE transactions on robotics*, vol. 24, no. 3, pp. 588–599, 2008.
- [89] O. N. Beck, P. Taboga, and A. M. Grabowski, “Characterizing the mechanical properties of running-specific prostheses,” *PloS one*, vol. 11, no. 12, p. e0168298, 2016.
- [90] P. Taboga, O. N. Beck, and A. M. Grabowski, “Prosthetic shape, but not stiffness or height, affects the maximum speed of sprinters with bilateral transtibial amputations,” *Plos one*, vol. 15, no. 2, p. e0229035, 2020.
- [91] M. S. Xavier, A. J. Fleming, and Y. K. Yong, “Finite element modeling of soft fluidic actuators: Overview and recent developments,” *Advanced Intelligent Systems*, vol. 3, no. 2, p. 2000187, 2021.
- [92] O. H. Yeoh, “Some forms of the strain energy function for rubber,” *Rubber Chemistry and technology*, vol. 66, no. 5, pp. 754–771, 1993.
- [93] A. C. Quillen, R. C. Nelson, H. Askari, K. Chotkowski, E. Wright, and J. K. Shang, “A light-weight vibrational motor powered recoil robot that hops rapidly across granular media,” *Journal of Mechanisms and Robotics*, vol. 11, no. 6, 2019.
- [94] I. Stancic, D. Borojevic, V. Zanchi, I. Rudas, M. Demiralp, and N. Mastorakis, “Human kinematics measuring using a high speed camera and active markers,” in *WSEAS International Conference. Proceedings. Mathematics and Computers in Science and Engineering*, no. 5. WSEAS, 2009.
- [95] C. E. Shannon, “Communication in the presence of noise,” *Proceedings of the IRE*, vol. 37, no. 1, pp. 10–21, 1949.
- [96] Z. Wang and S. Hirai, “Soft gripper dynamics using a line-segment model with an optimization-based parameter identification method,” *IEEE Robotics and Automation Letters*, vol. 2, no. 2, pp. 624–631, 2017.
- [97] J. Baumgarte, “Stabilization of constraints and integrals of motion in dynamical systems,” *Computer methods in applied mechanics and engineering*, vol. 1, no. 1, pp. 1–16, 1972.
- [98] D. Morin, “Transverse waves on a string,” 2021.

- [99] P. Papadakis, “Terrain traversability analysis methods for unmanned ground vehicles: A survey,” *Engineering Applications of Artificial Intelligence*, vol. 26, no. 4, pp. 1373–1385, 2013.
- [100] R. Hoffman and E. Krotkov, “Terrain roughness measurement from elevation maps,” in *Mobile Robots IV*, vol. 1195. SPIE, 1990, pp. 104–114.
- [101] D. Helmick, A. Angelova, and L. Matthies, “Terrain adaptive navigation for planetary rovers,” *Journal of Field Robotics*, vol. 26, no. 4, pp. 391–410, 2009.
- [102] M. A Bekhti, “Traversability cost prediction of outdoor terrains for mobile robot using image features,” Ph.D. dissertation, Shizuoka University, 2020.
- [103] H. Inotsume, T. Kubota, and D. Wettergreen, “Robust path planning for slope traversing under uncertainty in slip prediction,” *IEEE Robotics and Automation Letters*, vol. 5, no. 2, pp. 3390–3397, 2020.
- [104] H. Seraji, “Traversability index: a new concept for planetary rovers,” in *Proceedings 1999 IEEE International Conference on Robotics and Automation (Cat. No. 99CH36288C)*, vol. 3. IEEE, 1999, pp. 2006–2013.

